8022955

McCumber, Michael Charles

A NUMERICAL SIMULATION OF THE INFLUENCE OF HEAT AND MOISTURE FLUXES UPON MESOSCALE CIRCULATIONS

University of Virginia   Ph.D.   1980

University Microfilms International

300 N. Zeeb Road, Ann Arbor, MI 48106   18 Bedford Row, London WC1R 4EJ, England

PLEASE NOTE:

The negative microfilm copy of this dissertation was prepared and inspected by the school granting the degree. We are using this film without further inspection or change. If there are any questions about the film content, please write directly to the school.

UNIVERSITY MICROFILMS

A NUMERICAL SIMULATION OF THE
INFLUENCE OF HEAT AND MOISTURE
FLUXES UPON MESOSCALE CIRCULATIONS

Michael Charles McCumber
Scotia, New York

B.A., State University of New York-Oswego, 1971
M.S., State University of New York-Albany, 1974

A Dissertation Presented to the Graduate
Faculty of the University of Virginia
in Candidacy for the Degree of
Doctor of Philosophy

Department of Environmental Sciences

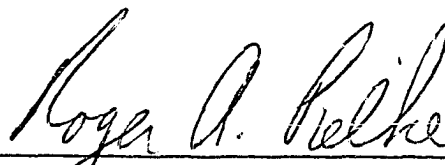University of Virginia

May 1980

A Dissertation Presented to the Graduate
Faculty of the University of Virginia
in Candidacy for the Degree of
Doctor of Philosophy

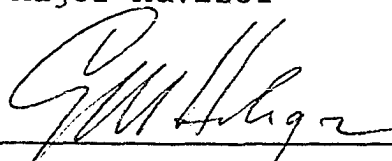Department of Environmental Sciences
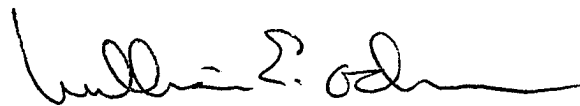University of Virginia

May 1980

and Approved by:

_____
Roger A. Pielke
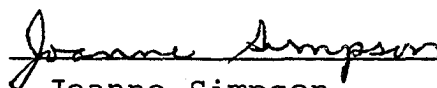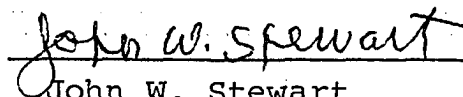Major Advisor

_____
George Hornberger

_____
William Odum

_____
Joanne Simpson

_____
John W. Stewart

DEDICATION

To my family, which has patiently supported me
through the course of this research, and espec-
ially to my parents, Chuck and Rita.

A NUMERICAL SIMULATION OF THE INFLUENCE OF HEAT AND MOISTURE FLUXES UPON MESOSCALE CIRCULATIONS

ABSTRACT

Michael Charles McCumber

Sensible and latent heat fluxes at the ground surface are often parameterized in mesoscale numerical models using a simple slab approach. While this is economically advantageous relative to using a layered soil profile, it can lead to an erroneous specification of these fluxes. It is demonstrated that the soil moisture is the dominant soil variable, controlling both the temporal variation and the intensity of the moisture and sensible heat fluxes. Experiments show that the computed fluxes are strongly influenced by the type of slab parameterization chosen.

A hydrostatic primitive equation model is used to evaluate the effects of variable soil conditions upon the development of a south Florida sea breeze. A multi-layered soil profile is used to eliminate the numeric deficiencies often associated with slab soil parameterizations. The model is designed to accomodate up to twelve different soil types simultaneously which can be horizontally mapped in any desired combination. Vegetation is also parameterized in the manner of Deardorff (1978). Allowance is made for a variable number of canopies, which can be mapped much like the soils.

Three-dimensional experiments indicated that the intensity and the pattern of the mesoscale convergence are strongly

affected by soil conditions and their distribution. Vegetation also affects both the strength and pattern of the mesoscale convergence and it delays the strongest development by one to two hours where the soil is wettest.

A general weakening and some broadening of the sea breeze convergence accompanied cloudiness and precipitation, which were predicted using a simple, explicit parameterization. These effects resulted from a reduced horizontal temperature gradient along the west coast of Florida. The greatest temperature contrast over land occurred along the eastern edge of the clouds. It was here that the strongest sea breeze convergence occurred.

iii

ACKNOWLEDGEMENTS

iv

TABLE OF CONTENTS

vi

TABLE OF CONTENTS (CONT'D)

Page

LIST OF FIGURES

viii

ix

content is 0.07 cm^3/cm^3. b. Initial moisture content is 0.12 cm^3/cm^3. Heat fluxes directed toward the atmosphere are negative.

xi

ground specific humidity (long dashed line) in g/kg. The abscissa is the local time in hours.

Figure 28. Comparison of energy fluxes from simulated vegetation. Fluxes plotted are the total sensible heat, total latent heat and the transpiration fluxes (watts/m^2). Negative fluxes are directed toward the atmosphere. a. grass overlying peat soil (σ_f = 0.85) b. trees overlying sandy clay soil (σ_f = 0.90).

Figure 29. Comparison between the predicted sensible heat flux from simulated foliage and the heat flux diagnosed using an equation for heat conduction through the laminar boundary layer above the surface of a leaf. a. Sand with trees (σ_f = 0.90) b. Sand with grass (σ_f = 0.75) Negative fluxes are directed toward the atmosphere.

Figure 30. Profiles of predicted soil temperatures (°C) for early afternoon (1315 LST) and at sunrise the following morning (0515 LST). a. afternoon profile b. morning profile

Figure 31. Same as Figure 30, except for the predicted soil moisture content (cm^3/cm^3).

Figure 32. Vertical profile of the atmospheric potential temperature (K) for early afternoon (1315 LST) and at sunrise the following day (0515 LST). a. afternoon profile b. morning profile

Figure 33. Same as Figure 32, except for the wind speed

(cm/sec). An additional plot is made for early

morning of the first day (0715 LST). Notice the

development of the nocturnal jet at low levels.

Figure 44.   a. Predicted boundary layer height (km) at 1815 LST for an East-West cross-section of south Florida (row 17). b. Predicted atmospheric specific humidity. Upper set of curves applies to a height of 200 meters, while the lower set of curves applies to a height of 2500 meters. The abscissa is labelled by gridpoint.

Figure 45.   a. Predicted horizontal winds at 25 meters for Run A (homogeneous sand). Wind speed is proportional to arrow length with one grid interval equal to 8 m/sec. b. Predicted vertical velocity at 1200 meters. Contour interval is 4 cm/sec. Dashed lines indicate negative velocities. Time is 1315 LST.

Figure 46.   Same as Figure 45, except for Run B (mixed bare soils).

Figure 47.   Same as Figure 45, except for Run C (mixed soils and vegetation).

Figure 48.   Shower pattern observed at 1300 LST on July 17, 1973 by the Miami WSR-57 digitized radar. Contours for rainfall rates are drawn for 0.25, 2.29, 13.72, 30.23 and 66.55 mm/hr.

Figure 49.   Radar echoes observed by the Miami radar at 1400 LST on July 17, 1973. Rainfall contour intervals are the same as in Figure 48.

Figure 50.   Same as Figure 45, except the time is 1815 LST. Contour interval for the vertical velocities is

5 cm/sec.

Figure 51. Same as Figure 46, except the time is 1815 LST.
Contour interval for the vertical velocities is
5 cm/sec.

Figure 52. Same as Figure 47, except the time is 1815 LST.
Contour interval for the vertical velocities is
5 cm/sec.

Figure 53. A DAPP (Data Acquisition and Processing Program)
satellite photograph of south Florida taken at
1237 LST on July 17, 1973.

Figure 54. a. Predicted horizontal winds at 25 meters for
Run D (mixed soils). Wind speed is proportional
to arrow length with one grid interval equal to
8 m/sec. b. Predicted vertical velocity at
1200 meters. Contour interval is 4 cm/sec.
Dashed lines indicate negative velocities. Time
is 1115 LST.

Figure 55. Predicted cloud cover at 1715 LST (composited
from all levels) for Run D.

Figure 56. Same as Figure 54, except at 1815 LST. Contour
interval in b. is 10 cm/sec.

Figure 57. a. Predicted horizontal winds at 25 meters for
Run E. Wind speed is proportional to arrow
length with one grid interval equal to 8 m/sec.
b. Predicted vertical velocity at 1200 meters.
Contour interval is 5 cm/sec. Dashed lines
indicate negative velocities. Time is 1515 LST.

Figure 58. Same as Figure 57, except the time is 1715 LST.

LIST OF TABLES

experiments for the surface temperature (T_G), surface specific humidity (q_G), latent heat flux (LE) and sensible heat flux (H).

I. Introduction

A. An Overview

Mesoscale weather phenomena typically have dimensions of the order of about 10-1000 kilometers. They often originate as perturbations to the large-scale flow due to the effects of regional forcing. Such effects may be due to roughness inhomogeneities, orography or differential heating, for example. In effect these local perturbations are a significant influence on local weather and present a formidable challenge to forecasters. It has recently been suggested that forecasting skill has reached a plateau (AMS, 1976). Undoubtedly significant improvements will have to await advances in prediction on the mesoscale (Fritsch and Kreitzberg, 1978; Golden et al., 1978).

Numerous numerical prediction models have been developed to properly address and interpret the mesoscale. They are typically applied to domains on the order of several hundreds of kilometers, with notably enhanced vertical and horizontal resolution compared with synoptic numerical models. The principal premise is that better resolution yields better forecasts! However, some of the advantage is lost since mesoscale models are commonly initialized from a data base which is designed for the synoptic scale. In the absence of orography, this results in a refined synoptic prediction, rather than a truly mesoscale prediction.

Data deficiencies aside, the ultimate merit of the prediction lies with the capability of the model. Much success

has been reported in simulating the general features of a host of mesoscale phenomena. Among them are the strength and organization of the sea breeze convergence (Pielke, 1974; Hsu, 1979; Anthes and Warner, 1978; Tapp and White, 1976; Carpenter, 1979), the airflow over mountains (Klemp and Lilly, 1978; Anthes and Warner, 1978; Mahrer and Pielke, 1977) and lake-effect storms (Lavoie et al., 1970). Other applications may include predicting valley winds , the dispersion of air pollutants and prediction of areas prone to severe local storms.

Both the spatial and the temporal scales characterizing mesoscale weather tend to be small, the latter being typically of the order of several hours. For this reason, the mesoscale is sufficiently responsive to surface exchanges of mass, heat and momentum that they should be computed with some care. Improvements in the acquisition of mesoscale data are beyond the scope of this work. However, an attempt is made to show that improvement in mesoscale prediction could be achieved through more realistic simulation of surface conditions.

B. Surface Parameterizations

Much work has been accomplished to develop relationships which express the turbulent exchange of heat, moisture and momentum within the atmospheric surface layer. Empirical formulae such as those of Businger (1973) have been utilized in numerical models with considerable success. However, the surface layer relations are limited by the accuracy with which the ground surface parameters are computed.

Clearly there is little difficulty with treating momentum exchange at the surface, since the ground acts as a momentum sink. Reasonable values of roughness length are known and they are sufficient to characterize the surface. On the other hand, soil surface temperature and, in particular, soil moisture are usually less accurately specified.

The surface heat flux is a principal driving force in a mesoscale model. In previous work, the soil surface temperature, which regulates the heat flux, has been either specified or predicted. When specified, the customary approach is to assume that the diurnal change behaves as a sinusoidal wave, such as in the mesoscale models of Pielke (1974) and Tapp and White (1976) and the boundary layer model of Burk (1977). This can be a very good method since the sinusoidal wave can be tailored to fit observed data. But the surface temperature is unresponsive to the environment, which is an important drawback. All land gridpoints have the same temperature, despite variability in turbulent exchange, soil type and observed cloud cover. (Some models (e.g.,

Neumann and Mahrer, 1975) specify $T_G = T_G(t,x)$ but this requires the additional assumption that the atmospheric forcing is persistent.)

The soil surface temperature is usually predicted by solving a surface energy balance equation

$$R_n + \rho L u_* q_* + \rho C_p u_* \theta_* - G = 0 .$$

R_n is the net radiation flux, the second and third terms are latent and sensible heat fluxes, respectively, and G is the soil heat flux. There is some variability in the specification of atmospheric radiative fluxes among modellers, ranging from detailed calculations (Atwater, 1973) to a simple bulk parameterization (Carpenter, 1979). But the main difference between the schemes which are used to compute the soil temperature concerns the treatment of the soil heat flux. Deardorff (1978) provides a comprehensive evaluation of six techniques. One scheme defined a layered soil temperature profile, while the other five treat the soil as a homogeneous slab. Three of the slab schemes solve for the temperature directly from the surface energy balance equation. The other two schemes each use a prognostic equation relating the soil heat flux (defined as the sum of all the other terms in the energy balance equation) to the depth of either the annual or the diurnal temperature wave.

Deardorff found that one of the latter schemes, termed force-restore (Blackadar, 1976) yielded very acceptable temperatures, especially when the solar forcing was strong. The essence of this technique is that the influence of the

soil heat flux is partially offset by the deep soil tempera-
ture--hence a restoring effect. The best predictions typically
occurred between local noon and sunset, while discrepancies
as large as 2°C due to underprediction occurred at other
times.

Intuitively the most accurate specification of the soil
heat flux results from solving the vertical heat diffusion
equation over several levels in the soil (at least to the
depth of the diurnal wave). However, the added computer
storage requirements and the concomitant greater expense of
such an approach enhance the appeal of the more efficient
slab approaches used by most modellers.

The parameterization of soil moisture fluxes tends to
be even less detailed than the representation of the heat
fluxes. A few modellers elect to ignore it (Klemp and Lilly,
1978; Anthes and Warner, 1978). Burk (1977) specifies it by
treating the surface specific humidity as a diurnal wave,
while Perkey (1976) related the sensible and latent heat
fluxes using a Bowen ratio which is constant in both time
and space.

Others (Dieterle (1976), Mahrer and Pielke (1977),
Deardorff (1978), Pandolfo and Jacobs (1973) and Hsu (1979))
weighted the surface specific humidity in the following
manner:

I.1 $\qquad q_G = \delta\, q_s\, (T_G) + (1 - \delta)\, q(1)$.

Here $q_s\,(T_G)$ is the saturation specific humidity at the soil
temperature T_G, $q(1)$ is the specific humidity at the first

model atmospheric level above the ground and δ is a measure of soil wetness. Various meanings are attributed to δ. Generally it is either the ratio of actual to potential evaporative flux (Halstead et al., 1957) or it is the ratio of soil moisture to a saturation value. It will be demonstrated later that the behavior of soil moisture is significantly linked to the way in which δ is defined.

Relatively few atmospheric models utilize a layered soil moisture profile. For example, the models of Sasamori (1970) and Garrett (1978) each employ the detailed soil physics parameterization developed by Philip (1957). In these models vertical diffusion equations are solved for the soil temperature and the soil moisture content, taking into account the fluxes driven by both the thermal and moisture gradients in the soil. The surface specific humidity is related to the soil relative humidity, following Philip.

Few efforts have been expended to parameterize the modifying effects on surface heat and moisture fluxes produced by vegetation. Carpenter (1977), in one of the first efforts, parameterized the influence of a vegetative cover in a mesoscale model by employing a surface resistance to evaporation. However, this resistance was constrained to assume one of only three values over the course of a diurnal cycle.

Recently, Deardorff (1978) developed a simple and efficient parameterization for a single-level canopy. It permitted variable foliage cover, variable stomatal resistance and it treated interception of rainfall and dewfall. Removal

of soil moisture by the foliage was accomplished by extracting the entire transpiration flux from the deep soil moisture, while he permitted only a tenth of the flux to deplete the surface moisture so that the evaporative demand upon the surface moisture would not be severe. The deep soil and surface moistures were independent variables. He showed through his simulations that neglecting the vegetation could result in estimates of evaporative fluxes that are in error by a factor of two.

Garrett (1978) applied Deardorff's scheme to his three-dimensional model with apparent success. He noted that inclusion of the foliage affected both the timing and the intensity of the convection predicted by his model.

C. Proposal

Gannon (1978) studied the effects of surface heat and moisture fluxes and cirrus cloud cover on south Florida sea breezes. He used a two-dimensional model which featured a detailed computation of atmospheric radiation fluxes with a soil surface temperature computed from a slab model. A prognostic equation relating the net flux at the soil surface to the soil thermal inertia defined the temperature tendency. The thermal inertia was defined as

$$I = (\kappa_s \rho_s c_s)^{1/2} \quad ,$$

where κ_s is the soil thermal conductivity, ρ_s is the density of the soil and c_s is the soil specific heat. Gannon attempted to simulate a variety of soil characteristics by specifying an initial distribution of thermal inertia which was fixed in time. He treated the surface specific humidity as a function of the surface relative humidity. The relative humidity was fixed in time, but variable in space.

Carpenter (1977) investigated surface exchanges using a three-dimensional model and he also applied it to south Florida. He eliminated the surface specific humidity altogether, choosing instead to restrict the surface evaporative flux via the choice of a representative surface resistance to evaporation. He also computed the soil surface temperature using a slab technique. Carpenter did not include clouds and like Gannon, his model was run without precipitation.

In this dissertation a model has been developed to further examine the influence of surface fluxes of moisture

and heat on a mesoscale circulation. Since previous work has simulated south Florida circulations, numerical experiments are also performed here for the same geographic location in order to test the response of the sea breeze to changes in the surface fluxes. In this model both the soil moisture and the soil temperature are detailed in a soil layer characterized by fourteen levels over a depth of one meter. This is done to render a more accurate prediction by eliminating numeric deficiencies often found in simpler slab techniques.

The model is three dimensional and it is capable of horizontally mapping up to eleven different types of soil, as well as peat. Thermal and moisture diffusivities are variable, each being a function of the soil moisture content and the type of soil. The ground surface temperature is determined from an energy balance equation, which uses computed radiation fluxes from the atmosphere. The surface specific humidity is dependent upon the surface relative humidity (which in turn is a function of the soil moisture stress and the soil temperature (Philip, 1957)).

Vegetation is included using a modification of Deardorff's (1978) parameterization. Only a single canopy is permitted in each grid box; however, the foliage characteristics can vary in adjacent grid cells. A provision is made to accommodate a variable stomatal resistance and rainfall/dewfall interception, following Deardorff.

Additionally condensation is parameterized to permit

the release of latent heat into the atmosphere, when the predicted mesoscale convergence is sufficient. Rain which reaches the ground is allowed to alter the soil and vegetation fluxes, thereby effecting a feedback to the atmosphere.

Features of the numerical model are presented more fully in the sections which follow. The governing equations are found in section II and the parameterizations of physical processes are detailed in section III. Section IV explains the numerical techniques used, while section V contains the boundary and the initial conditions.

The response of the simulated atmosphere to changing soil conditions is examined in a series of one-dimensional sensitivity experiments. The effects of foliage cover are determined in an analogous way. Results of these experiments are presented in section VI. A horizontal distribution of native Florida soils is used in several three-dimensional sensitivity experiments. Section VII discusses the experiments, which systematically endeavor to evaluate the impact of variable soil type, vegetation and precipitating clouds on the evolving mesoscale convergence. It will be demonstrated that each of these three factors can significantly influence both the intensity as well as the arrangement of the convergence.

II. <u>Model Mathematical Framework</u>

The basic model equations are those of Pielke (1974). The modifications cited in Mahrer and Pielke (1977) are also included. The model is hydrostatic, the Boussinesq approximation is applied and the model is initialized from a barotropic synoptic state. The lower boundary is the ground surface, which may include topography, while a material surface bounds the top of the domain. The material surface, which fluctuates in response to the integrated divergence below it, is intended to preclude loss of mass solely due to the addition of heat to the volume.

The predictive equations are the following:

II.1
$$\frac{du}{dt} = fv - fV_g - \Theta\frac{\partial \pi}{\partial x} + g\left[\frac{z^* - \overline{S}}{\overline{S}}\right]\frac{\partial Z_G}{\partial x} - g\frac{z^*}{\overline{S}}\frac{\partial S}{\partial x}$$

$$+ \left(\frac{\overline{S}}{S-Z_G}\right)^2 \frac{\partial}{\partial z^*}\left[K_z^m \frac{\partial u}{\partial z^*}\right] + \text{Fil}(u) \quad,$$

II.2
$$\frac{dv}{dt} = -fu + fU_g - \Theta\frac{\partial \pi}{\partial y} + g\left[\frac{z^* - \overline{S}}{\overline{S}}\right]\frac{\partial Z_G}{\partial y} - g\frac{z^*}{\overline{S}}\frac{\partial S}{\partial x}$$

$$+ \left(\frac{\overline{S}}{S-Z_G}\right)^2 \frac{\partial}{\partial z^*}\left[K_z^m \frac{\partial v}{\partial z^*}\right] + \text{Fil}(v) \quad,$$

II.3
$$\frac{d\Theta}{dt} = \left(\frac{\overline{S}}{S-Z_G}\right)^2 \frac{\partial}{\partial z^*}\left[K_z^\theta \frac{\partial \Theta}{\partial z^*}\right] + \text{Fil}(\Theta) + F_\theta \quad,$$

II.4
$$\frac{dq}{dt} = \left(\frac{\overline{S}}{S-Z_G}\right)^2 \frac{\partial}{\partial z^*}\left[K_z^\theta \frac{\partial q}{\partial z^*}\right] + \text{Fil}(q) + F_q \quad,$$

II.5
$$\frac{\partial}{\partial t}(S-Z_G) + \frac{\partial}{\partial x}\left[u(S-Z_G)\right] + \frac{\partial}{\partial y}\left[v(S-Z_G)\right] + \frac{\partial}{\partial z^*}\left[w^*(S-Z_G)\right]$$

$$= 0 \quad ,$$

II.6 $\quad \dfrac{\partial \pi}{\partial z^*} = -\left(\dfrac{S - Z_G}{\overline{S}} \right) \dfrac{g}{\Theta} \quad ,$

where $\quad \dfrac{d}{dt} = \dfrac{\partial}{\partial t} + u \dfrac{\partial}{\partial x} + v \dfrac{\partial}{\partial y} + w^* \dfrac{\partial}{\partial z^*} \quad .$

In order, II.1 through II.6 are the equations of motion for the u and v components of velocity, the thermodynamic equation, the conservation equation for specific humidity, the incompressible continuity equation and the hydrostatic equation. The transformed vertical coordinate z* is defined by

II.7 $$z^* = \overline{S} \left[\dfrac{Z - Z_G}{S - Z_G} \right] ,$$

where $\overline{S}$ is the initial (uniform) height of the material surface, Z is the cartesian height coordinate and Z_G is the local topographic height. S is the local height of the material surface.

The scaled pressure, π , is obtained from

II.8 $$\pi = c_p \left[\dfrac{P}{1000} \right]^{R/c_p} ,$$

where P is the pressure in millibars. The fourth and fifth terms on the right-hand side of II.1 and II.2 result from using the transformed vertical coordinate.

Fil ( ) is a horizontal filter operating on the variable in parentheses. Its characteristics will be discussed later. F_θ and F_q are the source terms for heat and water vapor,

respectively. They are described in more detail in section
III.C .

The vertical eddy exchange coefficients are evaluated
in the next section. Subscript z refers to the vertical
dimension, whereas superscripts m and θ refer to momentum
and heat, respectively.

The transformed vertical velocity w* is prescribed to
be zero at the upper and the lower bounding surfaces. Thus
a tendency equation for the material surface results:

$$\text{II.9} \qquad \frac{\partial S}{\partial t} = -\frac{1}{\bar{S}} \int_0^{\bar{S}} \left\{ \frac{\partial}{\partial x} \left[u(S-Z_G) \right] + \frac{\partial}{\partial y} \left[v(S-Z_G) \right] \right\} dz*$$

All of the remaining variables assume their conventional
meaning. A complete list is provided in Appendix A.

III. Description of Model Physics

A. Boundary Layer

The free atmosphere is coupled with the ground surface through a planetary boundary layer. A surface layer, which is assumed to be characterized by constant turbulent fluxes, resides in the lowest subsection of the boundary layer. Its depth is specified as

III.A.1
$$h = z_i / 25 \quad .$$

The denominator was varied from 15 to 45 in an earlier version of the model to test its sensitivity. It was found that the solutions varied little over the entire range.

Turbulent exchange is computed using first-order closure. Within the surface layer the exchange coefficients are specified as

$$K_z^m (z*) = k_o u_* z* / \phi_m (\xi)$$

III.A.2
$$K_z^\theta (z*) = K_z^q (z*) = k_o u_* z* / \phi_h (\xi) ,$$

where k_o is the von Karman constant (.35) and u_* is the friction velocity. $\phi_m (\xi)$ and $\phi_h (\xi)$ are the non-dimensional Obukhov similarity functions for momentum and heat, respectively. They are obtained from the work of Businger (1973). For an unstable stratification,

$$\phi_m = (1 - 15 \xi)^{-0.25}$$

III.A.3
$$\phi_h = .74 (1 - 9 \xi)^{-.50}$$

and for a stable atmosphere

III.A.4
$$\phi_m = 1 + 4.7\, \xi$$

$$\phi_h = .74 + 4.7\, \xi \qquad ,$$

where $\xi = z^* / L_*$ and L_* is the Monin-Obukhov mixing length

$$L_* = \frac{\theta\, u_*^2}{k_0 g \theta_*} \quad .$$

Assuming that the friction velocity can be expressed in the form

$$u_*^2 = K_z^m \, \frac{\partial u}{\partial z^*}$$

$$= (\, k_0 u_* z^* \,/\, \phi_m(\, \xi\,)\,) \frac{\partial u}{\partial z^*} \quad ,$$

then an alternate expression for $\phi_m(\, \xi\,)$ becomes

III.A.5.a
$$\phi_m(\xi) = \frac{k_0 z^*}{u_*} \, \frac{\partial u}{\partial z^*} \quad .$$

Similarly,

III.A.5.b
$$\phi_h(\xi) = \frac{k_0 z^*}{\theta_*} \, \frac{\partial \theta}{\partial z^*} \quad .$$

Integrating A.5.a and A.5.b, using the roughness height (z_0^*) as a lower limit (and assuming that $z_0^* \ll L_*$), results in expressions for the surface friction parameters.

$$u_* = k_0 (u^2 + v^2)^{.5} / (\ln(z^*/z_0^*) - I_1)$$

III.A.6
$$\theta_* = k_0 (\theta - \theta(z_0^*)) \,/\, (.74(\ln(z^*/z_0^*) - I_2))$$

$$q_* = k_0 (q - q(z_0^*)) \,/\, (.74(\ln(z^*/z_0^*) - I_2))$$

The functions I_1 and I_2 are written as

<u>Unstable Case</u> $(\theta_* \leq 0)$

$$I_1 = 2\,\ln((1 + \phi_m^{-1})/2) + \ln((1 + \phi_m^{-2})/2) - 2\tan^{-1}(\phi_m^{-1})$$
$$+ \pi/2$$

$$I_2 = 2\,\ln((1 + .74\,\phi_h^{-1})\,/\,2)$$

<u>Stable Case</u> $(\theta_* > 0)$

$$I_1 = -4.7\,\xi$$

$$I_2 = -6.35\,\xi \quad .$$

Above the surface layer, the eddy exchange coefficients assume the form of interpolating polynomials as suggested by O'Brien (1970).

$$\text{III.A.7} \quad K_z(z^*) = \begin{cases} K_z\big|_{z_i} + \dfrac{(z_i - z^*)^2}{(z_i - h)^2} \left[K_z\big|_h - K_z\big|_{z_i} + (z^* - h) \left[\dfrac{\partial}{\partial z^*} K_z\big|_h + 2\,\dfrac{K_z\big|_h - K_z\big|_{z_i}}{z_i - h} \right] \right], & z_i \geq z^* \geq h \\[4ex] K_z\big|_{z_i}, & z^* > z_i \\[2ex] \dfrac{z^*}{h} K_z\big|_h, & z^* < h \quad . \end{cases}$$

The notation $\big|_h$ refers to the top of the surface layer and $K_z\big|_{z_i}$ is the exchange coefficient at and above the top of the planetary boundary layer. It is assigned a nominal value of 1 cm^2/sec.

The planetary boundary layer is permitted to vary in depth in response to turbulent fluxes within the layer as

well as to mesoscale vertical motion, and it is subject to the restraint imposed by the overlying stability. A prognostic equation for the height of the boundary layer (Deardorff, 1974) is

III.A.8

$$\frac{\partial z_i}{\partial t} + u \frac{\partial z_i}{\partial x} + v \frac{\partial z_i}{\partial y} = w^* \Big|_{z_i} + \left(\frac{1.8 (w_c^3 + 1.1\, u_*^3 - 3.3\, u_*^2\, fz_i)}{g\, \dfrac{z_i^2}{\theta} \dfrac{\partial \theta^+}{\partial z^*} + 9\, w^{*2} + 7.2\, u_*^2} \right) .$$

$w^* \Big|_{z_i}$ is the vertical velocity at the top of the boundary layer, while w_c is a convective velocity scale given by

III.A.9

$$w_c = \begin{cases} \left(-\dfrac{g}{\theta}\, u_* \theta_* z_i \right)^{1/3} & , \ \theta_* \leq 0 \\[2ex] 0 & , \ \theta_* > 0 \end{cases}$$

The potential temperature gradient at the top of the boundary layer, $\partial \theta^+ / \partial z^*$, reflects the overlying stability.

The roughness length over land is prescribed by an input parameter. However, over water, Clarke (1970) suggested that it should be related to the wind stress. It is computed as

III.A.10 $$z_0^* = 0.032\, u_*^2 / g \quad ,$$

with the restriction that $z_0^* \geq 0.0015$ cm as a lower limit.

B. Atmospheric Radiation

The pertinent equations are presented here for conven-
ience. They are explained in more depth in Mahrer and Pielke
(1977). Additions and modifications to the physics are de-
scribed in this section.

At the ground surface, the applicable energy balance
equation for bare soil is

III.B.1 $R_{sw}\big|_G + R_L + \rho L u_* q_* + \rho c_p u_* \theta_* - \lambda \dfrac{\partial T_s}{\partial z}\bigg|_G - \sigma T_G^4 = 0$,

where R_{sw} is the net incoming solar flux and R_L is the in-
coming long wave flux. The other terms are the air density
(ρ), the soil temperature (T_s) and the Stefan-Boltzmann con-
stant (σ). Subscript G refers to the surface of the soil.
The latent heat of vaporization (L) is defined as a simple
function of the temperature

III.B.2 $L = 597.3 - 0.566 \ (T - 273.15)$,

where L is in cal/g and T is the air temperature in degrees
K. The sign convention adopted for the fluxes is that they
are positive if directed toward the surface and negative if
directed away.

1. Short Wave Radiation

The intensity of the unattenuated solar beam impinging
upon the top of the atmosphere is a function of the solar
zenith angle.

III.B.3 $R_{sw} = (R_{sw})_o \ \cos (\ Z \ )$

Here $(R_{sw})_o$ is the solar constant and Z is the zenith angle.
The latter obeys the relationship,

III.B.4 $\quad \cos(Z) = \sin(\phi) \sin(\delta) + \cos(\phi) \cos(\delta) \cos(\omega)$,

in which ϕ is the mean latitude, δ is the solar declination
and ω is the solar hour angle.

The solar flux is attenuated by absorption and scattering due to atmospheric gases and by reflection from the surfaces of clouds and the ground. Mahrer and Pielke (1977) approximated absorption and scattering using two empirical functions. The first is attributed to Kondrat'yev (1969), later modified by Atwater and Brown (1974). It accounts for forward Rayleigh scattering, due to such gases as ozone, oxygen and carbon dioxide. Its functional form is

III.B.5 $\quad RAY = .485 + .515(1.041 - .16((.000949 P$
$$+ .051) / \cos (Z))^{.5}) ,$$

where P is pressure in millibars. The second term is from
McDonald (1960). It accounts for the absorption due to
water vapor.

III.B.6 $\qquad a_w = .077 (r(p) / \cos (Z))^{.3}$

The optical path length $r(p)$ above some pressure level p
takes the form

III.B.7 $\qquad r(p) = - \int_P^{P_{TOP}} \frac{q}{g} \, dp$

Here P, q and g are all in CGS units. P_{TOP} is the pressure
at the top of the model.

Attenuation by clouds is parameterized using a trans-

mission function. Atwater (in Pandolfo and Jacobs, 1973)
suggested a function of the form

$$\text{III.B.8} \qquad \tau_m = \prod_{P_o}^{TOP} \tau_z$$

where $\tau_z = 1$ when the relative humidity is less than 100% and

$$\tau_z = .4130 - .014 \, M$$

when the relative humidity equals 100%. M is the fraction
of the slant solar optical path length through the atmosphere
defined by

$$M = \frac{P(z^*)}{P_o \cos(Z)} \, .$$

P_o is the surface pressure and TOP is the top of the model,
as before. This particular function (τ_z) applies to alto-
stratus clouds. The altostratus transmission function was
selected because the model was originally designed to treat
only stable precipitation. This point will be discussed
further in section VII.

Reflection of solar radiation is called the albedo. It
varies from relatively large values at low sun angles to
smaller values near midday. The variability of albedo with
zenith angle is determined from

$$\text{III.B.9} \qquad a_n = .01(\exp(a \, z^{1.5}) - 1)$$

where $a = 0.003286$. This represents a fit to the normal-
izing function of Idso et al. (1975a) and it agrees well
with the values given by Gannon (1978). Function B.9 is
plotted in Figure 1.

Figure 1 . Relationship between the surface albedo and the solar zenith angle ($^{\circ}$). The enhancement to the surface albedo, a_n, is expressed in percent.

ZENITH ANGLE (z)

a_n
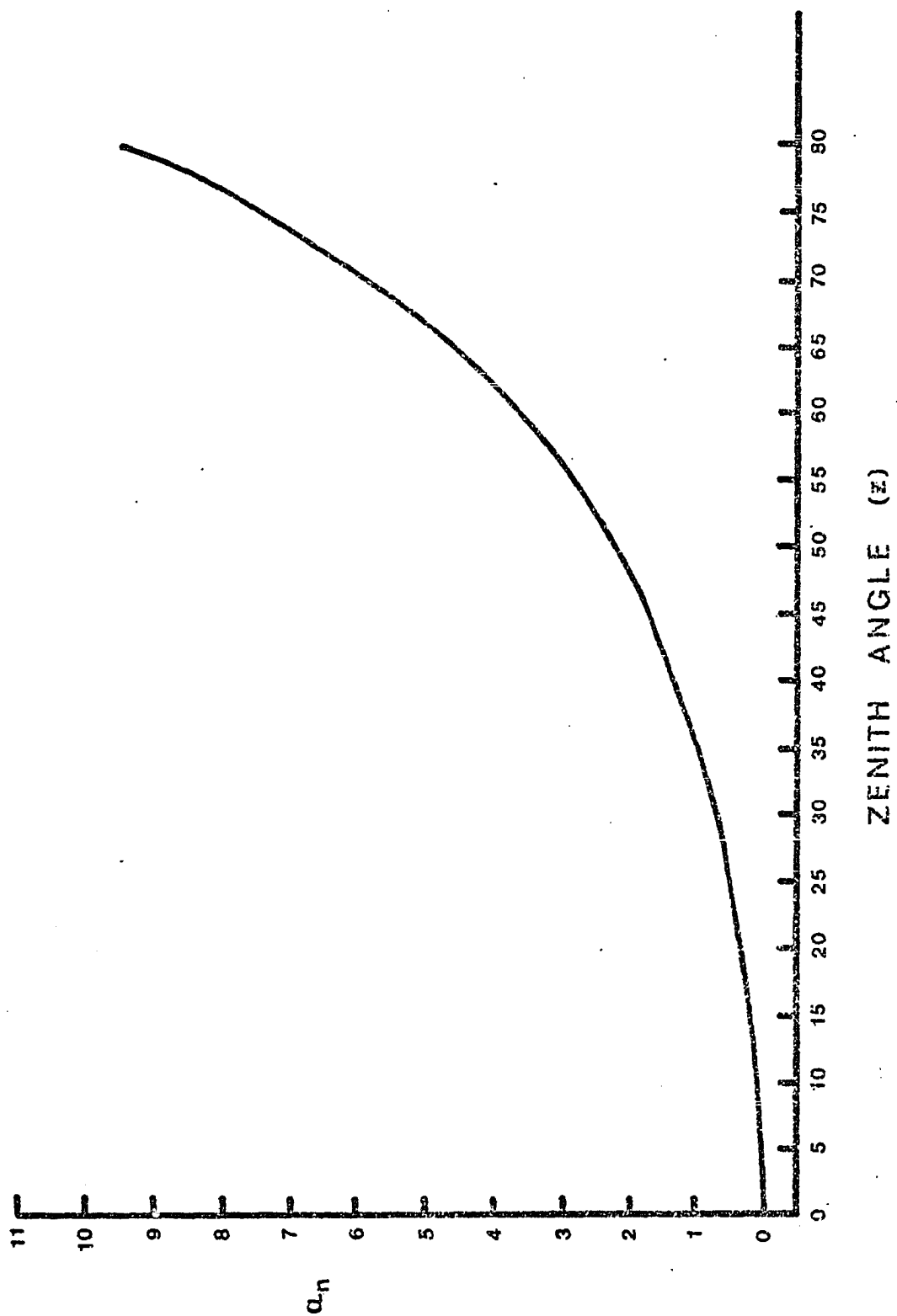
The degree of wetness of the soil also affects the surface albedo, which is lower for wetter than drier soils. From Figure 5 in Idso et al., the effect of the soil moisture becomes:

$$a_s = 0.31 - 0.34 \ \Delta \quad , \qquad \Delta \leq 0.5$$

III.B.10.1

$$a_s = 0.14 \qquad , \qquad \Delta > 0.5 \quad ,$$

where $\Delta = (\eta/\eta_s)$. The volumetric moisture content (cm^3/cm^3) is η and η_s is the porosity. Idso et al. presented relationships for only an Avondale loam soil. However. B.10.1 is extended to other soil types as a reasonable first-order estimate. Since the limiting albedos for Florida peat are readily available (Gannon, 1978), the appropriate linear relations for peat become

$$a_s = 0.14 \ (1 - \Delta) \quad , \qquad \Delta \leq 0.5$$

III.B.10.2

$$a_s = 0.07 \qquad , \qquad \Delta > 0.5 \quad .$$

Lastly, the short wave beam is modified by the local slope of the topography. The flux intensity on a slant surface, as given by Kondrat'yev (1969), is

III.B.11
$$(R_{sw})_{sl} = R_{sw} \cos(i) \quad ,$$

where the angle of incidence i is obtained from

III.B.12
$$\cos(i) = \cos(\alpha) \cos(Z) + \sin(\alpha) \sin(Z) \cos(\beta - n) \quad .$$

The slope angle, solar azimuth and slope azimuth are represented by α, β and n, respectively. They are expressed by

$$\alpha = \tan^{-1} \ (\ (\partial Z_G/\partial x)^2 + (\partial Z_G/\partial y)^2 \ )^{.5}$$

III.B.13 $\qquad \beta = \sin^{-1} (\cos(\delta) \sin(\omega) / \sin(Z))$

$$n = - \tan^{-1} (\partial Z_G/\partial y / \partial Z_G/\partial x) + \pi/2 \quad .$$

Here δ is the solar declination and ω is the solar hour angle.

Combining the influences of absorption, scattering, reflection and slope, the net solar flux at the bare ground surface is

III.B.14 $\qquad R_{sw}|_G = \begin{cases} (R_{sw})_{sl} \ (RAY-a_w)\tau_m(1-a_s-a_n) \ , \ \cos(Z)>0 \\ 0 \qquad\qquad\qquad\qquad\qquad\quad , \cos(Z) \le 0. \end{cases}$

The rate of short wave heating of the atmosphere due to the absorption by water vapor (McDonald, 1960) is

III.B.15 $\qquad \dfrac{\partial T}{\partial t} = \dfrac{0.0231}{c_p} (R_{sw})_o \left(\dfrac{r(p)}{\cos(Z)}\right)^{-.7} \dfrac{dr(p)}{dp} \cos(Z).$

2. Long Wave Radiation

The parameterization of atmospheric cooling due to the flux divergence of long wave radiation accounts for only the effects of water vapor and carbon dioxide. The optical path length (cm) for water vapor at a level with pressure P is computed from

III.B.16 $\qquad r(p) = - \displaystyle\int_{P_o}^{P} \dfrac{q}{g} \, dp \qquad$ (P in dynes/cm^2) .

And the optical path length (atm/cm) for carbon dioxide is

III.B.17 $\qquad c(p) = - 0.4148239 (P - P_o) \qquad$ (P in mb) .

Emissivities are treated in the following manner. For water vapor, they are assigned values derived from the work of Kuhn (1963) as presented in Jacobs et al. (1974).

$$\text{III.B.18} \quad \varepsilon_r(p,p_i) = \begin{cases} 0.11288 \ \log_{10}(1+12.63\ \overline{r}), & \log_{10}\ \overline{r} \leq -4 \\ 0.104 \ \log_{10}\ \overline{r} + 0.440, & -4 < \log_{10}\ \overline{r} \leq -3 \\ 0.121 \ \log_{10}\ \overline{r} + 0.491, & -3 < \log_{10}\ \overline{r} \leq -1.5 \\ 0.146 \ \log_{10}\ \overline{r} + 0.527, & -1.5 < \log_{10}\overline{r} \leq -1 \\ 0.161 \ \log_{10}\ \overline{r} + 0.542, & -1 < \log_{10}\ \overline{r} \leq 0 \\ 0.136 \ \log_{10}\ \overline{r} + 0.542, & \log_{10}\ \overline{r} > 0 \ . \end{cases}$$

This gives a range in emissivities of about 0.024 to 0.61 for values of $\overline{r}$ ranging from 0.0001 cm to 3.0 cm.

The term $\overline{r}$ is the optical path length between levels p and p_i such that

$$\overline{r} = \quad r(p) - r(p_i) \quad .$$

The emissivity due to carbon dioxide assumes a different form.

$$\text{III.B.19} \qquad \varepsilon_c(p,p_i) - 0.185 \ (1 - \exp(-.3919\ (\overline{c})^{.4}),$$

where $\overline{c}$ is analogous to $\overline{r}$, except that it applies to carbon dicxide.

$$\overline{c} = \quad c(p) - c(p_i) \quad .$$

Then the total emissivity can be written as

$$\text{III.B.20} \qquad \varepsilon(p,p_i) = \varepsilon_r(p,p_i) + \varepsilon_c(p,p_i) \quad .$$

This permits the computation of the upward and the downward directed fluxes. The long wave fluxes at some level p are

$$R_L^{\downarrow}(p) = \int_p^{P_{TOP}} \sigma\varepsilon(p,p_i) \ \frac{\partial T^4}{\partial \xi} \ d\xi$$

$$\text{III.B.21}$$

$$R_L^{\uparrow}(p) = \int_{P_o}^P \sigma\varepsilon(p,p_i) \ \frac{\partial T^4}{\partial \xi} \ d\xi \ + \ \sigma T_G^4 \quad .$$

T is the air temperature and P_o is the surface pressure. It is further assumed that the downward long wave flux at the top of the atmosphere is zero (Sasamori, 1972). The emisivities are computed in B.21 in the direction of their respective fluxes for a slab of thickness $(z* - \xi) < 0$ for $R_L^{\uparrow}$ and for $(z* - \xi) > 0$ for $R_L^{\downarrow}$.

Sasamori (1972) simplified the computation of the long wave cooling due to radiative flux divergence by assuming that the atmosphere is isothermal at the temperature of each grid point when computing the cooling at that level. The net fluxes at some level N are

$$R_L^{\uparrow} = R_L^{\uparrow} (N + 1) - R_L^{\uparrow} (N)$$

$$R_L^{\downarrow} = R_L^{\downarrow} (N + 1) - R_L^{\downarrow} (N) \quad ,$$

and the vertical flux divergence is $\dfrac{\partial R_L}{\partial p}$, where R_L is the net long wave flux. Invoking Sasamori's assumption results in a relationship for the long wave cooling:

III.B.22
$$\frac{\partial T}{\partial t} = \frac{g\sigma}{c_p} \left[(T_N^4 - T_G^4) \ (\varepsilon(N+1,G) - \varepsilon(N,G)) \ + \right.$$

$$\left. (T_{TOP}^4 - T_N^4) \ (\varepsilon(N+1,TOP) - \varepsilon(N,TOP)) \right] \frac{1}{(p(N+1) - p(N))} \ .$$

Recall that the emissivities are computed between the levels in the parentheses. TOP is the top of the model and subscript G denotes the ground surface.

The presence of a cloud layer (only a single layer is permitted, although it may extend through more than one vertical level) will alter the long wave fluxes. Since the top

and the base of the cloud deck are assumed to radiate as black bodies, the long wave fluxes must commence and terminate at these surfaces. Thus the long wave fluxes are modified so that below cloud base

$$R_L^{\downarrow}(p) = \sigma T_{BASE}^4 + \int_P^{P_{BASE}} \varepsilon(p,p_i)\sigma \frac{\partial T^4}{\partial \xi} d\xi \quad ,$$

and above the cloud top

$$R_L^{\uparrow}(p) = \sigma T_{CTOP}^4 + \int_{P_{CTOP}}^P \varepsilon(p,p_i)\sigma \frac{\partial T^4}{\partial \xi} d\xi \quad .$$

BASE is cloud base and CTOP is cloud top. No contributions are computed within the cloud since this region is assumed radiatively inactive (Sasamori, 1972).

Now the long wave cooling below cloud base can be written as:

$$\frac{\partial T}{\partial t} = \frac{g}{c_p} \sigma \left[(T_N^4 - T_G^4) \; (\varepsilon(N+1,G) - \varepsilon(N,G)) + (T_{BASE}^4 - T_N^4) \right.$$
$$\left. (\varepsilon(N+1,BASE) - \varepsilon(N,BASE)) \right] \frac{1}{(p(N+1)-p(N))} \quad ,$$

while above cloud top it is

$$\frac{\partial T}{\partial t} = \frac{g}{c_p} \sigma \left[(T_N^4 - T_{CTOP}^4)(\varepsilon(N+1,CTOP) - \varepsilon(N,CTOP)) + (T_{TOP}^4 - \right.$$
$$\left. T_N^4) \quad (\varepsilon(N+1,TOP) - \varepsilon(N,TOP)) \right] \frac{1}{(p(N+1)-p(N))} \quad .$$

Fractional cloud cover is ignored since this model assumes that a grid cell has either a total overcast or no cloud at all.

C. Atmospheric Condensation and Rainfall

Rainfall is treated quite simply. It is just the cumulative condensation which reaches the ground. Condensation and its effects are parameterized in the manner suggested by Asai (1965).

When the air is supersaturated, the potential temperature and the specific humidity are adjusted by

III.C.1
$$\theta = \tilde{\theta} + \frac{L}{c_p} \left(\frac{p_0}{p} \right)^{\kappa} F_q$$

$$q = \tilde{q} - F_q .$$

The tilda designates partially updated variables (i.e. all effects are incorporated except those due to phase changes), L is the latent heat of vaporization, $\kappa = 0.286$ and F_q is the condensed water vapor.

The moisture excess is composed of two parts: condensate and an increase in the saturation specific humidity, which is attributed to warming of the air by latent heat. The condensate, expressed as a fraction of the total excess moisture, for an isobaric process is

III.C.2
$$S' = \left[1 + \frac{L^2}{c_p R_v} \left(\frac{p_0}{p} \right)^{2\kappa} \frac{q_s(T)}{\theta^2} \right]^{-1} .$$

The saturation specific humidity $q_s(T)$ is determined from Teten's equation

III.C.3
$$q_s(T) = \frac{3.8 \, (10^{(aT/(T+b))})}{p} .$$

In this equation P is the unscaled pressure in mb and T is

the air temperature in degrees Celsius. Only the water phase
is considered, so the constants a and b assume the values
7.5 and 237.3, respectively.

The moisture excess is defined as

III.C.4 $$q' = q - \delta\, q_s(T),$$

where δ is a weighting function (ordinarily $\delta = 1$). The
condensed water vapor is

III.C.5 $$F_q = q'S' \quad .$$

The source term for the potential temperature (see
equation II.3) is expressed as

III.C.6 $$F_\theta = \frac{L}{c_p}\left(\frac{p_o}{p}\right)^{\kappa} F_q \quad .$$

If the air is <u>unsaturated</u> and rainwater (q_r) descends
into a layer, then the temperature and the humidity are
altered due to the evaporation of the rainwater until sat-
uration is achieved. When the magnitude of $(q'S')$ also ex-
ceeds the rainfall (in this case $q'S'$ actually represents
a saturation deficit), then

III.C.7
$$F_\theta = -\frac{L}{c_p}\left(\frac{p_o}{p}\right)^{\kappa} q_r S'$$

$$F_q = -q_r S' \quad .$$

Otherwise, equations C.5 and C.6 are used (F_q is negative),
evaporating an amount of water just equal to F_q. The re-
maining water descends to a lower height.

This procedure is first applied near the top of the
model domain. If any water vapor condenses, it is assumed

to rain out with 100% efficiency to the next lower level, leaving the original level just saturated. Variable grid spacing is taken into account by weighting q_r at level $j + 1$ by the factor

$$\frac{\Delta Z_{j+1}}{\Delta Z_j} \quad ,$$

where j is the vertical grid increment.

The sequence begins anew at the next lower level. If this air is supersaturated, then the liquid water from this level is added to any which entered from above. Otherwise, water will evaporate into unsaturated air until it just saturates it. Any net liquid water is adjusted for grid spacing and descended another level.

There is a dependency of S' upon the initial value of θ in C.3. (Recall that S' is the condensate fraction of the excess moisture). Therefore, the sequence represented by C.1 through C.7 is iterated to insure that the correct solutions are obtained. The convergence criteria are 0.05 K for potential temperature and 0.005 g/kg for the specific humidity. Both criteria are satisfied simultaneously. No more than 17 iterations were ever needed for the south Florida simulations.

When a net moisture excess occurs in the air at the first model grid point above the ground surface, it is considered to be rain. The rain is transformed into a flux and added to the turbulent vapor flux of the atmosphere. In this way it enters the soil, thereby affecting the moisture content and altering the surface energy balance.

The total rainfall in a grid box is partitioned between bare ground and vegetated surfaces (if any) using the canopy shielding factor (defined later). The amount of rain reaching the ground beneath the canopy is depleted by interception, while the rain over bare soil is undiminished. No assumption is made regarding the temperature of the rainwater due to the arbitrary way in which it would have to be assigned.

A final note about the rain scheme. One way in which the believability of a precipitation scheme can be checked is by evaluating the precipitation rate of fall. In the parameterization presented here, tests indicate that during the early stages of rainfall, the rate of fall can be rather slow, taking up to two to three hours for rain to reach the ground from a height of 1.2 kilometers. This reflects the imposed condition that all levels below cloud base must saturate before rain can descend through a layer. However, once a column has saturated, it is possible that water vapor which condenses at cloud base could find its way to the surface in a single time step (i.e. 180 seconds)! Presumably some entrainment of drier air into the column would preclude this very unrealistic possibility. In any event, this is the price paid for the simplicity sought in a rain scheme.

D. Soil Physics

The soil temperature is treated similarly to Mahrer and Pielke (1977). The surface temperature is computed from the surface energy balance equation B.1 . Below the surface only vertical diffusion is permitted using

III.D.1
$$C \; \frac{\partial T_s}{\partial t} = \frac{\partial H_s}{\partial z} \quad ,$$

where the vertical heat flux in the soil $H_s = \lambda \dfrac{\partial T_s}{\partial z}$.

The volumetric heat capacity, C, is defined by

III.D.2
$$C = (1 - \eta_s) \; C_i + \eta \; .$$

Recall that η is the volumetric moisture content and η_s is the saturation value, which is also the porosity. C_i is the dry soil volumetric heat capacity for soil type i. D.2 agrees with Sellers (1965) and De vries (1975), where the heat capacity of the air has been omitted since it is neggligibly small.

The thermal conductivity, λ (cal/sec/cm/^{0}C), can vary over several orders of magnitude as a soil dries out. To account for this, a mean curve was fitted to the data plotted in Figure 4 in Al Nakshabandi and Kohnke (1965). Its functional form is

$$\lambda = \exp(- (P_f + 2.7)), \; P_f \leq 5.1$$

III.D.3

$$\lambda = 0.00041 \quad\quad , \; P_f > 5.1 ,$$

where P_f is the base ten logarithm of the magnitude of the moisture potential, ψ (cm). Equations D.3 are plotted in Figure 2. Al Nakshabandi and Kohnke demonstrated that the

Figure 2. Dependence of soil conductivity upon moisture potential. P_f is the magnitude of the base ten logarithm of the moisture potential. The thermal conductivity, λ, is plotted in units of 10^{-2} cal/cm/sec/^{0}C . This diagram corresponds to Figure 4 in Al Nakshabandi and Kohnke (1965).
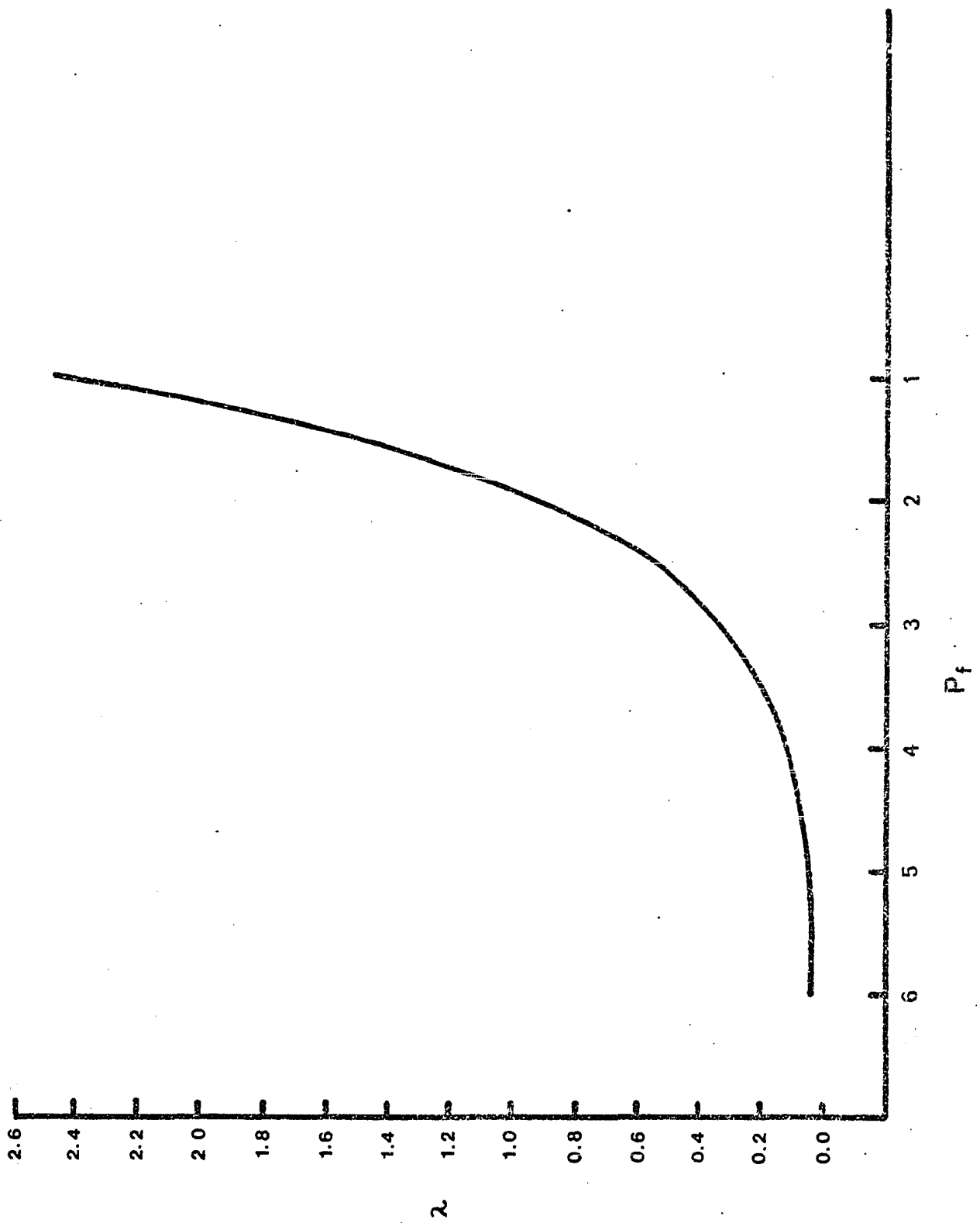
relationship between thermal conductivity and moisture potential is virtually independent of the soil textural class under consideration.

Soil moisture is treated somewhat differently. Philip (1957) presented detailed relationships for computing the temporal fluctuations in soil moisture content. Sasamori (1970) and Garrett (1978) both used Philip's approach in their numerical atmospheric models. Since only domain-averaged soil fluxes are desired here and further since detailed soil data are not available for either initializing or verifying the model at a specific site (i.e. south Florida), a simpler approach seems justified.

The prognostic equation for soil moisture is

III.D.4
$$\rho_w \frac{\partial \eta}{\partial t} = \frac{\partial W_s}{\partial z} \quad .$$

W_s is the moisture flux within the soil (defined as positive downward) and z is a vertical coordinate within the soil profile, defined (as it is in the atmosphere) as positive downward.

The soil moisture flux (which includes both vapor and liquid phases) is defined by

III.D.5
$$W_s = K_\eta \rho_w \frac{\partial (\psi + z)}{\partial z} \quad ,$$

where ρ_w is the density of water (g/cm^3).

The hydraulic conductivity (K_η) accounts for gravity drainage, while the moisture potential (ψ) represents the work required to extract water against capillary and adhesive forces. Another form of this equation is

III.D.6
$$W_s = D_\eta \rho_w \frac{\partial \eta}{\partial z} + K_\eta \rho_w \quad ,$$

noting that the diffusivity is merely $\quad D_\eta = K_\eta \frac{\partial \psi}{\partial \eta} \quad .$

The variables K_η, D_η and ψ are related to η using a set of simple relationships provided in Clapp and Hornberger (1978):

III.D.7
$$\psi = \psi_s \left(\frac{\eta_s}{\eta} \right)^b \quad ,$$

III.D.8
$$K_\eta = K_{\eta_s} \left(\frac{\eta}{\eta_s} \right)^{2b+3} \quad ,$$

III.D.9   and
$$D_\eta = - \frac{b K_{\eta_s} \psi_s}{\eta} \left(\frac{\eta}{\eta_s} \right)^{b+3} \quad .$$

Subscript s refers to saturation. The exponent b is a function of the USDA soil textural class, as are ψ_s, K_{η_s} and η_s. Clapp and Hornberger provide a table of values for each of these four parameters as they are applied to eleven soil classes. This data is reproduced here as Table I. The data for peat soil is from Rijtema (1970).

When a layer of foliage is present, the transpiration loss of soil moisture must be taken into account. Unlike the bare soil process which depletes moisture from the surface downward, the transpiration uptake is effected throughout the root zone. Following Molz and Remson (1970), Whisler, Klute and Millington (1968) and Nimah and Hanks (1973), D.4 is modified for root uptake of soil moisture. It takes the form

III.D.10
$$\frac{\partial \eta}{\partial t} = \frac{\partial}{\partial z} \left(D_\eta \frac{\partial \eta}{\partial z} \right) + \frac{\partial K_\eta}{\partial z} + A(z) \quad .$$

Table I. Soil parameters as a function of eleven USDA (United States Department of, Agriculture) textural classes plus peat. Units for soil porosity (η_s) are cm^3/cm^3, saturated moisture potential (ψ_s) is given in cm and the saturated hydraulic conductivity (K_{η_s}) is expressed in cm/sec. Exponent b is dimensionless. Permanent wilting moisture content (η_{wilt}) is in cm^3/cm^3 and it corresponds to a suction of 153 meters (15 bar). Dry volumetric heat capacity (c_i) is in cal/cm/ ^oC. The first four variables for the USDA textures are reproduced from Clapp and Hornberger (1978) (with permission).

Soil Type	n_s	ψ_s	K_{η_s}	b	n_{wilt}	c_i
SAND	.395	-12.1	.01760	4.05	.0677	.350
LOAMY SAND	.410	-9.0	.01563	4.38	.0750	.336
SANDY LOAM	.435	-21.8	.00341	4.90	.1142	.321
SILT LOAM	.485	-78.6	.00072	5.30	.1794	.304
LOAM	.451	-47.8	.00070	5.39	.1547	.290
SANDY CLAY LOAM	.420	-29.9	.00063	7.12	.1749	.281
SILTY CLAY LOAM	.477	-35.6	.00017	7.75	.2181	.315
CLAY LOAM	.476	-63.0	.00025	8.52	.2498	.293
SANDY CLAY	.426	-15.3	.00022	10.40	.2193	.281
SILTY CLAY	.492	-49.0	.00010	10.40	.2832	.275
CLAY	.432	-40.5	.00013	11.40	.2864	.260
PEAT	.863	-35.6	.00080	7.75	.3947	.200

The last term on the right-hand side of D.10 is a root extraction term. It functions as a sink of soil moisture. The strength of the root extraction term is dependent upon such factors as root distribution, soil moisture content, soil type, depth within the soil and the strength of the atmospheric forcing which drives the transpiration process. A simple form for the root extraction term, borrowed from Molz and Remson, is

$$\text{III.D.11} \qquad A(z) = E_{tr} \left[\frac{R(z) \, D_\eta}{\int_{G-r}^{G} R(z) \, D_\eta \, dz} \right].$$

E_{tr} is the transpiration rate per unit area, $R(z)$ is a root distribution function (vertical profile only), r is the root depth and G is the ground surface. Internal resistance to flow within the roots themselves as well as the effect of osmotic potential are both neglected.

Molz and Remson used D.11 in a model with which they simulated the loss of soil moisture due to birdsfoot trefoil in a Pachappa sandy loam soil. Their results verified rather well against sampled data over many days. These results and others led them to conclude that a macroscopic approach using an extraction term can reasonably approximate the microscopic flow of soil moisture to individual roots. The method is simple, easily applied in a model and it may well be valid for moderate or even perhaps low root densities.

E.   Vegetation Parameterization

Deardorff (1978) described a bulk treatment of vegeta-
tion, whereby a single-level canopy assumed the properties
of a large leaf. The computation sequence for the vegeta-
tion is illustrated in Figure 3. An energy balance, much
like that for the ground surface, is applied to the canopy.
The canopy storage is assumed to be negligible (Deardorff,
1978: Monteith, 1975).

III.E.1
$$(R_{sw}^{\downarrow} - R_{sw}^{\uparrow})\Big|_h + (R_L^{\downarrow} - R_L^{\uparrow})\Big|_h - (R_{sw}^{\downarrow} - R_{sw}^{\uparrow})\Big|_G$$

$$- (R_L^{\downarrow} - R_L^{\uparrow})\Big|_G + H_f + LE_f = 0$$

These fluxes are illustrated schematically in Figure 4.
The first two terms are the net short wave and the net long
wave fluxes, respectively, evaluated at canopy height. The
third and fourth terms represent the same radiative fluxes,
computed at the surface of the ground beneath the canopy.
Lastly H_f and LE_f are the sensible and latent heat fluxes,
respectively, applied to the canopy.

The short and long wave fluxes at the top of the canopy
are defined by

III.E.2
$$R_{sw}^{\uparrow}\Big|_h = \left[(1-\sigma_f)\, a_G + \sigma_f\, (a_f + a_n)\right]\, R_{sw}\Big|_h$$

III.E.3
$$R_L^{\uparrow}\Big|_h = (1-\sigma_f)\left[\varepsilon_G \sigma T_G^4 + (1-\varepsilon_G)\, R_L^{\downarrow}\Big|_h\right] +$$

$$\sigma_f \left[\varepsilon_f \sigma T_f^4 + (1-\varepsilon_f)\, R_L^{\downarrow}\Big|_h\right] \quad ,$$

where a_f is the foliage albedo and ε_f and ε_G are the emissiv-

Update Radiation Terms

Assign Constants

Compute u_{af}, c_f, r_s, r_a

Calculate T_{af}, q_s, f'

Calculate q_{af}

Compute H_f, E_f, E_{tr}

Solve Foliage Energy

Balance Equation For T_f

NO ———— Has H_f Converged

Within 0.01 cal/cm^2/sec?

YES

Compute H_0, E_0

Solve For Soil Parameters
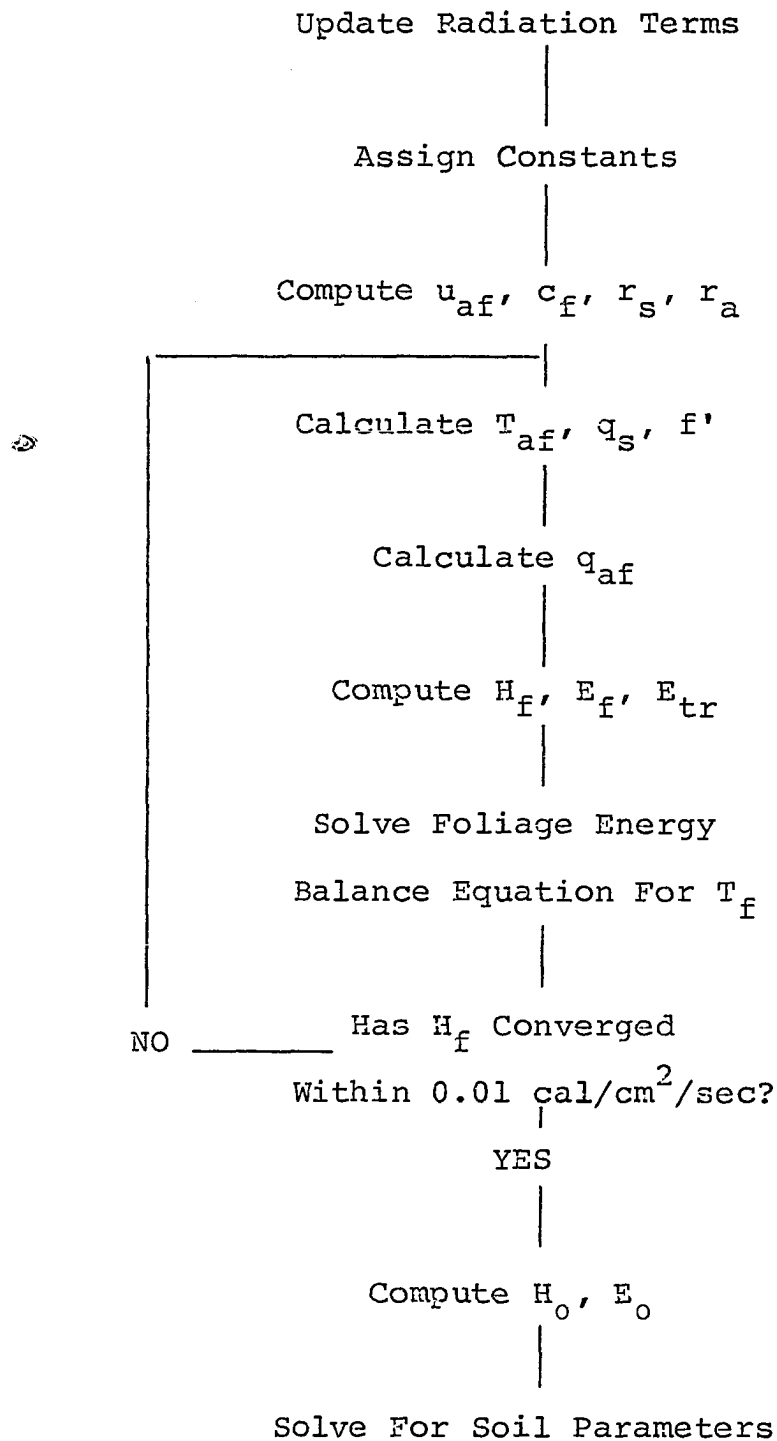
Figure 3. Computation sequence for the vegetation scheme.

Figure 4. A schematic representation of the energy fluxes for the model. Both bare ground and a vegetation canopy are shown. Note that the assumption of a dense canopy does not permit penetration of solar radiation through the canopy. Also note that the direction of the arrows does not necessarily indicate the direction of the latent and the sensible heat fluxes.

CANOPY LEVEL

SHORTWAVE
LONGWAVE
SENSIBLE
LATENT
SOIL
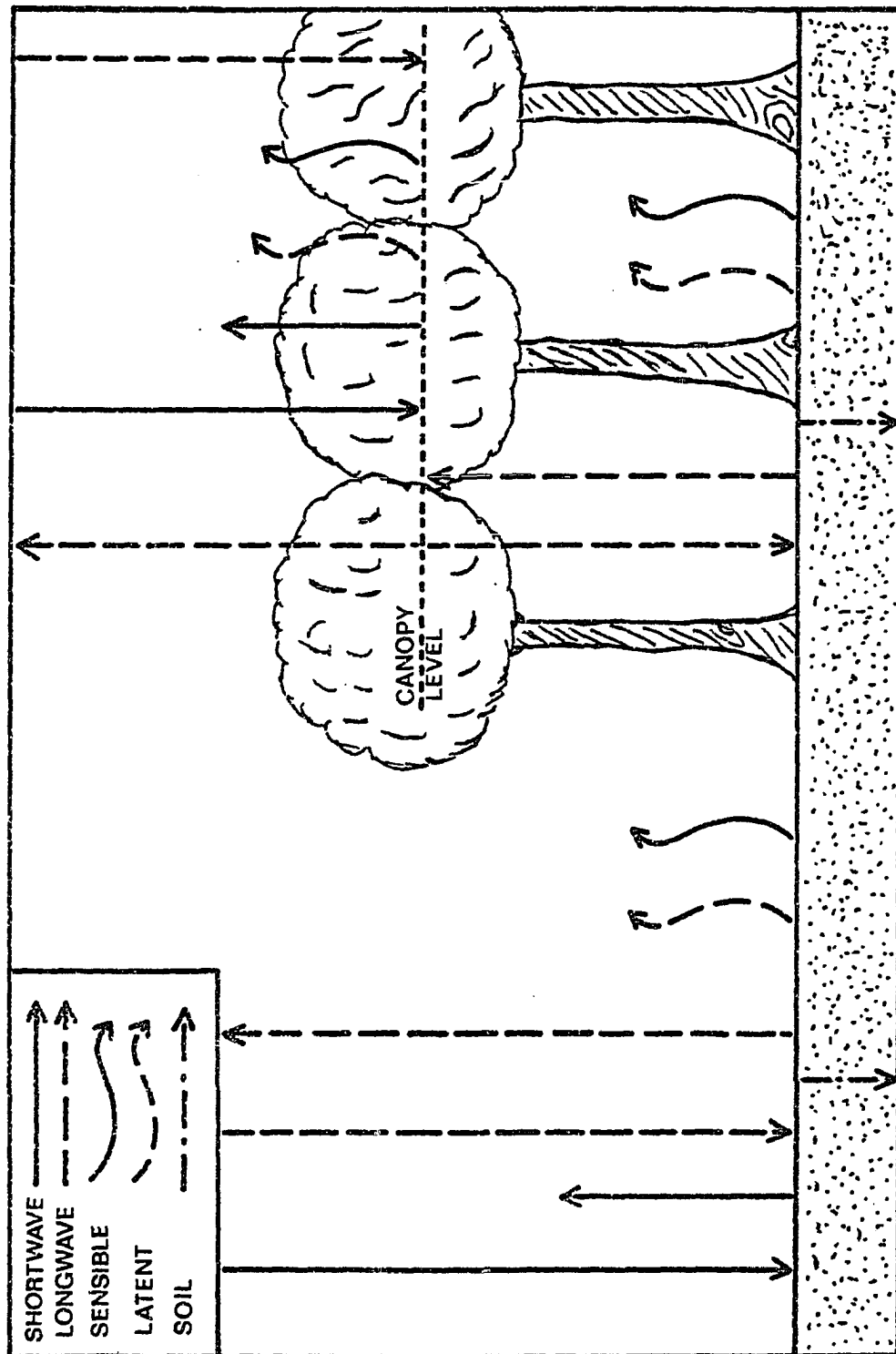
ities of the foliage and the ground, respectively. The shielding factor, σ_f, represents the fractional coverage of the ground by the canopy. $R_{sw}^{\downarrow}\big|_h$ is computed from B.14 (less the albedo terms) and $R_L^{\downarrow}\big|_h$ comes from B.21. T_f is the leaf temperature. The ground surface albedo is just

III.E.4
$$a_G = a_n + a_s \quad .$$

The radiative fluxes at the ground beneath the canopy are

III.E.5
$$R_L^{\uparrow}\big|_G = (1-\sigma_f)\left[\varepsilon_G \sigma T_G^4 + (1-\varepsilon_G) R_L^{\downarrow}\big|_h\right] + \sigma_f\left[\varepsilon_G \sigma T_G^4\right.$$
$$\left. + (1-\varepsilon_G)\varepsilon_f \sigma T_f^4\right] \;/\; (\varepsilon_f + \varepsilon_G - \varepsilon_f \varepsilon_G) \quad ,$$

III.E.6
$$R_L^{\downarrow}\big|_G = (1-\sigma_f) R_L^{\downarrow}\big|_h + \sigma_f\left[\varepsilon_f \sigma T_f^4 + (1-\varepsilon_f)\varepsilon_G \sigma T_G^4\right] /$$
$$(\varepsilon_f + \varepsilon_G - \varepsilon_f \varepsilon_G) \quad ,$$

III.E.7
$$R_{sw}^{\uparrow}\big|_G = a_G (1-\sigma_f) R_{sw}^{\downarrow}\big|_h \quad ,$$

III.E.8 and
$$R_{sw}^{\downarrow}\big|_G = (1-\sigma_f) R_{sw}^{\downarrow}\big|_h \quad .$$

When vegetation completely shades the ground, E.5 and E.6 become the radiative flux between two parallel plates (Fleagle and Businger, 1963 , as used by Deardorff, 1978).

Substituting E.5 through E.8 into E.1 and rearranging results in a condensed balance equation for the foliage layer.

III.E.9
$$\sigma_f\left[(1-a_f-a_n)R_{sw}^{\downarrow}\big|_h + \varepsilon_f R_L^{\downarrow}\big|_h + \left(\frac{\varepsilon_f \varepsilon_G}{\varepsilon_f + \varepsilon_G - \varepsilon_f \varepsilon_G}\right)\sigma T_G^4\right.$$

$$-\left(\frac{\varepsilon_f + 2\varepsilon_G - \varepsilon_f \varepsilon_G}{\varepsilon_f + \varepsilon_G - \varepsilon_f \varepsilon_G}\right) \varepsilon_f \sigma T_f^4 \Bigg] + H_f + LE_f = 0 \quad .$$

In the model E.9 is used to update the foliage temperature. The foliage specific humidity is obtained from

III.E.10 $\qquad q_f = f' q_s(T_f) + (1-f') q_{af}$,

with the restriction that

$$q_f \leq q_s(T_f) \quad .$$

The fraction of the potential evapotranspiration, f', is defined later.

The air flow within the modelled plant canopy (u_{af}) is written as

III.E.11 $\qquad u_{af} = 0.83 \; C_G^{\frac{1}{2}}\Big|_f \; u_a \quad .$

The term u_a is the wind speed at the first atmospheric level above the canopy, whereas $C_G\big|_f$ is a non-dimensional transfer coefficient applied at canopy height. Thom (1971) suggested the functional form

III.E.12 $\qquad C_G = \left[\dfrac{k}{\ln \dfrac{z - d}{z_o}}\right]^2 \quad ,$

where d is the zero plane displacement height of the vegetation. This equation is formally valid for a neutrally stratified surface layer. No modification was made for non-neutral stability. The term $C_G^{\frac{1}{2}} u_a$ approximates the friction velocity (Deardorff, 1978).

The canopy air temperature and specific humidity are computed somewhat differently. The properties of the canopy

air are assumed to be intermediate between those of the free air and the foliage. Using Deardorff's suggested weighting factors, the equations are

III.E.13
$$T_{af} = 0.3T + 0.6T_f + 0.1T_G$$

III.E.14
$$q_{af} = 0.3q + 0.6q_f + 0.1q_G \quad .$$

Unsubscripted variables refer to the free air at the first atmospheric level above the ground in the model.

The sensible heat flux from the leaves is defined by

III.E.15
$$H_f = 1.1L_I \rho c_p u_{af} \ (T_{af} - T_f)c_f \ (c_p/\pi) \quad ,$$

where c_f is a non-dimensional transfer coefficient written as

III.E.16
$$c_f = 0.01 \ (1 + 30/u_{af}) \quad (u_{af} \ \text{in cm/sec}) \quad .$$

L_I is the leaf area index (assumed to be 7 (Deardorff, 1978)), the factor 1.1 accounts for stems, trunks and branches, and the second term in E.16 is a free convection enhancement term (Deardorff, 1978). The last term in E.15 merely transforms the flux into a potential temperature form, which is consistent with the bare soil fluxes.

In order to compute the latent heat flux, the bulk stomatal resistance must be known. A generalized resistance (Deardorff) is expressed by

III.E.17
$$r_s = r_c \left[\frac{(R_{sw})_{MAX}}{0.3(R_{sw})_{MAX} + (R_{sw}|_h)_{NET}} + \left(\frac{\eta_{wilt}}{\eta_{root}}\right)^2 \right] \quad .$$

$(R_{sw})_{MAX}$ is the maximum net solar insolation for a cloudless sky, r_c is a resistance coefficient dependent upon plant type,

η_{wilt} is the permanent wilting percentage of the soil moisture and η_{root} is the minimum predicted value of the soil moisture in the root zone. The notation $|_h$ refers to the top of the plant canopy.

The resistance of the air is specified as

III.E.18
$$r_a = (c_f u_{af})^{-1} \quad .$$

Once each resistance is known, it is possible to compute the fraction of the potential evapotranspiration from the foliage.

III.E.19
$$f' = 1 - \Delta\left(\frac{r_s}{r_s + r_a}\right)\left[1 - \left(\frac{W_L}{W_I}\right)^{.67}\right] \quad .$$

The term $\Delta = 0$ if condensation is occurring onto the leaf surface. It equals one otherwise. W_L is the liquid water per unit leaf area on the surface of the leaves and W_I is the maximum interception storage (depth per unit leaf area). Many investigators have found that interception storage estimates must take rainfall into account (Clark, 1940; Ovington, 1954; Sim, 1972; Burgy and Pomeroy, 1958; and Helvey and Patric, 1965). Rainfall weight imposes a physical limitation on the storage at any given instant. And evaporation from the leaf surfaces can enhance the total interception from a given rain event. Thus heavy rains can yield a greater total interception, yet light rainfalls can produce the larger percentage interception. For the sake of simplicity, the effects of rainfall rate are ignored here. W_I is assigned a representative value for each type of plant.

The predictive equation for dewfall or rainfall on the surfaces of the leaves is

III.E.20
$$\frac{\partial W_L}{\partial t} = \sigma_f P_r + (E_f - E_{tr}) \qquad 0 \leq W_L \leq W_I \quad .$$

P_r is the precipitation rate. The second term is just the evaporation of liquid water. Since rainfall can be intercepted by the foliage, the net rainfall reaching the ground is adjusted. Hence,

$$P_G = (1 - \sigma_f) P_r + \sigma_f \left[P_r - \frac{W_I - W_L}{\Delta t} \right], 0 \leq W_L \leq W_I \quad ,$$

III.E.21

$$P_G = P_r \qquad\qquad , \quad W_L = W_I \quad .$$

The precipitation rate at the ground is P_G.

The exponent 0.67 in E.19 approximates the agglomeration of an evaporating film of water into discrete droplets, thereby covering less leaf surface and accelerating the evaporative flux somewhat from what it would be if a unit exponent were used. This is evident from the following equation, which defines the total moisture flux (i.e. evaporation plus transpiration) from the leaves.

III.E.22
$$E_f = 1.1 L_I \rho f' c_f u_{af} \left(q_{af} - q_s(T_f) \right) \quad .$$

$q_s(T_f)$ is the saturation specific humidity at the foliage temperature. The transpiration rate taken alone is then

III.E.23
$$E_{tr} = 1.1 L_I \rho c_f u_{af} \left(q_{af} - q_s(T_f) \right)$$
$$\left(\frac{r_a}{r_a + r_s} \right) \left(1 - \left(\frac{W_L}{W_I} \right)^{.67} \right) \quad .$$

This is the flux in the root extraction term defined in D.11 .

The presence of a vegetative cover necessitates modification of the surface energy balance equation. Following Deardorff, it assumes the form

III.E.24
$$(R_{sw}^{\downarrow} - R_{sw}^{\uparrow})\big|_G + R_L^{\downarrow}\big|_G + \sigma_f(H_o + LE_o) +$$

$$(1 - \sigma_f)\ (\rho L u_* q_*' + \rho c_p u_* \theta_*) - \lambda\ \frac{\partial T_s}{\partial z}\bigg|_G$$

$$- R_L^{\uparrow}\big|_G = 0 \qquad .$$

The first term is the net short wave flux (E.7 and E.8), the second term is the incoming long wave flux (E.6), H_o is the flux of sensible heat and LE_o is the latent heat flux. The preceding two fluxes are both evaluated beneath the canopy. The next two terms are the latent and the sensible heat fluxes over bare soil. Next is the surface soil heat flux and last is the upward long wave flux from the ground (E.5).

The bare soil turbulent fluxes for sensible and latent heat are calculated from A.6. Beneath the canopy, these fluxes are described by

III.E.25
$$H_o = \rho c_p\ C_G\big|_G\ u_{af}\ (T_{af} - T_G)\ (c_p/\pi)$$

III.E.26
$$E_o = \rho L\ C_G\big|_G\ u_{af}\ (q_{af} - q_s(T_G))\qquad .$$

Recall that π is the scaled pressure, in this instance at the ground surface. $C_G\big|_G$ is scaled to the roughness length of bare ground. In this model it assumes a value of 0.0057 (Deardorff, 1978) .

The total sensible and latent fluxes to the atmosphere become

III.E.27
$$H_{TOT} = \sigma_f (H_f + H_o) + (1 - \sigma_f) \theta_* \rho c_p u_*$$

$$E_{TOT} = \sigma_f (E_f + E_o) + (1 - \sigma_f) q_* \rho L u_* \quad .$$

Lastly the surface layer friction parameters are weighted as linear functions of the values computed over the bare soil and the effective values computed both over and beneath the vegetation. Hence,

$$\theta_*^\dagger = (\theta_* \big|_{BARE}) (1-\sigma_f) + \left[\frac{H_o}{C_G \big|_G^{1/2}} + \frac{H_f}{C_G \big|_f^{1/2}} \right]$$

$$\left(\frac{1}{u_{af} \rho c_p} \right) \sigma_f$$

$$u_*^\dagger = (1-\sigma_f) (u_* \big|_{BARE}) + \sigma_f (C_G \big|_f^{1/2} u_a)$$

III.E.28
$$q_*^\dagger = (1-\sigma_f) (q_* \big|_{BARE}) + \sigma_f \left[\frac{E_o}{C_G \big|_G^{1/2}} + \frac{E_f}{C_G \big|_f^{1/2}} \right]$$

$$\left(\frac{1}{u_{af} \rho L} \right)$$

$$L_*^\dagger = \left(\frac{\theta u_*^{\dagger 2}}{k_o g \theta_*^\dagger} \right) \quad .$$

IV. <u>Numerical</u> <u>Techniques</u>

A.   Advection and Diffusion

Numerical solution of the predictive equations is accomplished in two steps: advection, then diffusion. The advective derivatives are approximated with cubic splines using upstream interpolation. Mahrer and Pielke (1978) describe how the splines are applied to this model. It is a very accurate scheme, which preserves phase very well and it suffers only slight damping (Long and Pepper, 1979).

The generalized Crank-Nicolson scheme of Paegle et al. (1976) is used to compute turbulent exchange terms. For any dependent variable A, the scheme assumes the form:

IV.A.1
$$\frac{A_j^{N+1} - A_j^N}{\Delta t} =$$

$$(1 - \delta) \left(\frac{K_{j+1/2}\left[A_{j+1}^N - A_j^N\right] - K_{j-1/2}\left[A_j^N - A_{j-1}^N\right]}{\Delta z_j \quad \Delta z_{j-1}} \right)$$

$$+ \delta \left(\frac{K_{j+1/2}\left[A_{j+1}^{N+1} - A_j^{N+1}\right] - K_{j-1/2}\left[A_j^{N+1} - A_{j-1}^{N+1}\right]}{\Delta z_j \quad \Delta z_{j-1}} \right).$$

The time step is N, the vertical grid index is j and Δz is a vertical grid interval. K is an eddy exchange coefficient. The conventional Crank-Nicolson scheme ($\delta = 0.50$) has been widely used, but it demands a fairly small time step to maintain stability. .   g (1975) has shown that by choosing $\delta > 0.50$ the scheme is unconditionally stable. For the

value of δ (0.75) used in these simulations, phase and amplitude are well behaved. The generalized Crank-Nicolson scheme is applied in both the atmosphere and the soil.

A discriminating low pass filter devised by Long (personal communication) is used in lieu of explicit horizontal diffusion. It eliminates $2\Delta x$ grid length instability completely which is desirable. The weighting coefficient is chosen to give some damping out to a wavelength of $4\Delta x$, but very little at larger wavelengths. This filter is described in Mahrer and Pielke (1978).

B.   Soil Layer

Soil characteristics for each grid cell can be specified independently. A maximum of eleven soil types in addition to peat are available. A list of values for the dependent variables of each soil type is provided in Table I. Hydraulic conductivities and heat capacities were calculated from a few known values for sand, clay, loam and peat, using the percentage weight compositions of Petersen, Cunningham and Matelski (1968). Permanent wilting percentages were computed assuming a suction of 153 meters (i.e. 15 bar).

The soil moisture is updated by first computing the surface moisture potential from a diagnostic relationship:

IV.B.1 $$\psi_G = \psi_{G-1} + \Delta z_G \left[\left\{ (W_s)_G \ / \ (K_\eta)_G \right\} - 1 \right] \quad .$$

This equation is just a reorganization and a finite difference representation of III.D.5. $(W_s)_G$ is the soil moisture flux at the surface. Continuity of mass across the air-soil interface is insured by demanding that

IV.B.2 $$W_a - (W_s)_G = 0 \quad ,$$

where W_a is the turbulent atmospheric moisture flux defined as

IV.B.3 $$W_a = \rho u'_* q'_* \quad .$$

At each time step $(W_s)_G$ is initially determined from III.D.5. Thereafter it is weighted by

IV.B.4 $$(W_s)_G^{n+1} = \delta \ (W_s)_G^n + (1 - \delta) \ W_a, \quad 0 \le \delta \le 1 \quad .$$

Here δ is a weighting factor. Superscript n refers to the iteration of a guess value. This flux is used to update ψ_G

in IV.B.1. Then ψ_G is used to update η and then K_η and D_η at the surface. Philip (1957) showed that the relative humidity at the soil surface is related to the moisture potential by

IV.B.5
$$h = \exp\left[-\left(\frac{g\psi_G}{R_v T_G}\right)\right].$$

R_v is the gas constant for water vapor. Now the saturation vapor pressure at the soil surface is

IV.B.6
$$e_s(T_G) = 6.1078 \exp\left[\left(\frac{T_G - 273.16}{T_G - 35.86}\right)(17.269)\right],$$

and the saturation specific humidity becomes

IV.B.7
$$q_s(T_G) = 0.622\left(\frac{e_s(T_G)}{P - .378 \, e_s(T_G)}\right).$$

P is the pressure in mb. The soil surface specific humidity is then calculated as

IV.B.8
$$q_G = h \, q_s(T_G).$$

Thus q_* and subsequently W_a can be updated. The total sequence is iterated until

$$\left|\frac{W_a - (W_s)_G}{W_a}\right| < 0.001.$$

Fastest convergence is assured when the weighting factor δ is greater than 0.5. When the soil becomes fairly dry (i.e. $h < 0.70$) then it is necessary that δ be strongly skewed toward 1.0 to assure convergence. Once the surface moisture is computed, then equation III.D.10 is used to apply subsurface moisture diffusion.

The surface temperature is calculated next from the

soil surface energy balance equation using the Newton-Raphson technique. It is applied in the same manner as Mahrer and Pielke (1978). Lastly temperature diffusion is computed using the thermal conductivities which are obtained from the updated soil moisture profile.

C. Vegetation Canopy

A variable number of foliage canopies can be accommodated by the model. However, only one type of vegetation is permitted in each grid cell. Variables which are dependent upon the type of vegetation are the foliage albedo, shielding factor, interception storage, roughness length, zero-plane displacement height, foliage emissivity and the stomatal resistance coefficient.

The bulk aerodynamic equations used to estimate the heat and the moisture fluxes require an estimation of a transfer coefficient. In these simulations only a general treatment of grasslands and forests is simulated. The non-dimensional transfer coefficient C_G applicable to a grass canopy is scaled to a height of two meters above the ground, in the manner of Deardorff (1978). This assumes a mean grass height of 1.5 meters, a displacement height of 1.0 meter and a roughness height of 16.7 cm.

This approach is not easily applied to forests (assumed tree height is 20 meters). Little guidance for estimating the proper scaling height seems available. Intuitively a forest presents a rougher aerodynamic surface than does a grassland. In this study the transfer coefficient used for forests was larger than the grassland coefficient by a factor of 2.5. This factor originated in a study by Thom et al. (1975) which determined that aerodynamic relationships, derived for airflow over relatively smooth surfaces, consistently underestimated both the latent and the sensible

heat fluxes from Thetford forest (United Kingdom) by a factor of 2 - 3. This applied to unstable and near-neutral stratifications. Using the average factor, 2.5, the transfer coefficient for forests was 0.0498. It was comparable to an equivalent coefficient (0.087) computed by Leuning and Attiwill (1978) for a mature Eucalyptus forest. The mean tree height was 27.4 meters and the mean displacement height was 21.6 meters.

Once the forcing terms are computed, the foliage temperature is found by solving the foliage energy balance equation III.E.9 using the Newton-Raphson technique. The approach is analogous to that used for the soil surface temperature.

V. Boundary and Initial Conditions

Zero gradient lateral boundary conditions are specified for most variables. This means that

$$\frac{\partial}{\partial x} (u,v,\theta,q,\pi,S,Z_G) = \frac{\partial}{\partial y} (u,v,\theta,q,\pi,S,Z_G) = 0 \ .$$

The vertical velocity, which is diagnosed from the incompressible continuity equation, contains two component terms--one normal and one parallel to each lateral boundary. The normal component at the boundaries is set to zero such that

$$w^* = - \frac{\partial v}{\partial y} \text{ at } x = 1, \ x = 33$$

and

$$w^* = - \frac{\partial u}{\partial x} \text{ at } y = 1, \ y = 36 \ .$$

No lateral boundary conditions are specified for any of the soil, condensation or vegetation variables since they are only computed for interior points.

At the ground surface ($z^* = 0$) the boundary conditions are

$$u = v = w^* = 0$$

$$q_G = h \ q_s (T_G)$$

$$\theta_G = T_G \ (P_o/P)^{.286} \ .$$

The conditions imposed at the top of the model are

$$u = U_g \qquad , \ v = V_g$$

$$w^* = 0 \qquad , \ q\big|_s = 0.003 \text{ g/g}$$

$$\theta\big|_s = 326.2K \ , \ \Gamma_{TOP} = 0.00004 \text{ K/cm}$$

$$\pi = \pi(\bar{S}) - g(S - \bar{S}) / \theta\big|_s + \frac{\Gamma_{TOP} (S - \bar{S})}{2} \ .$$

Here Γ_{TOP} is the initial vertical potential temperature gradient at the top of the model.

Atmospheric data was obtained for July 17, 1973. The 1200 Z surface chart is shown in Figure 5. On that day south Florida was dominated by a high pressure ridge which bisected the peninsula. This ridge was an extension of the large Bermuda high situated to the east. By 0000 Z on the 18th, the ridge subdivided across the peninsula, resulting in a closed high over the Gulf of Mexico.

All simulations were initialized at sunrise on July 17. The 1200 Z (0700 LST) Miami sounding, used to define the synoptic scale, is plotted in Figure 6. The only noteworthy features on this day are a weak inversion near the ground and a moderate dry layer between about 650 and 530 mb.

Initial profiles of the atmospheric and soil variables are given in Table II. Some of the constants used are listed in Table III. The initial soil surface temperature was obtained by descending dry adiabatically from the first grid point in the atmosphere. The soil temperatures were then defined as departures from the surface value.

The soil moisture profile was generated in the same way, except that the surface moisture was initially assigned. Similarly, the type of soil, type of vegetation canopy and the foliage shielding factor were assigned. This will be discussed further in a later section.

The synoptic scale winds are assumed to be geostrophic above the initial boundary layer height (660 meters). Within

Figure 5. Surface analysis for the southeastern United States at 1200 Z (0700 LST) on July 17, 1973.
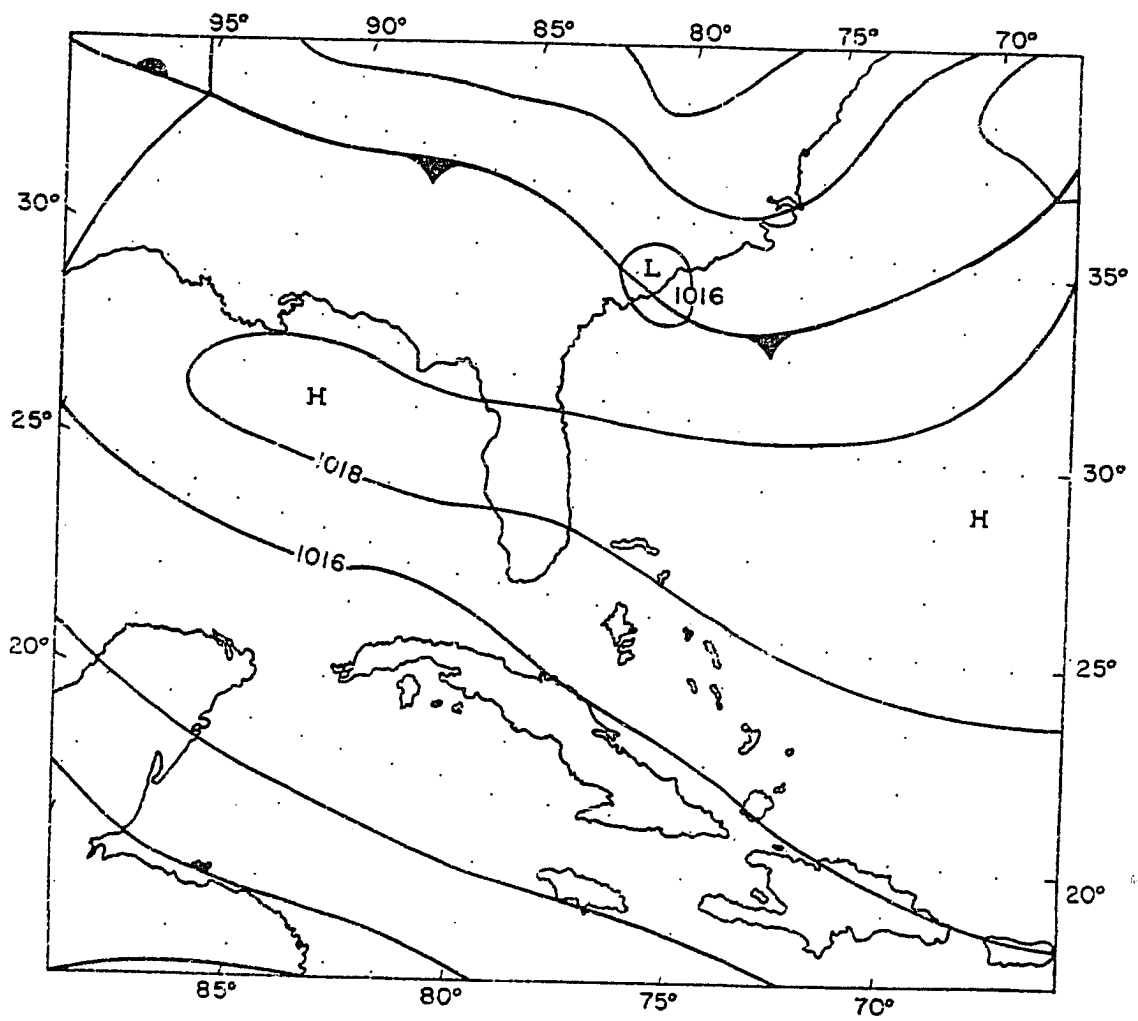
Figure 6. The Miami, Florida sounding taken at 1200 Z (0700 LST) on
July 17, 1973. The solid line is temperature, while the dew
point temperature is plotted as a dashed line.

MIAMI SOUNDING
17 JULY 1973
1200 GMT.

T ———
T_d ------

WIND SPEED

0 10 20 30 KNOTS
0 5 10 15 MS^{-1}
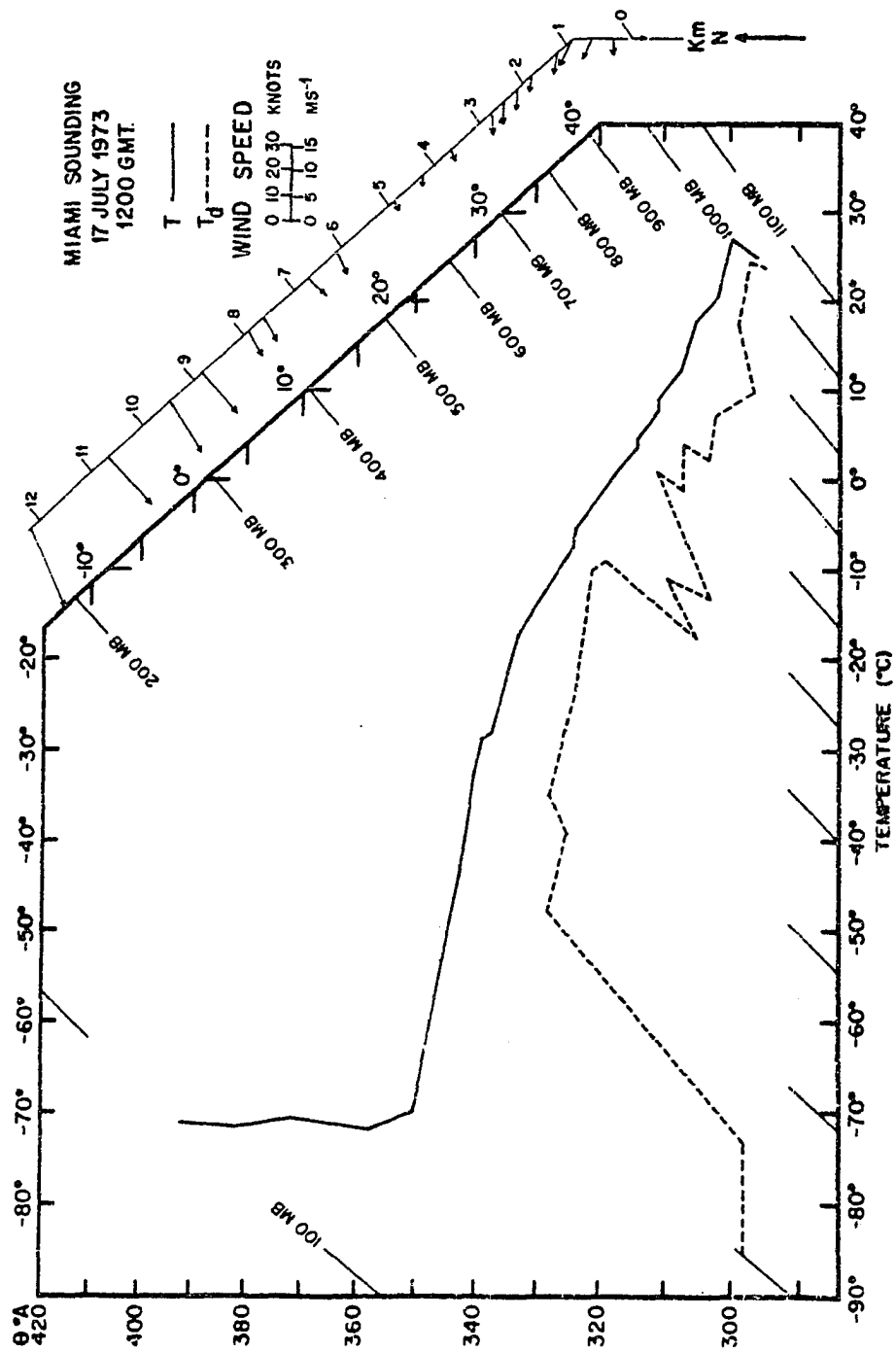
	ATMOSPHERE					SOIL		
Z^*(m)	Θ(K)	q(g/g)	windspeed (m/sec)	direction (degrees)	z(cm)	T_s(K)	$\Delta\eta$	R
6000	326.2	0.0030	4.72	58	0.0	301.03	0.00	0.000
5000	323.5	0.0035	2.24	63	0.5	301.17	0.00	0.036
4000	318.9	0.0026	2.80	90	1.5	301.54	0.00	0.073
3000	313.5	0.0054	4.00	90	3.0	301.98	0.00	0.073
2000	308.5	0.0076	4.00	90	5.0	302.98	0.00	0.109
1200	305.0	0.0092	4.57	110	8.0	302.81	0.00	0.145
700	301.5	0.0145	6.00	110	12.0	302.70	0.00	0.145
300	300.0	0.0165	6.04	94	18.0	304.99	0.00	0.146
100	299.8	0.0187	5.65	93	26.0	305.03	0.00	0.182
50	299.7	0.0189	5.40	93	36.0	305.28	0.00	0.091
25	299.6	0.0190	5.15	93	48.0	305.59	0.00	0.000
					62.0	304.33	0.00	0.000
					79.0	303.31	0.00	0.000
					100.0	303.08	0.00	0.000

Table II. Initial profiles of atmospheric and soil parameters. z is depth.

64

A. Atmospheric Constants

Surface pressure (P_o)	1018 mb
Surface specific humidity (q_G)	0.019 g/g
Geostrophic wind	6 m/sec from 110° (East)
Initial height of planetary boundary layer	600 meters
Filter weighting coefficient	0.05
Roughness length over land (z_o^*)	4 cm
Soil emissivity (ε_G)	1.00

B. Vegetation Constants

	Grass	Trees
Emissivity (ε_f)	0.95	0.98
Albedo (a_f)	0.20	0.10
Resistance coeff. $(r_c,\ sec/cm)$	4.00	8.00
Transfer coefficient $(C_G\vert_f)$	0.0199	0.0498
Interception storage $(W_I,\ cm)$	0.06	0.16

Table III. Constants used to specify the atmosphere and the surface.

Figure 7. Map of south Florida.

Figure 8. Outline of the computational grid.
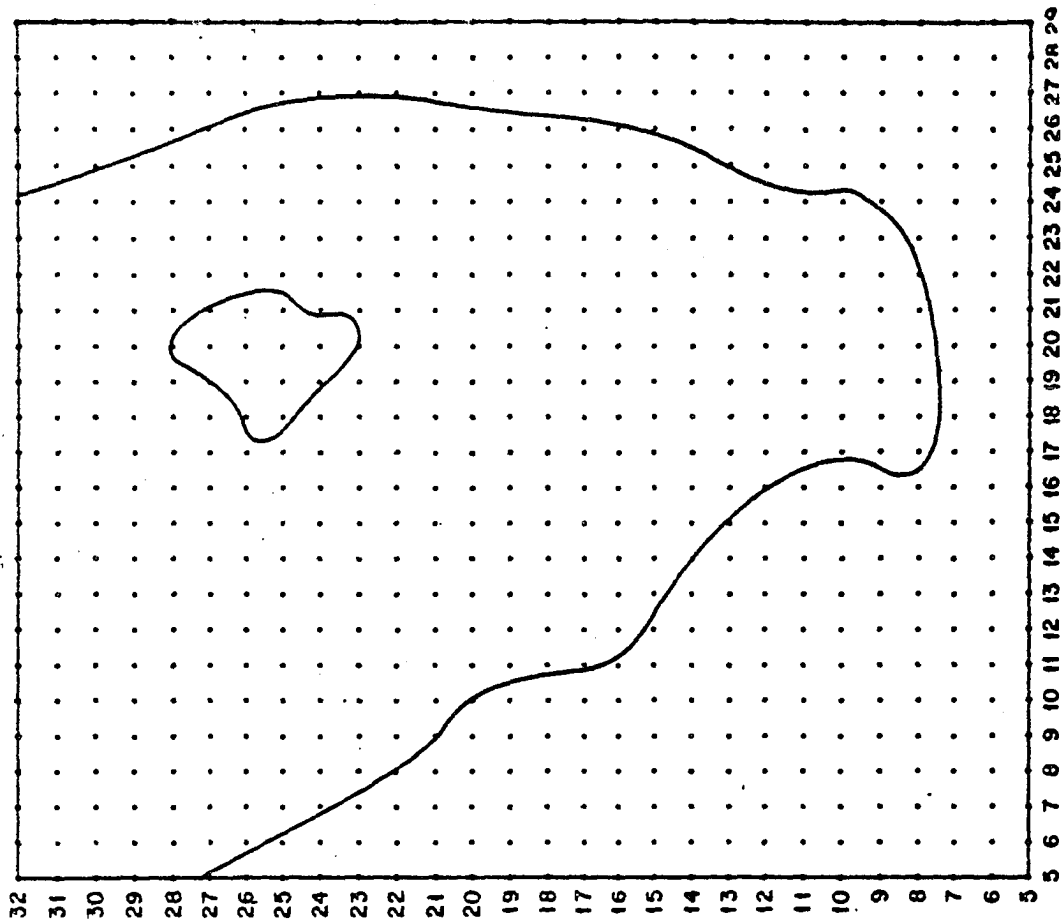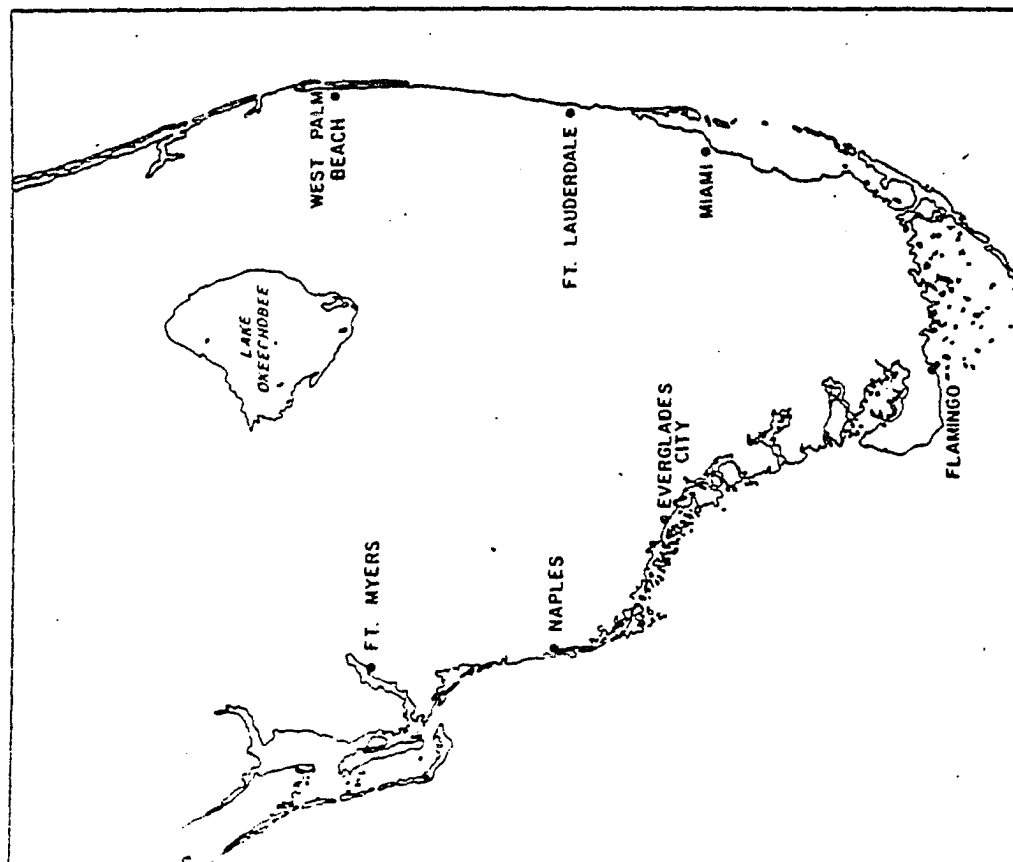
Figure 9.   Stencil of the atmospheric grid showing the relative positions of atmospheric variables in the horizontal and the vertical.
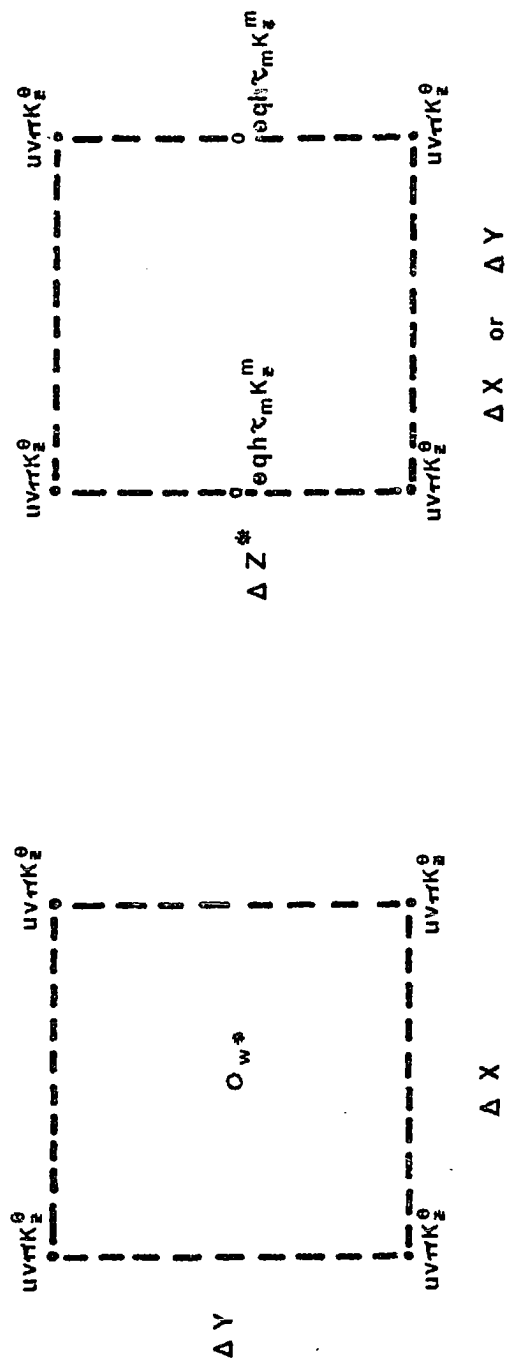
ATMOSPHERIC GRID

Figure 10. Stencil of the soil grid showing the relative positions of the soil variables in the horizontal and the vertical.

SOIL GRID

$T_s \eta h \, \psi D_\eta K_\eta$

$T_s \eta h \, \psi D_\eta K_\eta$

$T_s \eta h \, \psi D_\eta K_\eta$

$T_s \eta h \, \psi D_\eta K_\eta$

ΔY

ΔX

$T_s \eta h \, \psi D_\eta K_\eta$

$T_s \eta h \, \psi D_\eta K_\eta$

ΔZ
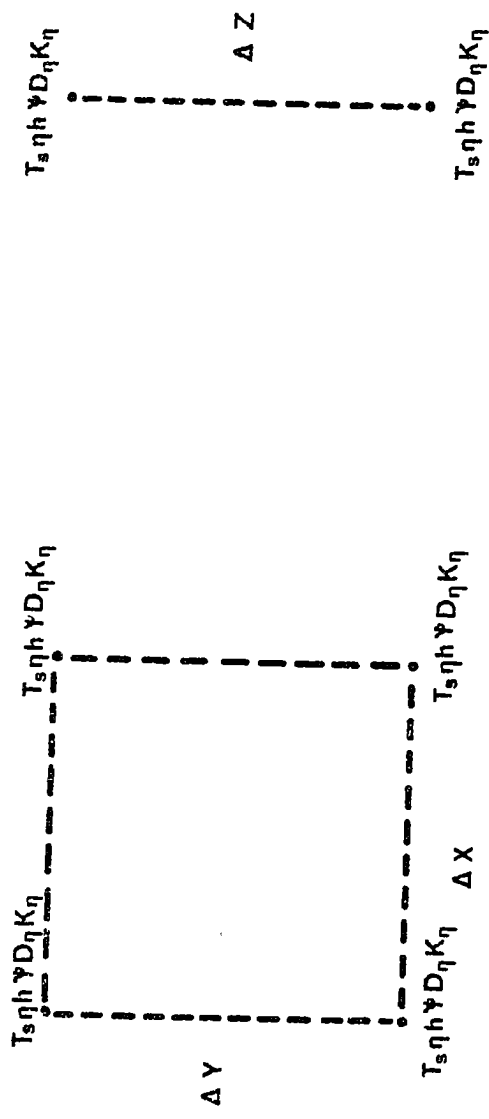
the boundary layer a balance is prescribed between the pressure gradient, coriolis and friction forces.

Charts depicting south Florida and the computational grid are given in Figures 7 and 8. The computational domain is characterized by a uniform horizontal grid spacing of 11 km in the interior. Near the lateral boundaries, the domain stretches until the grid increment becomes 55 km. This is done to reduce edge effects. In the horizontal plane the vertical velocities are centered in the grid cells, while the other variables are defined at the nodal points (Pielke, 1974).

Both the atmospheric and soil grids expand in the vertical dimension. The smaller grid increments are situated near the ground surface, where the strongest temperature and moisture gradients exist. Grid increments scale upward from 25 m to 1 km in the atmosphere and from 0.5 cm to 21 cm in the soil. This results in 11 levels in an atmosphere 6 km deep and a 1 m soil profile with 14 levels. Grid stencils for the soil and the atmosphere are provided in Figures 9 and 10.

VI. One-Dimensional Sensitivity Tests

One-dimensional simulations were used to evaluate the behavior of the surface parameterizations. Soil moisture predictions from a layered soil were contrasted with moisture predictions from three slab schemes. Several experiments also provided guidance in selecting initial soil temperature and moisture profiles, a procedure necessitated by a lack of observed soil data. Finally more comparisons were run to determine the relative significance of soil albedo, initial moisture content and soil type. A few vegetation canopies were also examined to ascertain the reasonableness of their behavior.

A. Soil Slab vs. Layered Soil

It is common practice in meteorological modelling to predict the ground surface temperature using approximate methods which only depend upon the surface properties. However, when strong diurnal forcing is simulated, the best predictions result when the influence of the deep soil temperature is taken into account (Deardorff,1978). Most numerical models predict surface moisture using approximate techniques analogous to those used for the surface temperature, although some ignore moisture (Klemp and Lilly, 1978; Anthes and Warner, 1978).

Three schemes were examined which predicted surface soil moisture by treating the ground as a homogeneous slab. Each scheme used a form of equation I.1, where the weighting factor (δ) was defined as either a constant (i.e. 0.05) or

a ratio of the soil moisture in a layer to a saturation value (layer depths of 2 cm and 10 cm were assumed). For convenience these three runs are referred to as CONSTANT, SURFACE and DEEP, respectively. A fourteen level layered soil (LAYERED) served as the control. All runs parameterized a sandy soil with identical initial conditions. The sand moisture content was initially assumed to be 0.07 cm^3/cm^3. Details of the four simulations are given in Figure 11.

Figures 12 through 15 highlight the differences between these four runs. CONSTANT and SURFACE quickly dried out the soil. This promoted higher soil surface temperatures and more intense sensible heat fluxes. DEEP responded least to surface evaporation. The corresponding surface temperature and surface specific humidity lagged the control by about two hours, although both predictions improved markedly during the early afternoon.

Within one or two hours prior to sunset an inversion formed at low levels in the atmosphere, capping the region of turbulent transfer. Surface evaporation continued to export moisture to the atmosphere, where it accumulated in the lowest two hundred meters, thereby reversing the moisture flux divergence which prevailed during most of the afternoon. This is evidenced by a second maximum in the surface specific humidity, principally between 1700 and 1800 LST (Figure 13). A similar increase occurred in the atmospheric specific humidity near the ground (not shown). Note that the amplitude of the peak in specific humidity is correlated with the

Name of Run	δ	Initial χ	χ_s	No. of Levels
CONSTANT	.05	–	–	1
SURFACE	χ/χ_s	.14	.78	1
DEEP	χ/χ_s	.70	3.95	1
LAYERED	–	.07	–	14

Assumed surface moisture content initially .07 cm^3/cm^3

Atmospheric sounding used July 17,1973

Figure 11. Data used to simulate slab and multi-leveled soils. χ is soil moisture as a depth of water (cm) and χ_s is the saturated soil moisture. The three slab parameterizations for soil moisture utilize equation I.1 . In SURFACE and DEEP χ is depleted by subtracting the atmospheric turbulent moisture flux at each time step.

Figure 12. Predicted soil surface temperatures (^{o}C) as a function of local time for three slab prediction schemes and a multi-layered soil. LST is local sun time.

SURFACE TEMPERATURE

HOUR (LST)
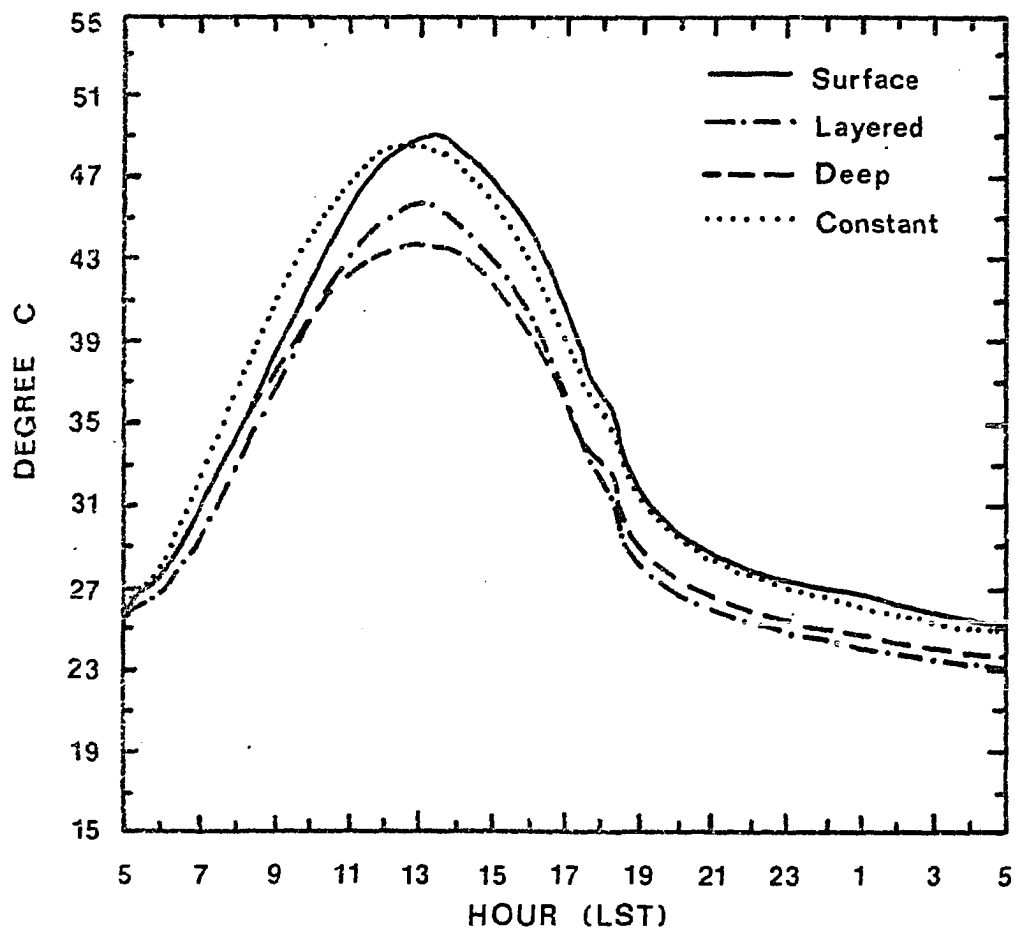
Figure 13. Predicted surface specific humidity (g/kg) as a func-
tion of local time for three slab prediction schemes
and a multi-layered soil.

SURFACE SPECIFIC HUMIDITY
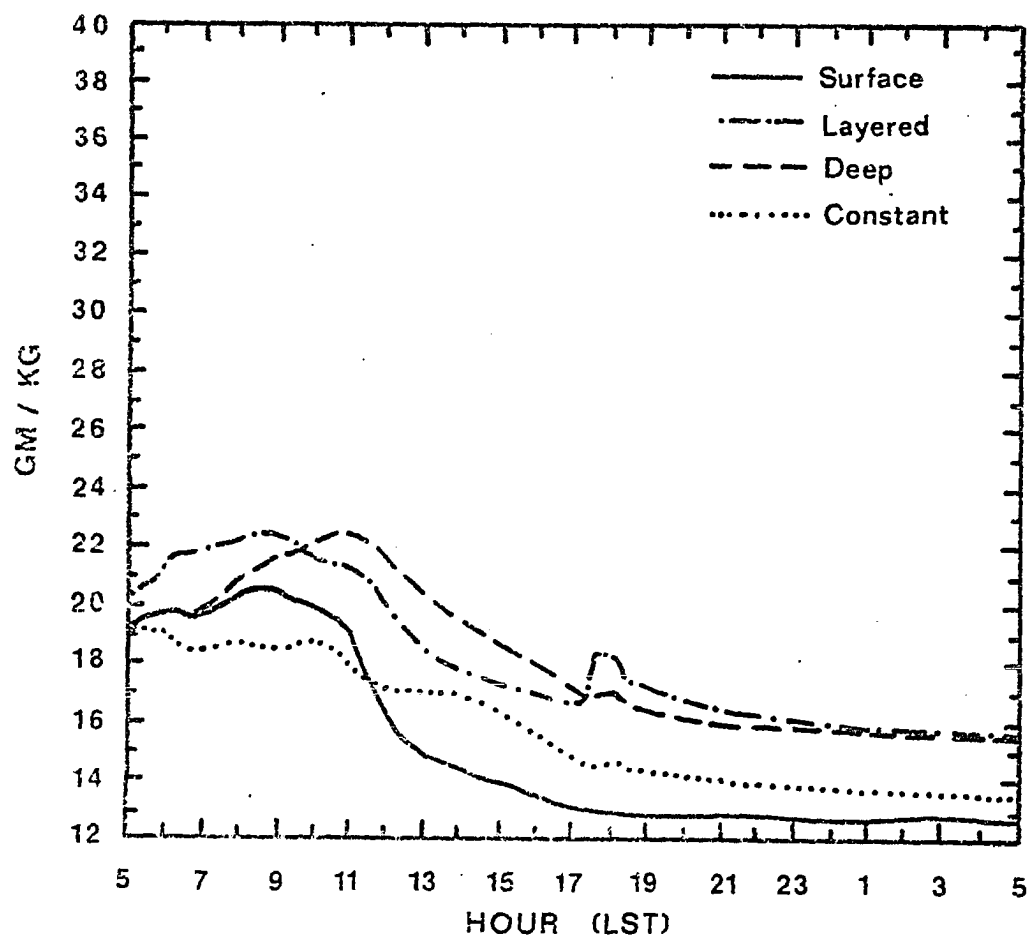
Figure 14. Predicted sensible heat flux density (watts/m^2) at the

surface of the ground as a function of local time for

three slab prediction schemes and a multi-layered soil.

Fluxes directed toward the atmosphere are negative.

SENSIBLE HEAT FLUX
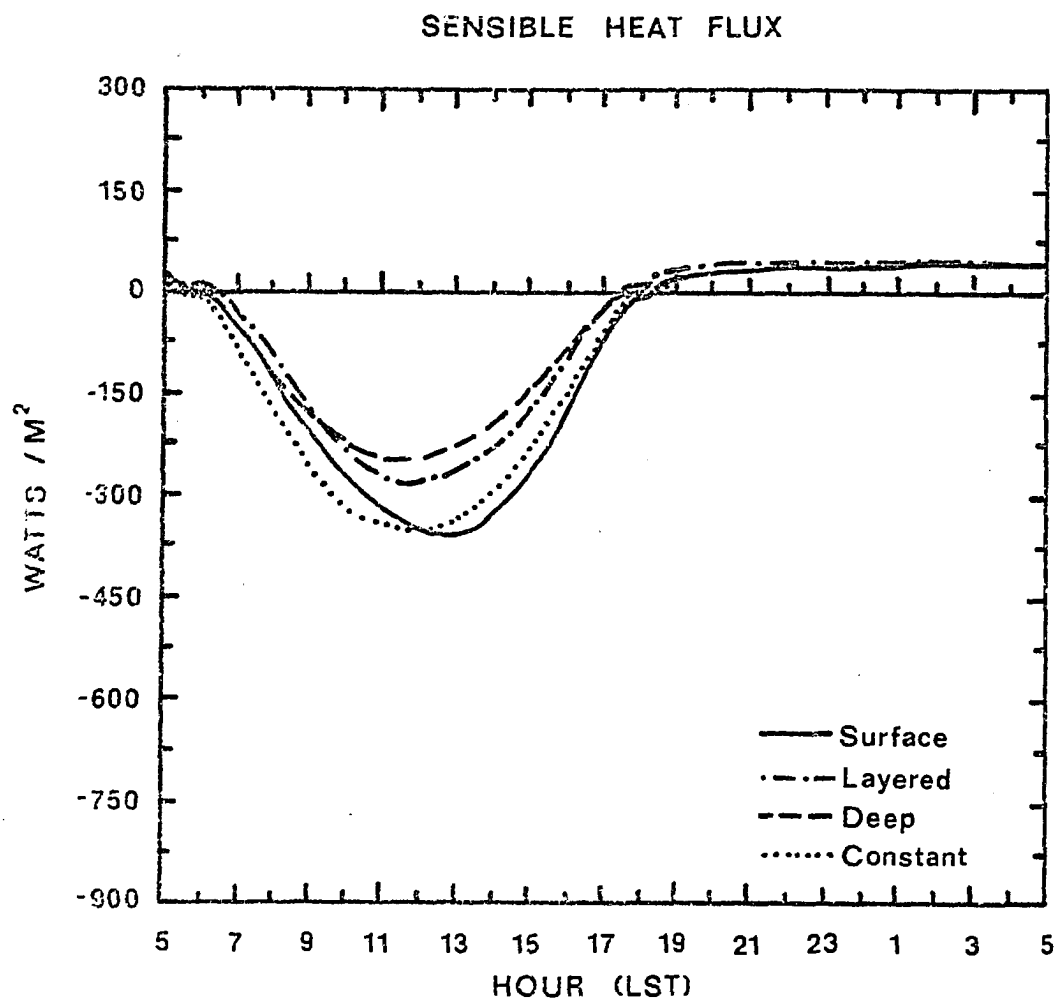
Figure 15. Predicted latent heat flux density (watts/m^2) at the surface of the ground as a function of local time for three slab prediction schemes and a multi-layered soil. Fluxes directed toward the atmosphere are negative.

LATENT HEAT FLUX
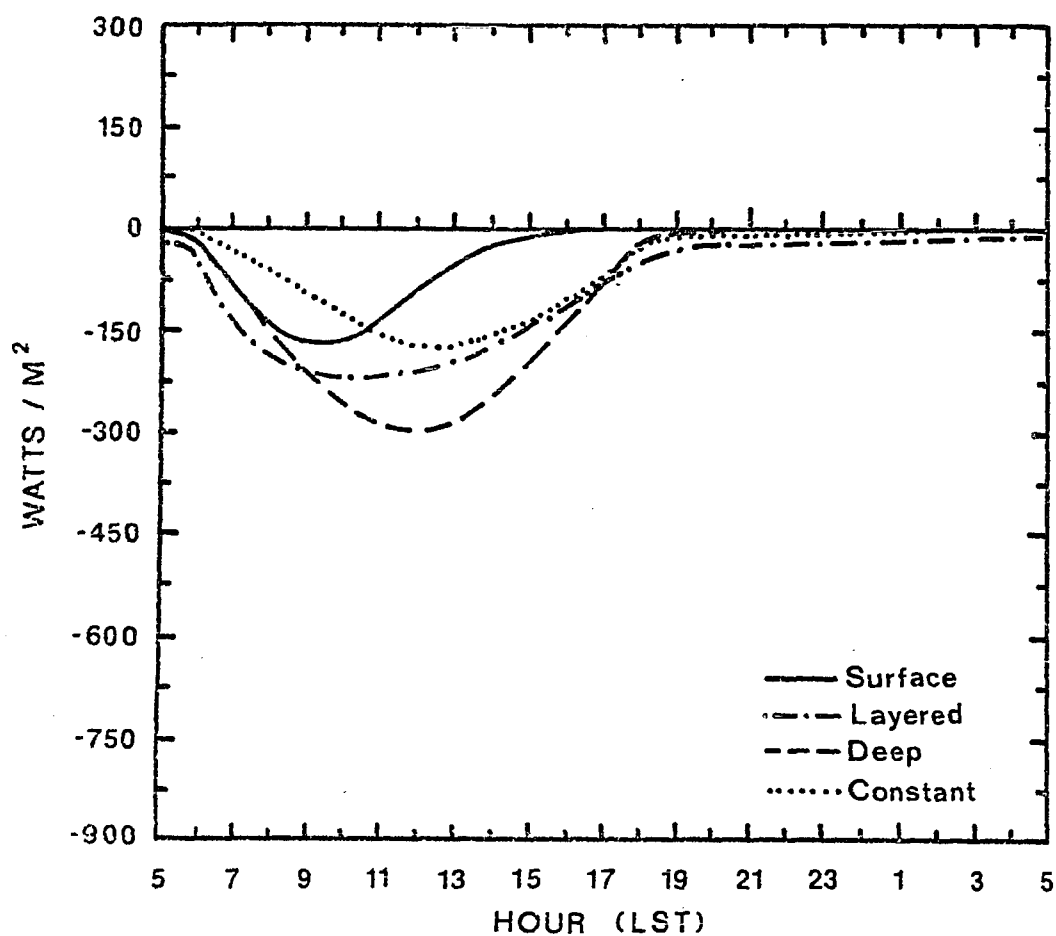
intensity of the latent heat flux (Figure 15). Geiger (1965) cited observational support for this phenomenon.

It is significant that the latent heat flux peaks about two hours prior to the sensible heat flux in the control. This reflects a limitation imposed by the surface relative humidity in equation IV.B.8. Recall that the surface specific humidity (q_G) is the <u>product</u> of the surface saturation specific humidity (q_S) and the surface relative humidity (h). When the surface relative humidity is high, then q_G varies in phase with q_S. Since q_S is a function of the soil surface temperature, it increases as the soil warms. Thus, q_G behaves in a similar manner (Figure 16). However, a low value of h (< .30) masks the effect of q_S, actually decreasing q_G prior to the time of maximum soil heating (Figure 17). SURFACE was the only slab scheme which approximated this effect when the soil was dry. However, q_G peaked and waned earlier than in the control, steadily decreasing for the duration of the simulation. This was due to the rapid decrease in the weighting factor, which dropped from 0.177 at 0500 LST to 0.029 at noon and 0.0013 by 1700 LST.

Apparently predicting soil moisture from a soil slab requires a careful description of the weighting factor employed. Admittedly the dry sand used here provided a harsher test of the schemes than may often be encountered. Agreement is likely to be much better for moist soils. This is especially true of DEEP, whose temporal variation is much

Figure 16. Diurnal variation of specific humidity (dashed line)

and relative humidity (solid line) at the surface of

sand for a layered soil profile. The initial mois-

ture content is 0.12 cm^3/cm^3.
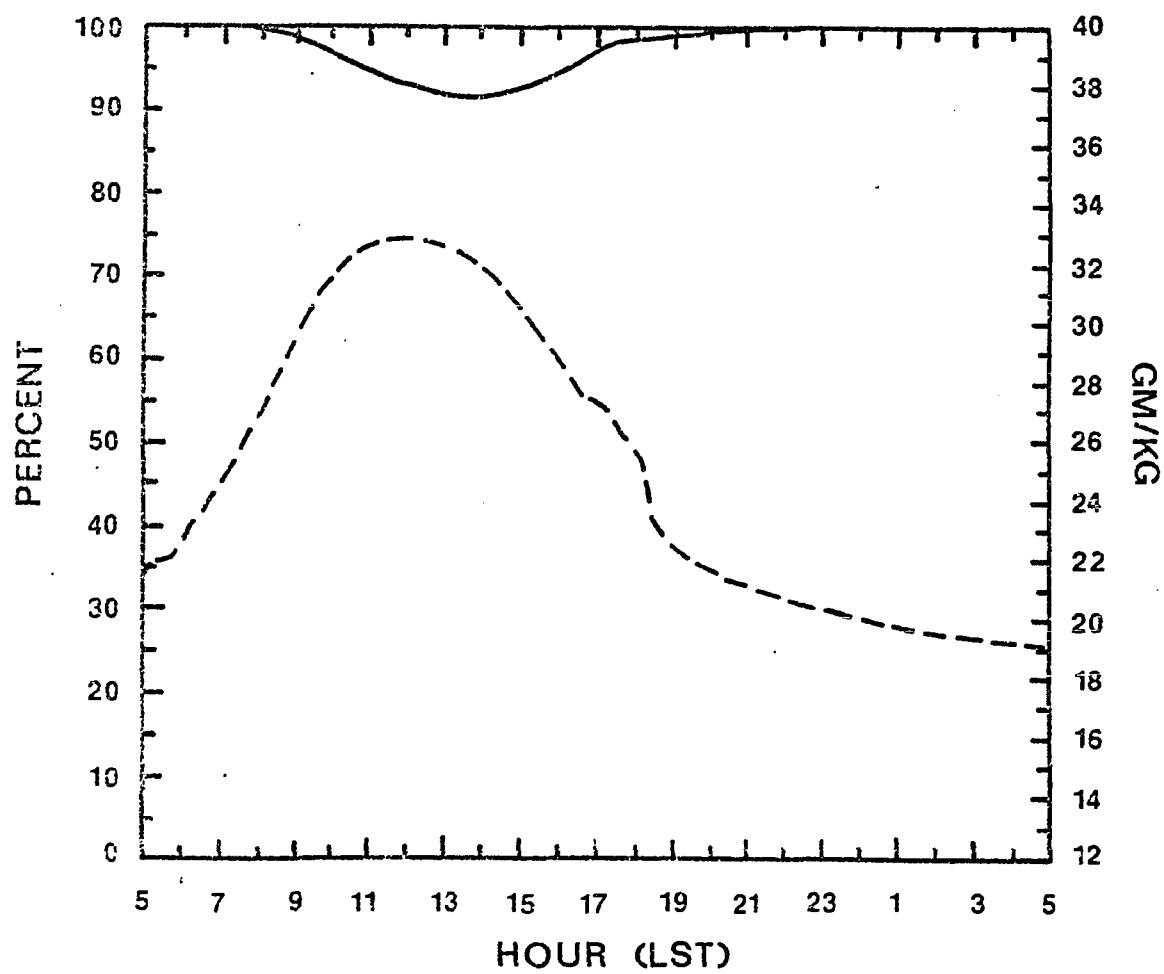
Figure 17. Same as Figure 16, except that the initial moisture content is 0.07 cm^3/cm^3. The abrupt rise in the specific humidity (dashed line) accompanied the development of a surface inversion around sunset.
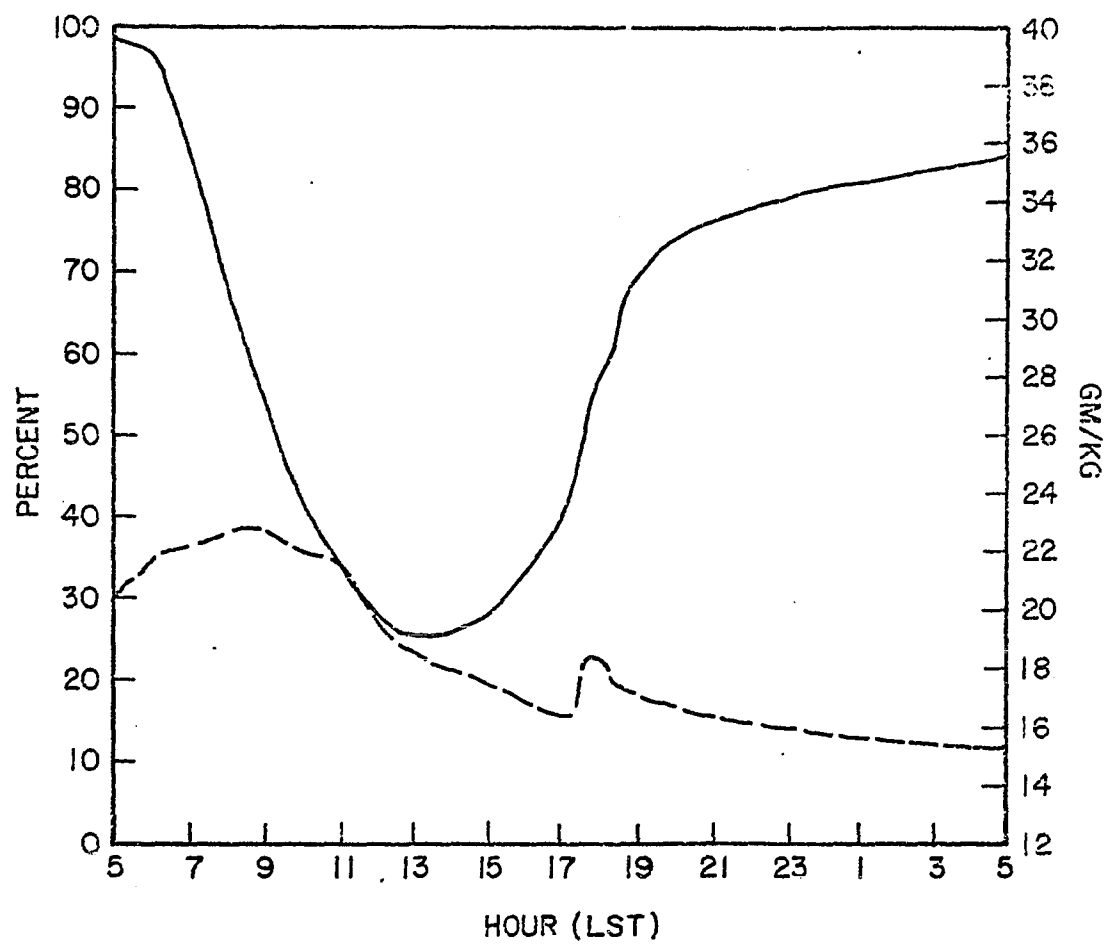
like that of moist soils tested with the layered model. Un-
like any of the slab schemes presented here, Deardorff (1978)
included a restoring effect of deep soil moisture to his
weighting factor. This is a reasonable adjustment, but
since his technique was not evaluated it is not known to
what degree it may be effective.

B. Influence of the Initial Soil Temperature and
    Moisture Profile

Sampled soil data are commonly lacking, which makes

initialization difficult. Garrett (1978) overcame this

problem by using soil moisture and temperature profiles

sampled at O'Neill, Nebraska, (Lettau and Davidson, 1957).

He applied them to the southeastern United States and

assumed that the soil was horizontally homogeneous. This

method does not extend itself satisfactorily to spatial

variability in soils. Therefore, soil temperature and

moisture profiles must be specified in some way for each

class of soil represented.

It was necessary to establish how crucial the initial

vertical profiles of temperature and moisture were within

the soil. This was accomplished via seven simulations (Fig-

ure 18a) in which either the soil temperature or the soil

moisture was varied from a base state. Data for the base

state was secured from a morning observation from Lettau and

Davidson (1957) and is given in Figure 18b. The variations

included a linear increase with depth, a linear decrease

with depth and zero gradient. The temperature gradient was

$\pm$ 4 K/m, while the moisture gradients were 0.20 $cm^3/cm^3/m$

and -0.07 $cm^3/cm^3/m$. All runs commenced at sunrise and

integrated for twelve hours. The initial surface moisture

content and surface temperature were identical in each

simulation. Table IV summarizes the results.

For a given moisture content and type of soil, the

temperature profile which developed was essentially

Experiment	$\dfrac{\partial T_s}{\partial z}$	$\dfrac{\partial \eta}{\partial z}$
1	O'Neill, Neb.	O'Neill, Neb.
2	0	O'Neill, Neb.
3	4.0 K/m	O'Neill, Neb.
4	−4.0 K/m	O'Neill, Neb.
5	O'Neill, Neb.	0
6	O'Neill, Neb.	0.20 cm^3/cm^3
7	O'Neill, Neb.	−0.07 cm^3/cm^3

Initial surface moisture content   0.12 cm^3/cm^3

Atmospheric sounding used   July, 17,1973

Figure 18a. Tests to determine the influence of the initial temperature and moisture profiles in the soil. O'Neill, Neb. is the base state data and it was obtained from Lettau and Davidson (1957). It is given in part b.

z (cm)	T_s (K)	η (cm^3/cm^3)
0.0	301.03	0.120
0.5	301.17	0.120
1.5	301.54	0.117
3.0	301.98	0.109
5.0	302.98	0.093
8.0	302.81	0.086
12.0	302.70	0.083
18.0	304.99	0.083
26.0	305.03	0.083
36.0	305.28	0.083
48.0	305.59	0.083
62.0	304.33	0.083
79.0	303.31	0.083
100.0	303.08	0.083

Figure 18b. Base state soil profiles of temperature and moisture used in the experiments listed in Figure 18a. z is depth.

	Variable Temperature	Variable Moisture
ΔT_G ($^{\circ}$C)	0.3	3.7
Δq_G (G/KG)	0.1	4.1
ΔLE (W/M^2)	5.0	110.0
ΔH (W/M^2)	5.0	75.0

Table IV. Effect of the initial soil temperature and mois-
ture profiles. The first column refers to a set of ex-
periments in which the temperature profile was varied
from a base state while the moisture profile was un-
changed. The second column refers to another set of
experiments where the moisture profile varied while the
temperature profile was fixed. The numbers represent
the maximum range for each set of experiments for the
surface temperature (T_G), surface specific humidity
(q_G), latent heat flux (LE) and sensible heat flux (H).

independent of the initialization chosen. This meant that solar forcing, which was quite strong, was clearly the dominant influence upon soil temperature. The choice of initialization of the soil temperature profile may be more critical, however, should the integration commence at night or should the sky be cloudy.

Varying the initial profile of soil moisture content had a much greater impact than varying the soil temperature profile. Thus, without data, it is difficult to justify a preference for one moisture profile over another. For this reason, no gradient in soil moisture content was assumed in the runs which follow. However, the soil temperature was initialized with the O'Neill, Nebraska, data (Table II).

Estimating the surface moisture content was equally challenging. Idso et al. (1975) suggested that the thermal inertia concept could adequately estimate soil moisture. Their data indicated that thermal inertia is most appropriate to the uppermost 2 - 4 cm of the soil, where the relationship between moisture content and the amplitude of the diurnal temperature wave is linear. But at the surface the relationship is highly non-linear when the soil is dry. This was presumably the situation on July 17, 1973, in south Florida. The wet season was still in progress, but intense solar heating exerted a strong evaporative demand on the soil, likely drying much of the soil surface significantly (Gannon, personal communication).

South Florida is chiefly characterized by four soil

textures--sand, sandy loam, sandy clay and peat. The soils vary widely in drainage and water retention characteristics. In general the drainage is greatest and the water retention least in coarse-grained soils (i.e. sand). Drainage decreases as the texture becomes finer while water retention increases. However, the available water content (i.e. freely available to plants) decreases when the clay fraction gets large (Salter and Williams, 1965; Petersen et al., 1968; Jadhav et al., 1977).

Sand in south Florida is usually well-drained (General Soil Map of Florida, Conservation Services of the U. S. Department of Agriculture, Gainesville, Florida). It was assigned a moisture content of 0.07 cm^3/cm^3, which is slightly above the permanent wilting percentage (Table I). Since water retention is higher in sandy loam and sandy clay, they were assumed to be wetter. Each was assigned a surface moisture tension of 20 meters, which corresponds to volumetric moisture contents of 0.17 cm^3/cm^3 and 0.27 cm^3/cm^3 for the loam and the clay, respectively. Both are mid-range levels of available moisture.

Peat soil was initialized at two-thirds of saturation (0.58 cm^3/cm^3), while marshland was treated as saturated peat. This was preferable to considering marsh as water because it permitted a diurnal change in the surface temperature which the model would have otherwise precluded.

C. Effect of Surface Albedo and Initial Moisture

Sand and marsh were used to test surface albedo. They were representative of dry and wet surfaces. Two cases were considered for each soil: a fixed albedo of 0.20 was used for one case while the albedo was free to vary as a function of the surface moisture content in the other (III.B.10). Energy fluxes depicted in Figures 19 and 20 indicate changes in flux strength, but no significant modification in the basic shape of the plots (i.e. the temporal response). The net effect of a constant albedo was to reduce the surface temperature of the marsh by about 1°C while it increased the surface temperature of the sand by 2.5°C.

The sensitivity of the model to initial soil moisture content was evaluated for five types of soils (sand, sandy loam, sandy clay, peat and marsh). Representative time series plots of energy fluxes are presented for sand in Figure 21 . The moisture content of the wetter sand was 0.12 cm^3/cm^3 whereas it was 0.07 cm^3/cm^3 for the dry sand. In each instance the albedo was fixed at 0.20 and the soil moisture profile was assumed to be vertically homogeneous.

When the soil moisture supply was plentiful, a substantial fraction of the available surface energy was used for evaporation. This meant that less energy was available to warm the soil, which resulted in a cooler soil and a weaker sensible heat flux. The lower surface temperature in turn produced a smaller surface temperature gradient, which resulted in a diminished soil heat flux even though the

Figure 19. Effect of albedo on surface heat fluxes for marsh soil. Initial moisture content is 0.86 cm^3/cm^3. a. Constant albedo (0.20) b. Albedo is variable. It is related to soil moisture through III.B.10.2 . Heat fluxes directed toward the atmosphere are negative.
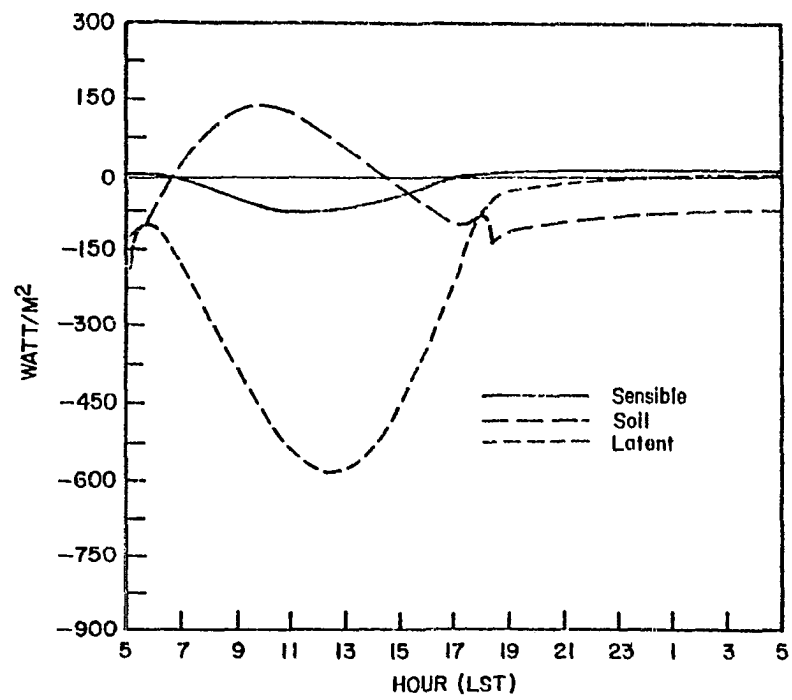
a.
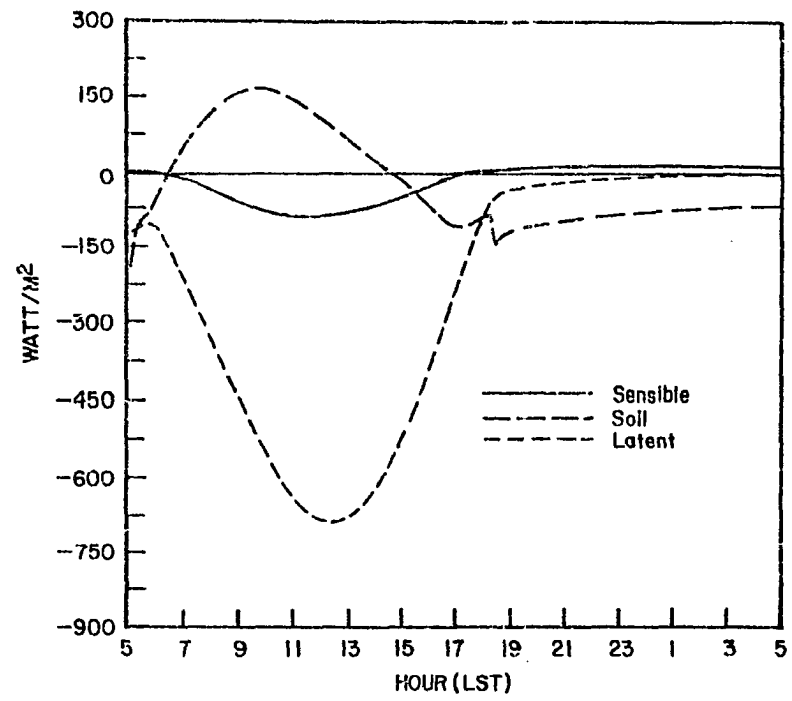
b.

Figure 20. Same as Figure 19, except the soil type is sand and the initial moisture content is 0.07 cm^3/cm^3.
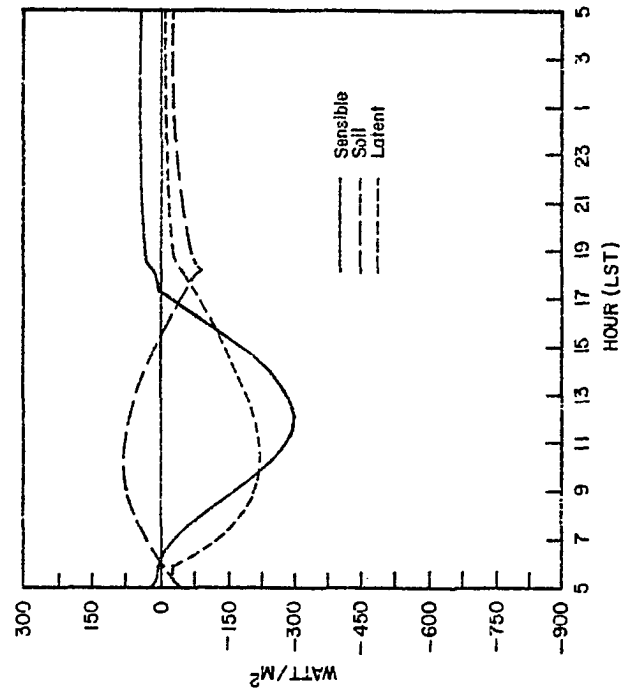
b.
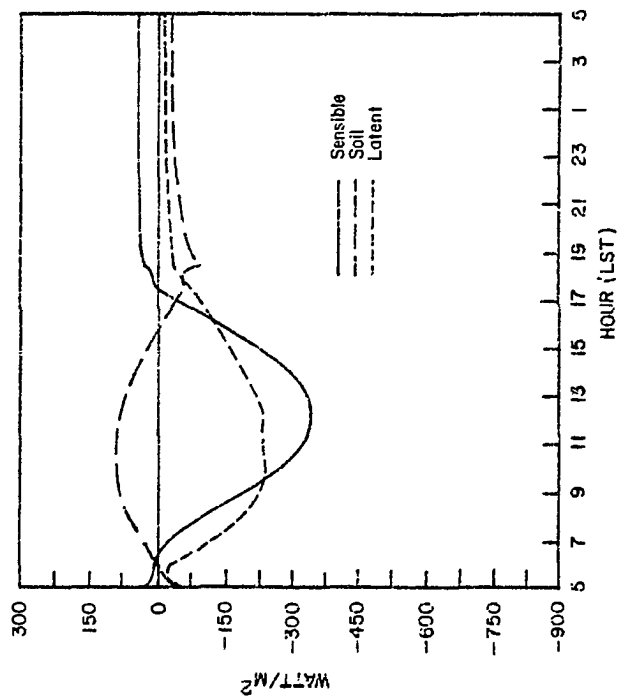
a.

Figure 21. Effect of initial soil moisture for sand with a constant
albedo (0.20). a. Initial moisture content is 0.07
cm^3/cm^3 . b. Initial moisture content is 0.12 cm^3/cm^3.
Heat fluxes directed toward the atmosphere are negative.
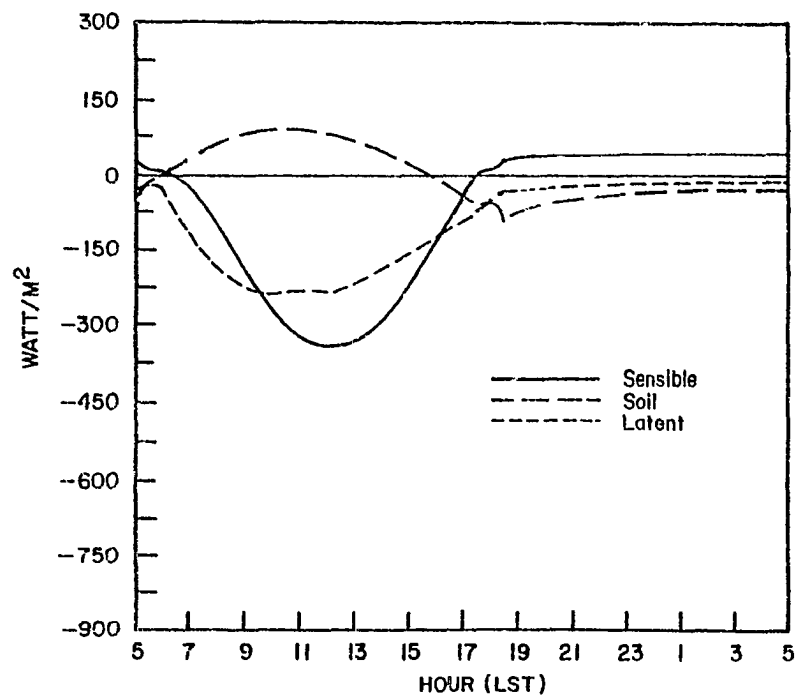
a.
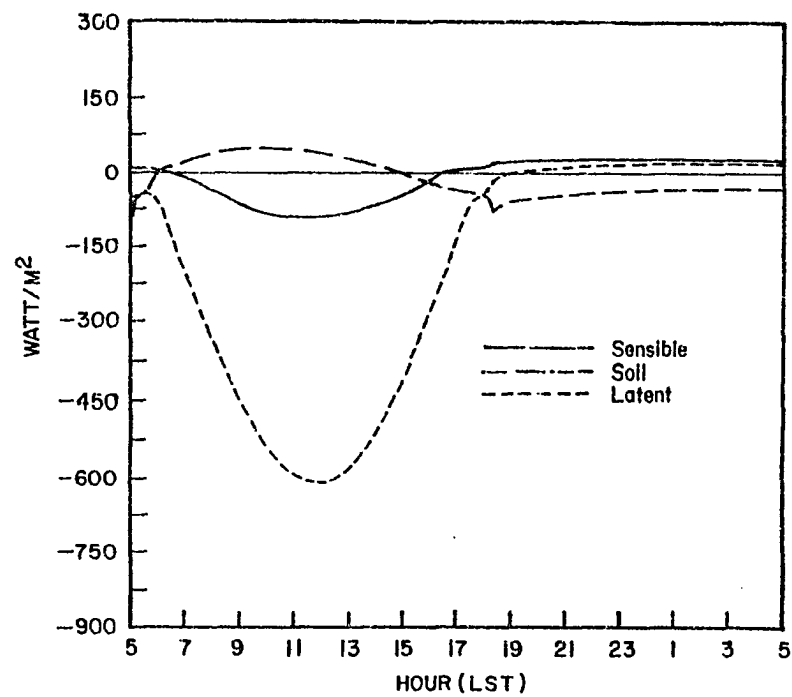
b.

thermal conductivities were much larger for the moist sand (Figure 2).

In the dry sand, the surface moisture was quickly depleted. This caused a sharp drop in the surface relative humidity and the surface specific humidity. The attendant reduction in the latent heat flux was accompanied by a stronger sensible heat flux which promoted deeper turbulent transfer in the atmosphere.

Energy diverted from evaporation was principally used to warm the soil. For example, dry sand gained three times the heat of moist sand. As a result, the soil heat flux doubled and the sensible heat flux was nearly quadrupled. Note that the sensible heat flux was approximately symmetric about local noon for both sands. The latent heat flux was similarly symmetric only for the wet sand (Figure 21b). In the latter case, this reiterated the influence of the surface relative humidity.

D.   Influence of Type of Soil

Five different soils (peat is treated as a soil for the purpose of this discussion) were tested. Figures 22 through 25 indicate that soil behavior was predominantly determined by moisture content. As an example consider the sensible heat flux (Figure 24). Most of the soils evaporated moisture at nearly the potential rate (i.e. surface relative humidity was close to 100%). Hence, their behavior was similar. However, sand being much drier, resulted in a substantially more vigorous sensible heat flux than any of the others. Van Bavel and Hillel (1976) obtained a similar relationship between soil wetness and the intensity of computed sensible and latent heat fluxes.

Since the turbulent mixing in the atmosphere is driven by the thermal forcing near the ground, it is not surprising that maximum boundary layer depths after 24 hours of simulation for peat, marsh, sandy clay and sandy loam were grouped, ranging from 1304 meters to 1499 meters. On the other hand, the boundary layer over sand grew to a depth of 2096 meters, indicative of the stronger sensible heat fluxes.

There was a somewhat wider disparity between latent heat fluxes. Marsh and peat behaved similarly as did sandy clay and sandy loam. This is a direct reflection of the control exerted by the surface specific humidity. The temperature range amongst these four soils never exceeded 3°C. Hence, the differentiation in q_G must generally be due to the surface relative humidities. Both peat and marsh

Figure 22. Predicted soil surface temperature (^{O}C) as a function

of soil type. Notice the smaller diurnal range for

the wettest soils (marsh and peat).

SOIL TEMPERATURE
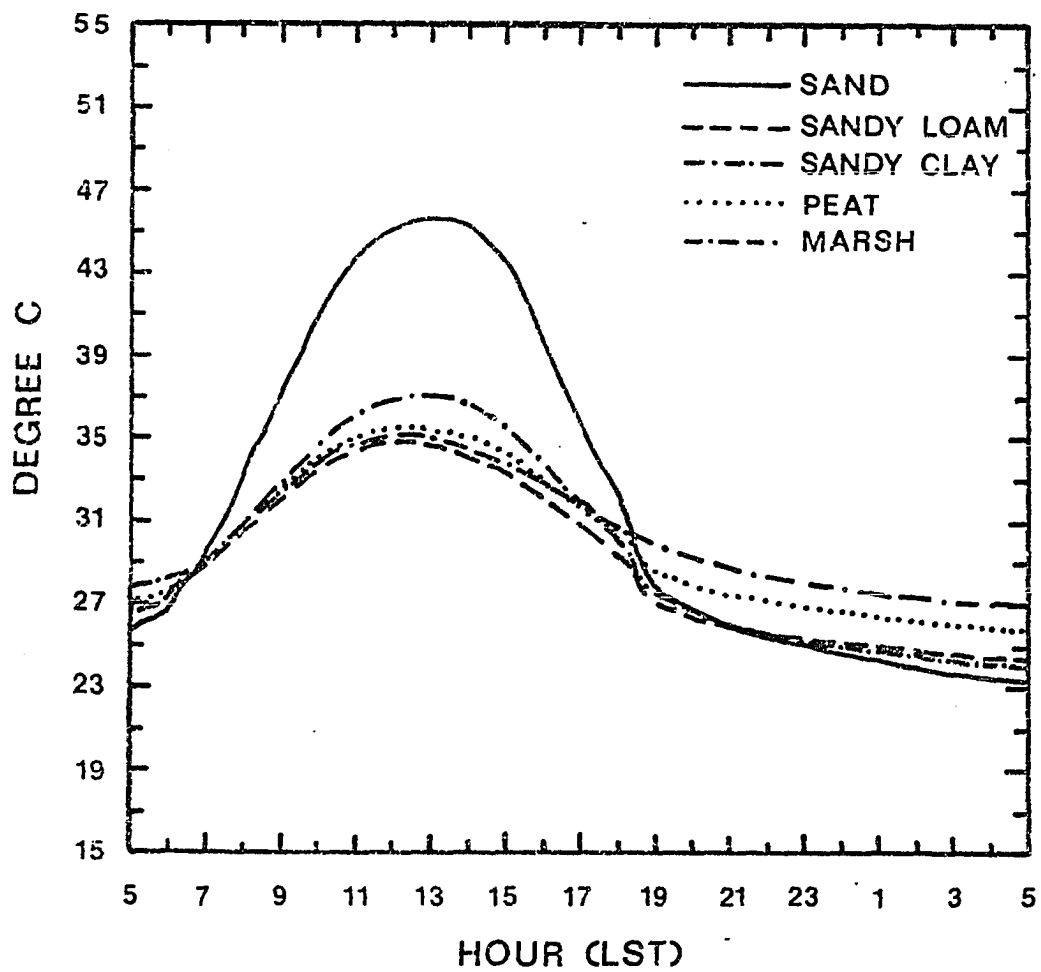
Figure 23. Predicted soil surface specific humidity (g/kg) as a function of soil type.

SURFACE SPECIFIC HUMIDITY
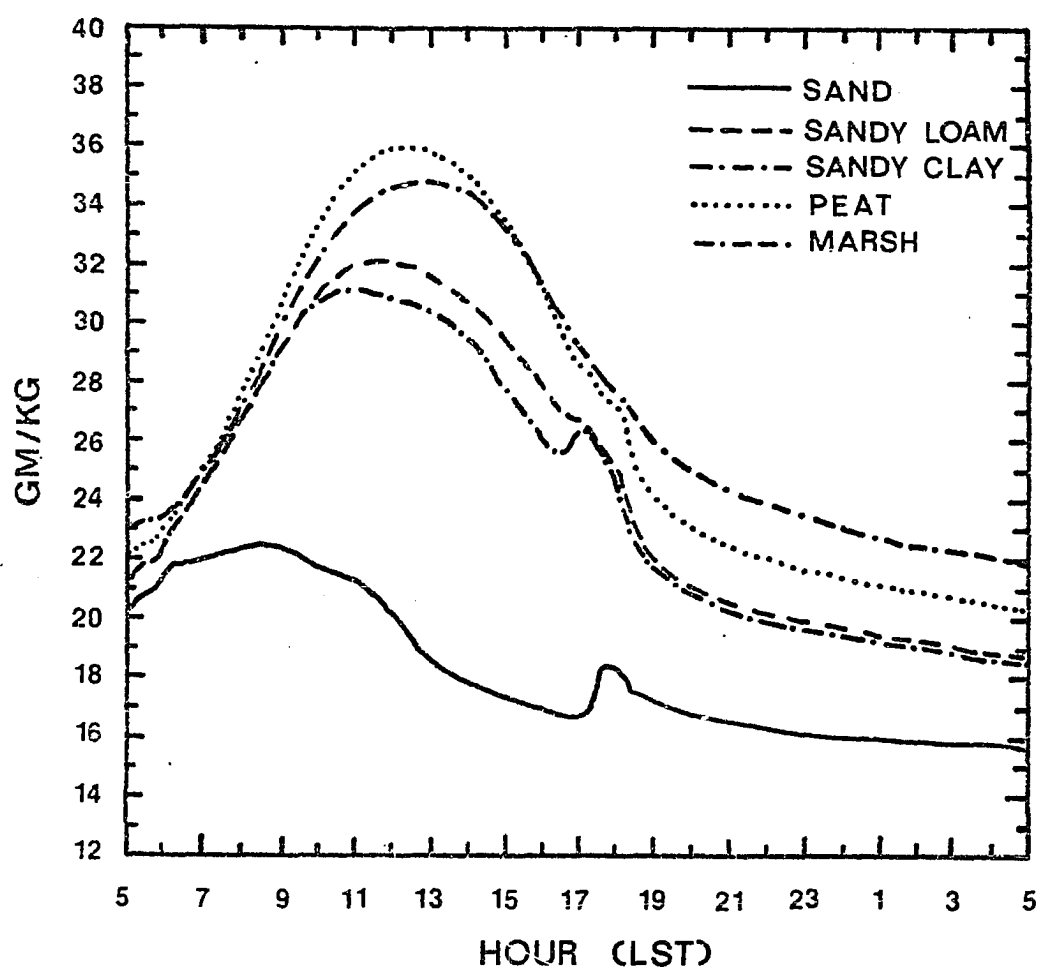
Figure 24. Predicted surface sensible heat flux density (watts/m^2) as a function of soil type. Fluxes directed toward the atmosphere are negative.

SENSIBLE HEAT FLUX

Legend:
- SAND (solid line)
- SANDY LOAM (dashed line)
- SANDY CLAY (dash-dot line)
- PEAT (dotted line)
- MARSH (dash-dot-dot line)

X-axis: HOUR (LST), ranging from 5 to 5
Y-axis: WATT/M², ranging from -900 to 300
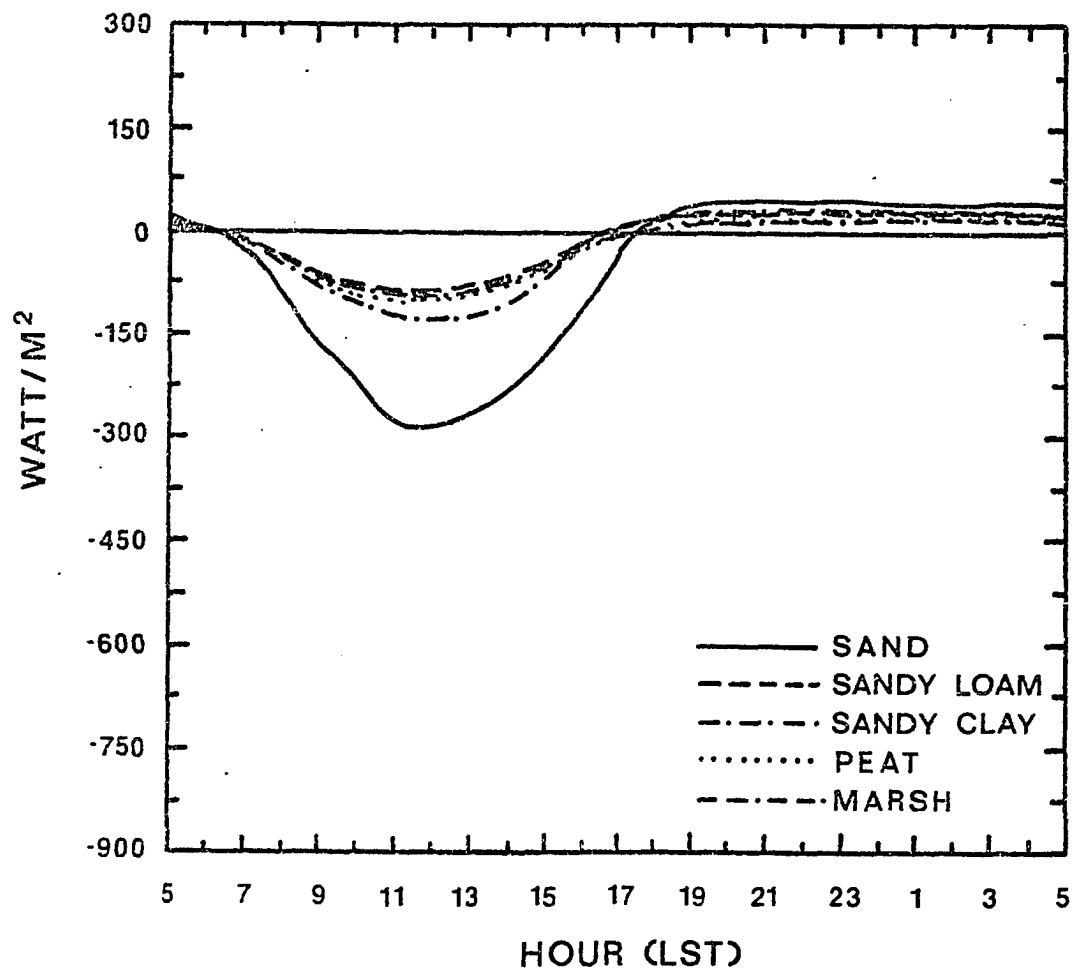
Figure 25. Same as Figure 24, except for the surface latent heat flux density (watts/m^2).

LATENT HEAT FLUX

Legend:
- Sand ——————
- Peat — — — —
- Sandy loam — — — —
- Sandy clay – – – –
- Marsh ● ● ● ● ●

Y-axis: WATT/M² (300, 150, 0, −150, −300, −450, −600, −750, −900)

X-axis: HOUR (LST) (5, 7, 9, 11, 13, 15, 17, 19, 21, 23, 1, 3, 5)
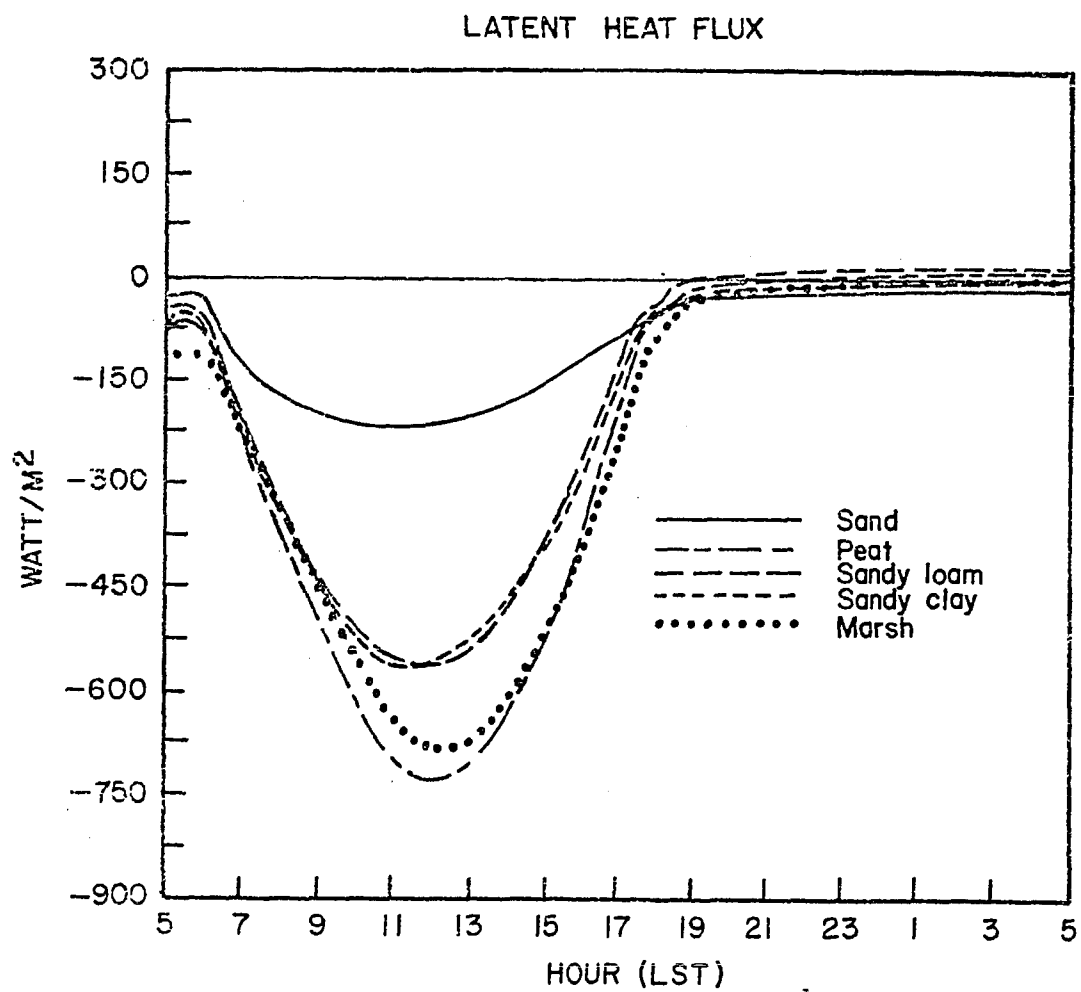
evaporated moisture very near the potential rate at all times. But the afternoon relative humidity in the sandy loam soil dropped to 90% and it fell to 75% for sandy clay. Sand was markedly drier than the other soils, registering a mid-afternoon relative humidity of only 28%.

Some variability can be attributed to the different soils themselves. For instance, sandy clay warmed about 2°C more than sandy loam, yet they were both initialized with the same soil moisture suction. But the soil albedo was determined as a function of the fractional wetness of the soil (equations III.B.10) so that the albedos were never equal. At 1315 LST the surface albedo for the sandy clay was 18.2%, while it was 25.3% for the loam. Although the soil thermal conductivities and the moisture release characteristics were different for each soil, it appears that the additional net radiation received by the sandy clay (60 watts/m^2 at 1300 LST) was the principal reason for the greater warming.

Nevertheless, it was the soil wetness which regulated the behavior of each soil tested. Conceivably a single soil texture could be successfully employed with little likely error if the soil moisture and the albedo are mapped in lieu of soil variability.

E.   Test of Several Foliage Canopies

Two different canopies were tested in conjunction with the five soils defined above.   Physical variables characterizing grass and forest canopies are listed in Table III. The emissivity for grass represents an average value while the tree emissivity favors conifers (Oke, 1978).   Foliage albedos were selected in the same way.   The resistance coefficients for leaf transpiration were taken from Fetcher (1976).

Figure 26 shows the diurnal variation of predicted temperature for some grass and forest canopies (two cases each) which were used in the three-dimensional experiments. Solid lines represent leaf temperature whereas the dotted lines apply to the air within the single-level canopy.   The dashed lines refer to the surface of the ground.

During the day the foliage was 3 - 6°C warmer than the air at noon.   This is well within reason, since leaf temperatures are known to commonly exceed air temperatures by up to 10°C (Geiger, 1965), (Oke, 1978).   At night foliage typically cooled one to two degrees Celsius below the air temperature (within 0.4°C for the dry sand), in good agreement with typical observed data (Geiger, 1965).   This resulted in a sensible heat gain by the foliage.

Two different effects determined the daytime surface temperature beneath a vegetation canopy.   The first is cooling due to a reduction in the incoming solar flux by shading.   The surface temperatures of the dry sand in

Figure 26. Diurnal variation of predicted foliage temperature
(solid line), canopy air temperature (short dashed
line) and ground temperature (long dashed line) in
^{o}C. a. grass atop peat soil (σ_f = 0.85) b. grass
atop sandy soil (σ_f = 0.75) c. trees atop sandy
clay (σ_f = 0.90) d. trees atop sandy loam (σ_f =
0.90) These cases represent four of the soil and
plant combinations used in the three-dimensional
simulations. The abscissa is the local time in
hours.
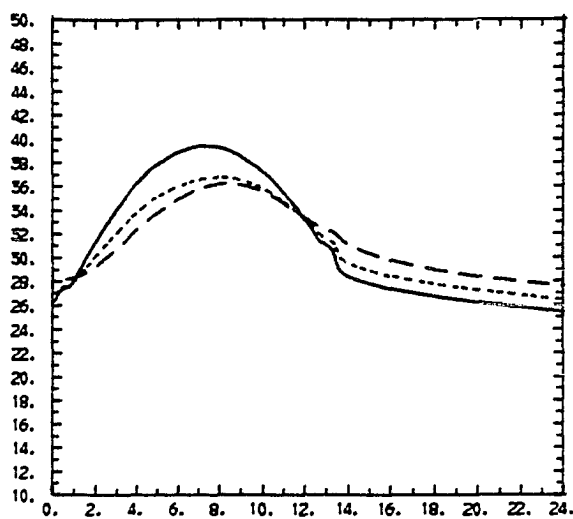
a.
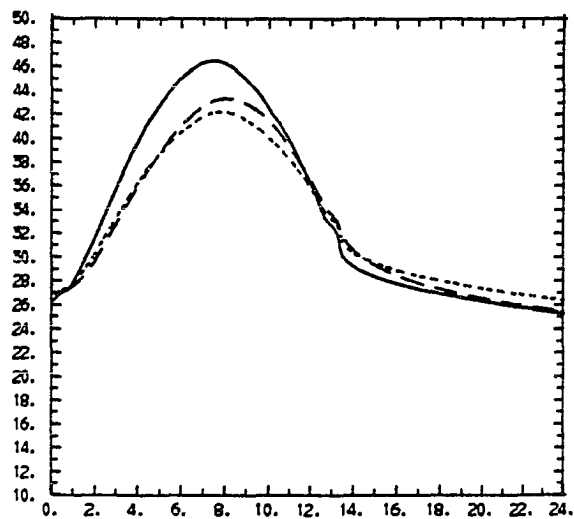
b.
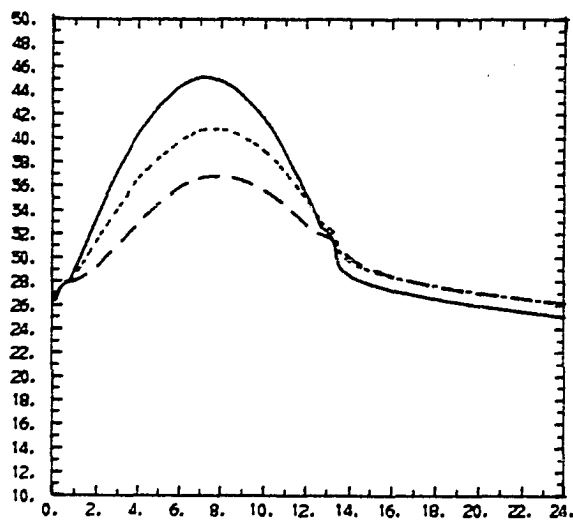
c.
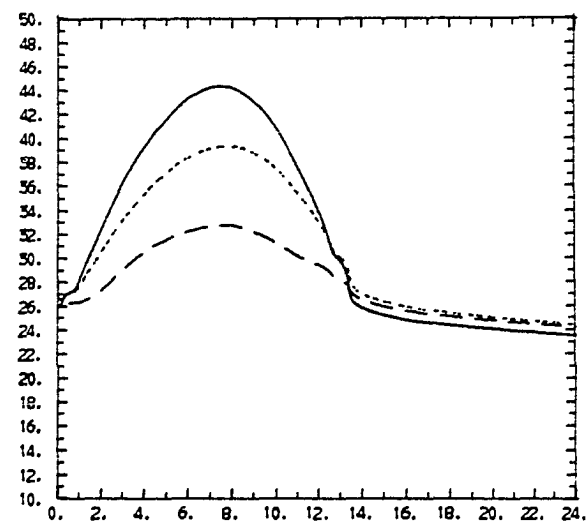
d.

Figure 26b and the sandy clay in Figure 26c illustrate this effect. Second, the relatively large aerodynamic roughness of the vegetation reduced the air speed near the ground. This, of course, reduced advection. The effect was greatest on the latent heat flux, which was primarily controlled by the moisture gradient near the surface. Lighter winds permitted low level moisture to accumulate, reducing the near-surface gradient. Reduced evaporation lowered the ground albedo (recall III.B.10) increasing the short wave flux density received at the surface. The diminished evaporation also diverted a larger fraction of the net radiation to warm the soil and increase the sensible heat flux. This process was most important for trees on sandy loam (Figure 26d) and for simulations of grass on all types of soil except sand.

The daytime ground temperature below a canopy was always lower than the air temperature at canopy level. This resulted in a stable stratification beneath the foliage. At night the stratification destabilized above all of the soils except sand, though the sensible heat fluxes were quite weak (in most cases less than 2.0 watts/m^2).

Specific humidities are shown in Figure 27. Solid, dotted and dashed lines refer to the foliage, canopy air and ground surface specific humidities, respectively. In each instance, the peak surface humidities are 2 - 6 g/kg larger than they were for bare soil. This results from the reduced surface evaporation.

Figure 27. Same as Figure 26, except that the plots are for foliage specific humidity (solid line), canopy air specific humidity (short dashed line) and ground specific humidity (long dashed line) in g/kg. The abscissa is the local time in hours.
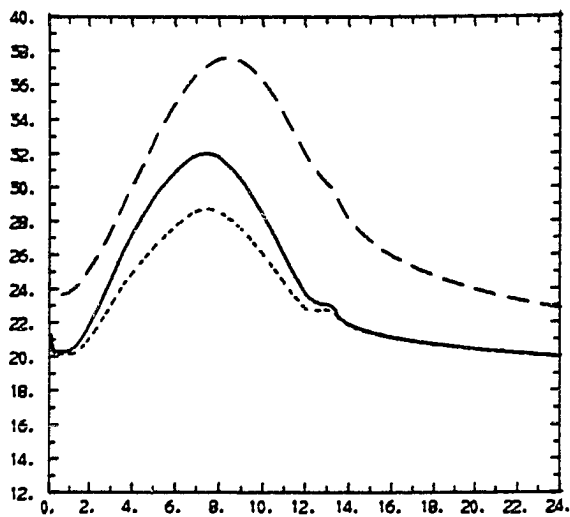
a.
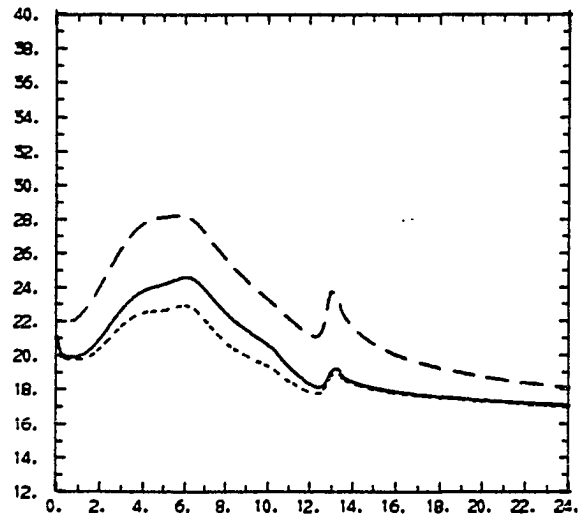
b.
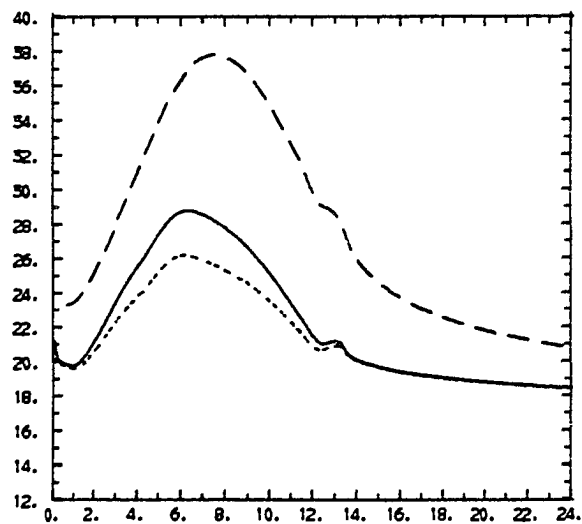
c.
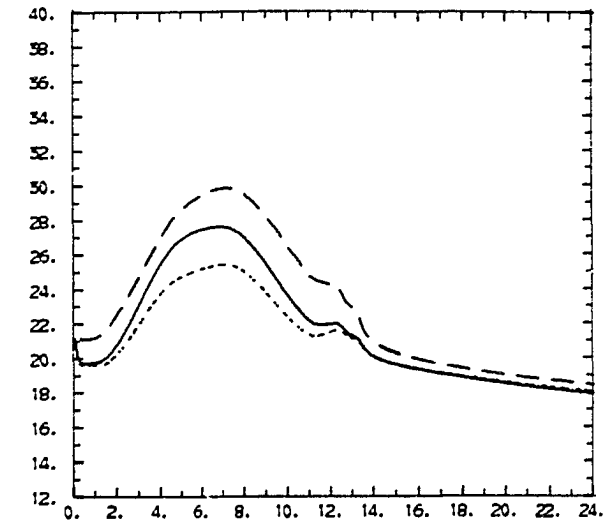
d.

Deardorff (1978) noted in his results that q_f (the foliage specific humidity) exceeded q_G in the early morning hours. He attributed this to the higher foliage temperature. This relationship is not evident in the experiments presented here because the ground was wetter and the stomatal resistance coefficients were larger than those of Deardorff.

Examples of <u>total</u> energy fluxes from two different canopies are plotted in Figure 28. The dashed line is the total latent heat flux and the dotted line is the total sensible heat flux. Transpiration from the foliage canopy is plotted with a solid line. Greater turbulent exchange above the forest increased the canopy wind by 20% over that for a grassland, resulting in a stronger sensible heat flux and a slightly larger latent heat flux. The larger Bowen ratio (sensible heat/latent heat) for the forest occurs because the resistance coefficient for transpiration is twice as large as the coefficient for grass. Also note that the total latent heat fluxes for vegetated land do not exceed the bare soil fluxes in Figure 25 (sand was an exception). This is really not unexpected since the bare soils evaporated moisture very near the potential rate. Drier soils would probably behave differently.

Predicted total fluxes of latent and sensible heat are given in Table V for eight different combinations of soils and canopies. The simulated time is 1215 LST. In most cases the Bowen ratio is nearly 0.50, which agrees with data reported for forests and grasslands (Black and McNaughton, 1971;Hicks et al., 1975). The larger Bowen ratios which

Figure 28. Comparison of energy fluxes from simulated vegetation.

Fluxes plotted are the total sensible heat, total latent

heat and the transpiration fluxes $(watts/m^2)$. Negative

fluxes are directed toward the atmosphere. a. grass

overlying peat soil (σ_f = 0.85) b. trees overlying

sandy clay soil (σ_f = 0.90) .
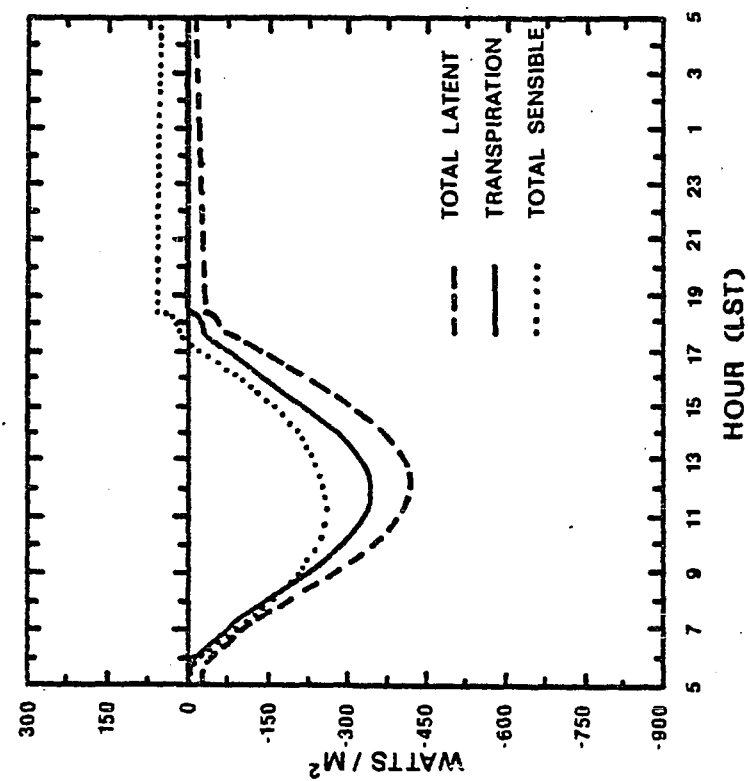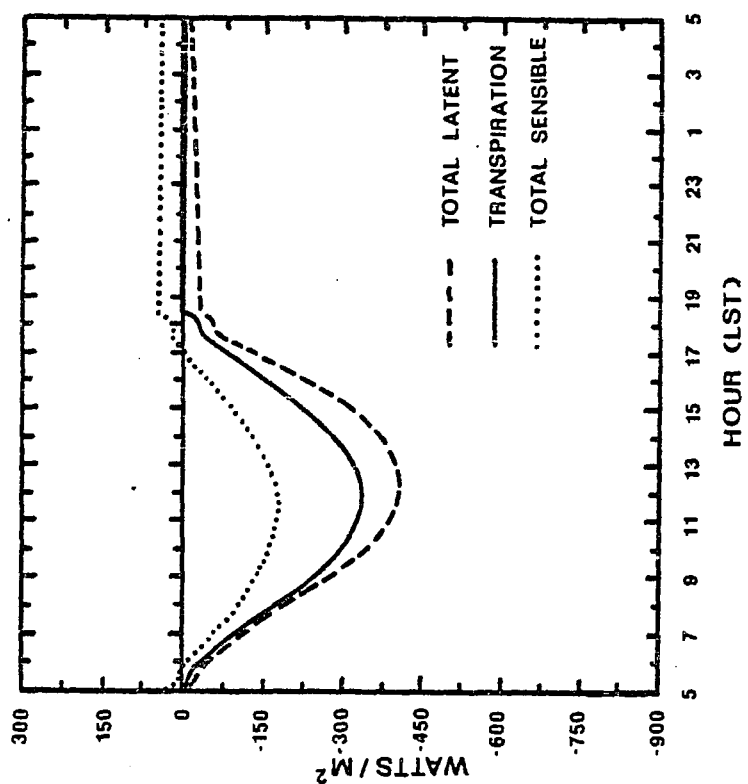
Soil Type	Canopy	σ_f	H_{TOTAL}	LE_{TOTAL}	Bowen Ratio
Sand	Trees	0.90	394	250	1.58
Sandy Loam	Trees	0.90	255	452	0.56
Marsh	Trees	0.98	261	509	0.51
Sandy Clay	Trees	0.90	277	424	0.65
Sand	Grass	0.75	251	230	1.09
Peat	Grass	0.85	154	428	0.36
Marsh	Grass	0.50	99	376	0.26
Sandy Clay	Grass	0.85	178	409	0.44

Table V . Total fluxes at 1215 LST for sensible heat and latent
heat for eight different combinations of soil and type
of canopy. Fluxes are in watts/m^2.

occur for sand reflect the increase in the stomatal resistance which occurs when the soil moisture is limited.

One of the difficulties presented by a lack of observed data for the vegetation is the choice of representative resistance coefficients. Reported values span a large range varying from 0.7 sec/cm for grasses (Monteith and Szeicz, 1962) to about 100 sec/cm for lodgepole pine (Fetcher, 1976).

Sensitivity tests revealed that a small reduction in the resistance coefficients from 8 to 4 sec/cm for trees increased the percentage of the total moisture flux due to transpiration from 79% to 90% at 1315 LST. A reduction from 4 to 2 sec/cm for grasses had a lesser effect (6% change). The total latent and sensible heat fluxes for both grasses and trees changed by about 13%. Hence the atmosphere was largely unaffected by the reapportioning of energy amongst the component fluxes. On the other hand, a large change in the resistance coefficient can have a marked effect on the atmosphere. For example, increasing the coefficient to 100 sec/cm for sand and trees (σ_f = 0.90) caused a 54% increase in the total sensible heat flux to the atmosphere—— an example of what Deardorff termed "foliage fever".

There is some ambiguity in choosing the weighting coefficients for defining q_{af} and T_{af} (III.E.13 and III.E.14). Deardorff selected his values by attempting to match sampled data. But equivalent data were not available for this study. A test whereby the coefficients were changed from

(0.6, 0.3, 0.1) to (0.45, 0.45, 0.1) for a case where trees shaded 90% of a sandy ground caused a 10% change at 1315 LST in the <u>total</u> latent heat flux.

Since no sampled data were available for south Florida, a direct check of the vegetation parameterization was not possible. Thus an alternative means was sought. For example, downward midday longwave fluxes beneath forest canopies on sandy clay and marsh reached an intensity of about 570 watts/m^2. This compares well with hypothetical results in Gates (1962) for a deciduous forest on a clear day (515 watts/m^2) allowing for the fact that the computed foliage temperatures were 7 - 9°C warmer than those assumed by Gates. Over bare soil the downward longwave flux averaged 392 watts/m^2 over the same time period.

A comparison was also made of the sensible heat flux emitted from the canopy with the sensible heat flux diagnosed from an equation for heat flow by conduction through the laminar boundary layer. Intuitively the two fluxes should be equivalent. The conduction equation is

$$H = 41860 \frac{k}{\delta} (T_{af} - T_f) \quad (watts/m^2) \;,$$

where $k = 6.0 \times 10^{-5}$ cal/sec/cm/deg C is the thermal conductivity for air at 20°C and δ is the thickness of the laminar layer (about .3 cm), defined by

$$\delta = \frac{55\nu}{v} \;.$$

Here v is the air speed just above the canopy and ν is the kinematic viscosity for air, assumed to equal 0.14 cm^2/sec.

Predicted sensible heat fluxes and fluxes diagnosed by the relationship above are compared in Figure 29. The better agreement occurs for the forest (Figure 29a) where the maximum discrepancy is less than 18%. However, the disagreement for the simulated grassland fluxes (Figure 28b) is quite large, peaking at 70%. The error is likely due to the selection of the leaf area index since it is the most influential adjustable parameter in equation III.E.15. In a test run, where the leaf area index of the grass was increased from 7 to 20, the predicted sensible heat flux at 1300 LST was 20% greater than the flux diagnosed from Gates' conduction equation. This suggests that the leaf area index should be greater than seven for grasses, at least in the context of the parameterization employed here. The most desirable means to determine a value for the index is to perform a case study for which information on observed heat fluxes is available.

Comparisons were made between runs which parameterized sandy loam soil with and without a canopy of trees ($\sigma_f = 0.90$) in Figures 30 and 31. The maximum surface temperature increased due to reduced air speed and the diurnal range increased by 0.2°C beneath the tree canopy. However the morning profiles the next day are nearly identical.

Moisture depletion is very strong at the surface of the bare soil during the day with no noticeable loss of moisture below 15 cm. Less surface moisture is lost beneath the canopy, but root uptake is evident to a depth of 20 cm. The

Figure 29. Comparison between the predicted sensible heat flux from simulated foliage and the heat flux diagnosed using an equation for heat conduction through the laminar boundary layer above the surface of a leaf. a. Sand with trees ($\sigma_f =$ 0.90) b. Sand with grass ($\sigma_f = 0.75$) Negative fluxes are directed toward the atmosphere.

SENSIBLE HEAT FLUX.
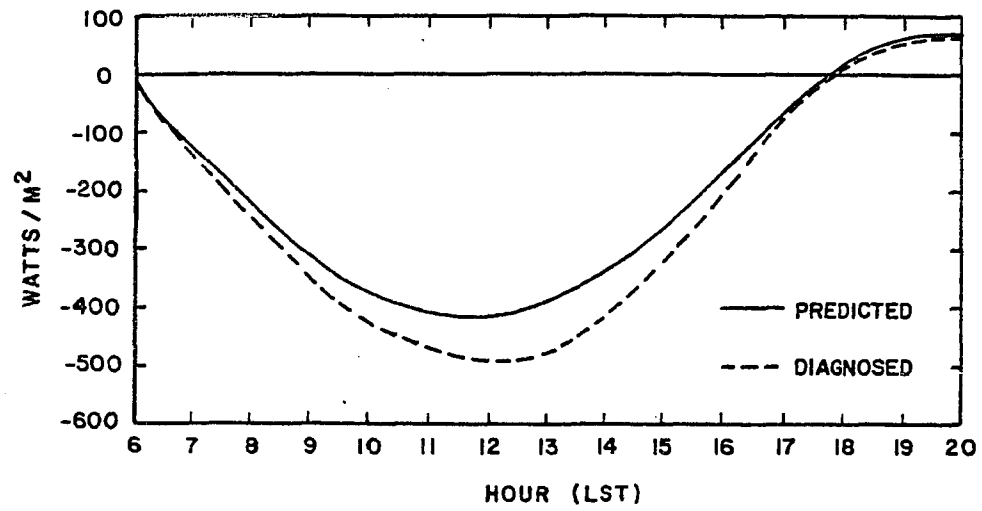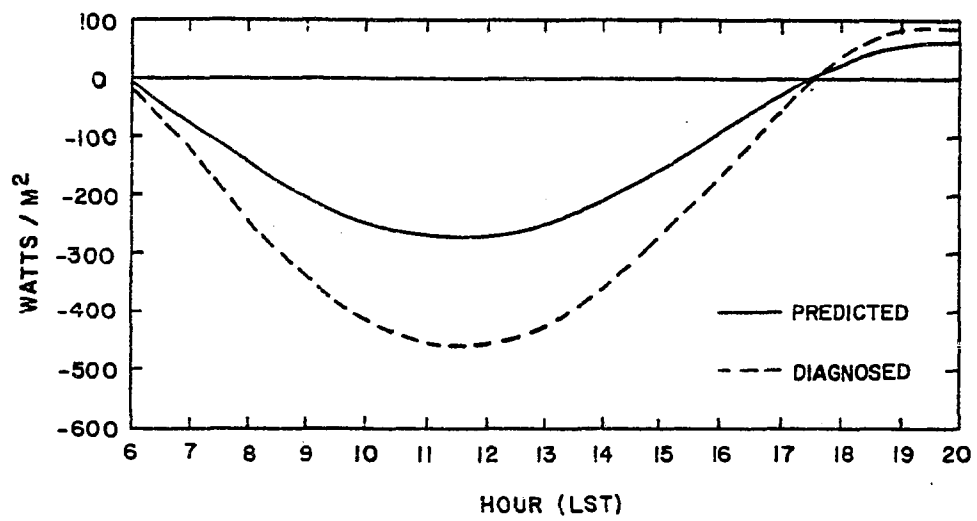
a.

b.

Figure 30.   Profiles of predicted soil temperatures (^{O}C) for early

afternoon (1315 LST) and at sunrise the following morn-

ing (0515 LST).   a. afternoon profile   b.   morning profile

Figure 31. Same as Figure 30, except for the predicted soil moisture content (cm^3/cm^3).

SOIL MOISTURE

a.

SOIL MOISTURE

b.
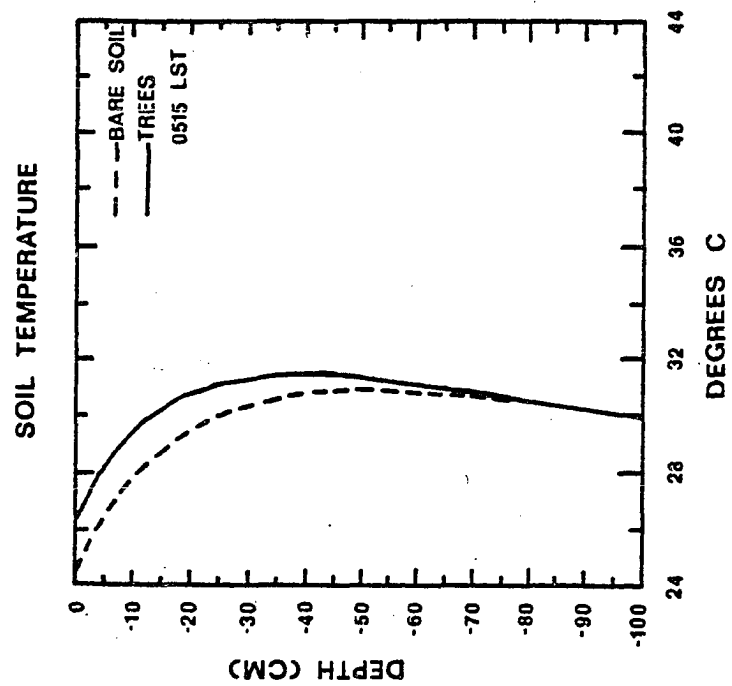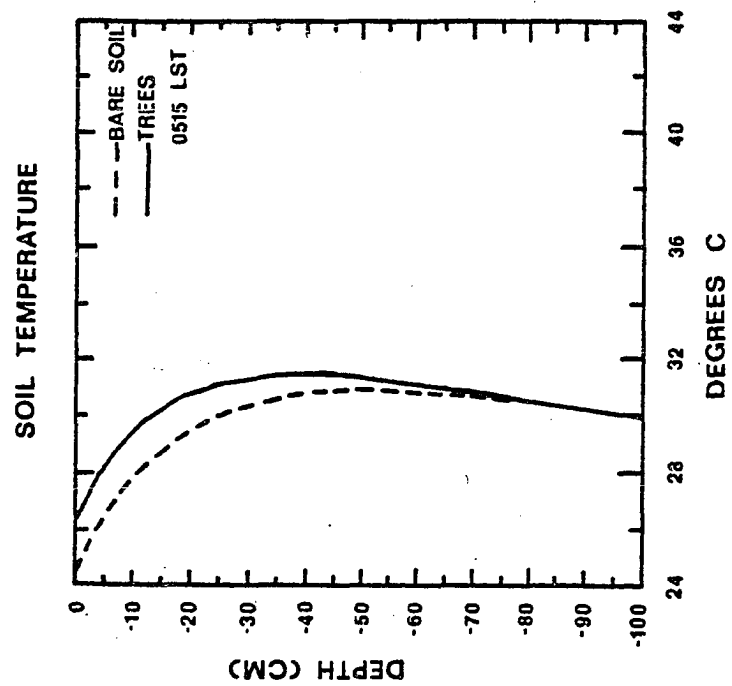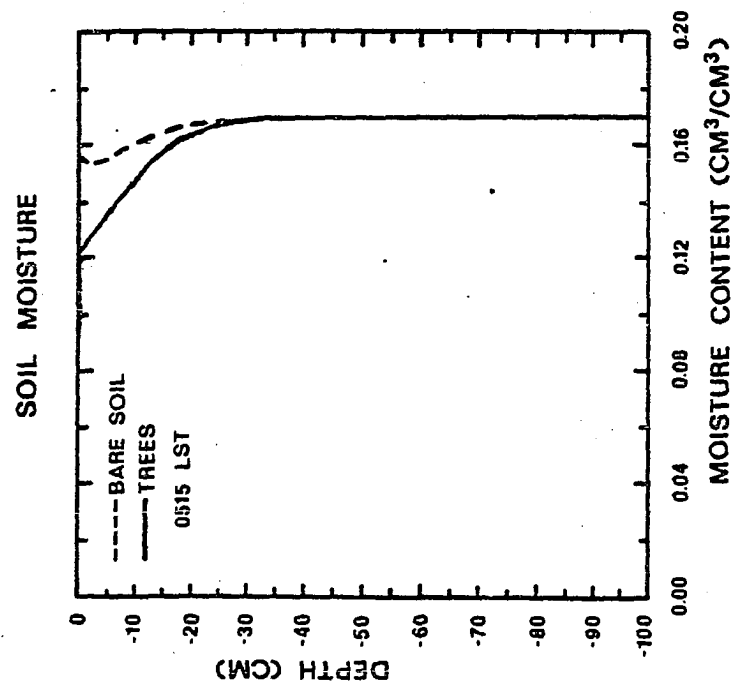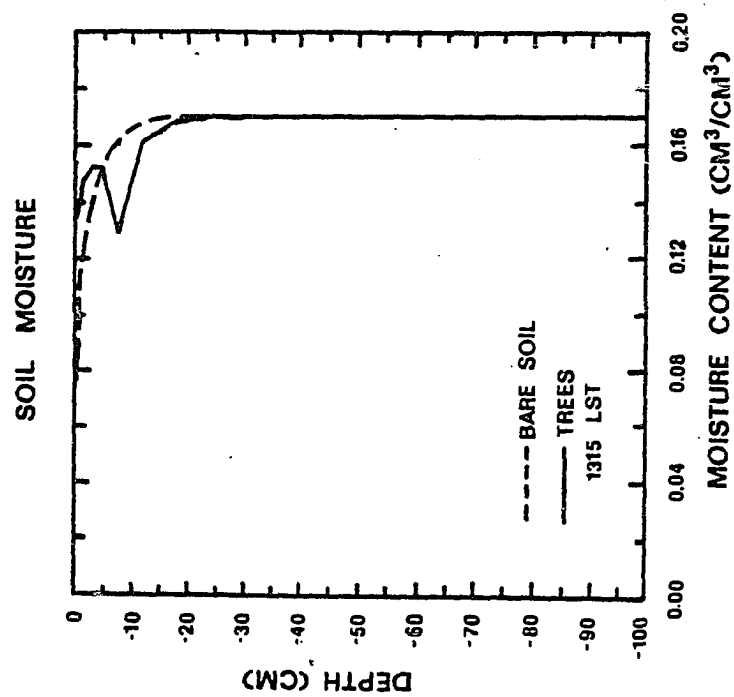
moisture minimum near 10 cm was determined by the root distribution function used. By morning, redistribution of soil moisture smoothed the profile, but the recovery toward the initial state (0.17 cm^3/cm^3 at all levels) significantly lagged the recovery in the bare soil. The slight downward moisture flux at the bare soil surface was due to dewfall, which was experienced at night by each of the bare soils, except sand. Dew did not form when a layer of foliage was present.

Some effects of a foliage layer on the overlying atmosphere are illustrated in Figures 32 and 33. Again, the soil type is sandy loam and the canopy is representative of a forest which shades 90% of the ground.

By early afternoon the depth of the boundary layer was about 60% greater over the forest than over the bare soil, reaching a height of 1600 - 1700 meters. The temperature of the bare soil surface and the plant surface differed by only 0.3°C at 0515 LST the next morning, which may account for the similar depths of the nocturnal inversion. The importance of the foliage layer as a source of sensible heat in this simulation is apparent from the area between the plotted curves in Figures 27 b.

Wind speeds above the canopy were lessened during the day (with respect to the bare ground), especially in the lowest hundred meters. At 1315 LST the peak wind was displaced upward to 1.2 kilometers, signifying strong drag forces which restrained flow within the boundary layer. A

Figure 32. Vertical profile of the atmospheric potential temperature

(K) for early afternoon (1315 LST) and at sunrise the

following day (0515 LST). a. afternoon profile b. morning

profile

POTENTIAL TEMPERATURE

- - - BARE SOIL
—— TREES

0515 LST

b.

POTENTIAL TEMPERATURE

- - - BARE SOIL
—— TREES

1315 LST

a.

Figure 33.   Same as Figure 32, except for the wind speed (cm/sec). An

additional plot is made for early morning of the first day

(0715 LST). Notice the development of the nocturnal jet

at low levels.

WIND SPEED

CM / SEC

b.

Z (KM)

—— 0715 LST
—·— 1315 LST
····· 0515 LST

WIND SPEED

CM / SEC

a.

Z (KM)
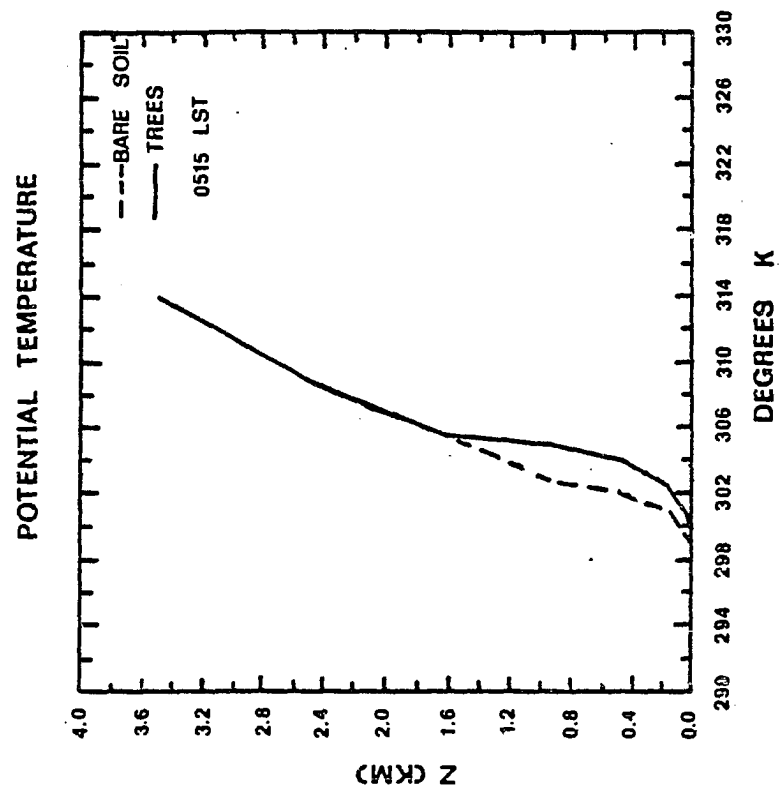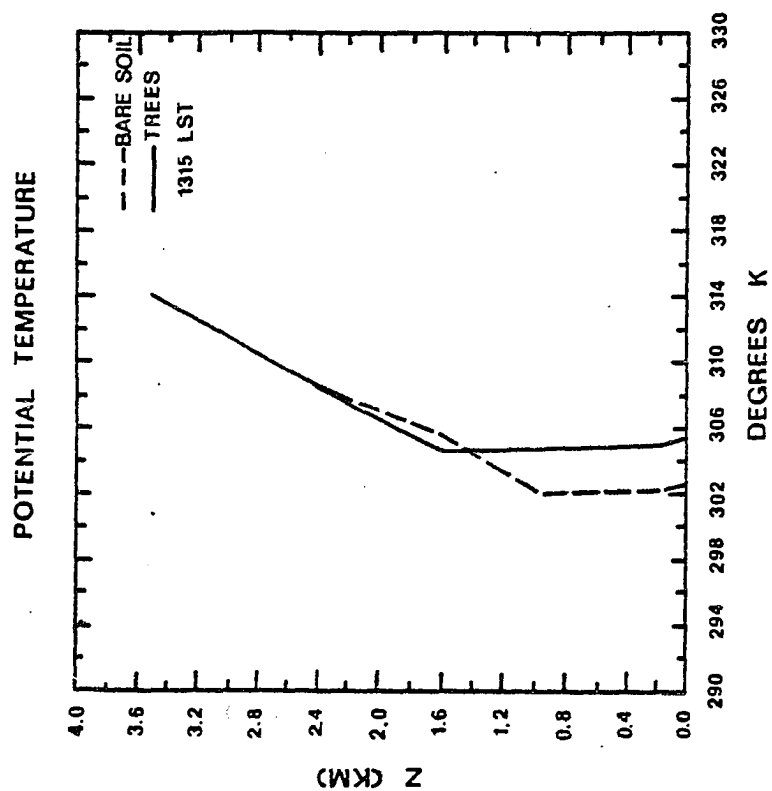
—— 0715 LST
—·— 1315 LST
········ 0515 LST
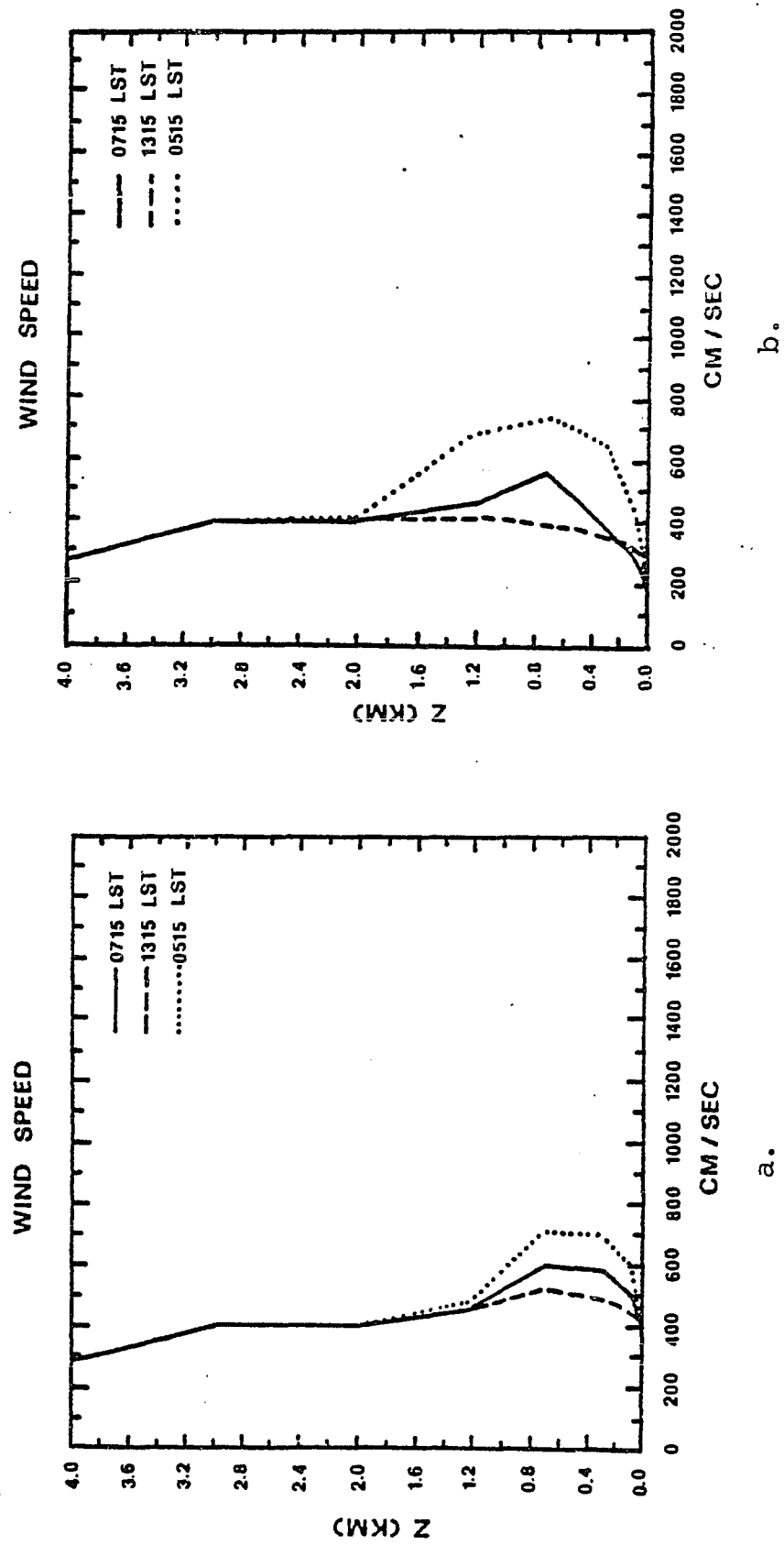
displacement is not evident for the bare soil. An inversion which formed prior to sunset below a height of 200 meters decoupled winds aloft from the surface. Removal of the surface stress caused an imbalance between the pressure gradient and the coriolis forces above the new boundary layer. As shown by Blackadar (1957), the inertial oscillation which resulted accelerated the wind to supergeostrophic speeds in the early morning hours.

Both diagrams show the emergence of a low level jet in the vicinity of 650 meters which is stronger than the initial wind (essentially the wind at 0715 LST). Several implications are apparent. If these one-dimensional results can be extended to three dimensions, then they suggest that convective storms may develop preferentially near the boundaries of relatively flat and aerodynamically rough areas at night as a result of speed convergence of the nocturnal jets downwind of the rough surface (McNider, personal communication). Also, note that the large vertical shear beneath the jet in Figure 28 b is twice the magnitude of the shear which developed over the bare soil. The simulated results suggest that the hazard presented to aircraft by a nocturnal jet may be reduced by situating the runways in an area which is aerodynamically smooth.

F.   Summary

Sensitivity tests support the findings of Gannon (1978) that moisture is the most important soil variable in affecting the turbulent fluxes of heat and moisture to the atmos-

phere. Albedo was much less important and soil type was the least. The degree of wetness of the soil affects the albedo, which in turn regulates the receipt of solar energy. Relative humidity, itself a function of soil moisture, determines the relative partitioning of surface energy into sensible and latent heat. Even the soil heat flux is influenced by wetness, since thermal conductivity is closely related to moisture tension.

Soil moisture must therefore be carefully predicted in a numerical model if realistic results are to be obtained. Three slab prediction schemes inaccurately predicted the phase and magnitude of surface soil moisture. Both the latent and sensible heat fluxes were affected, resulting in erroneous atmospheric forcing.

Vegetation principally enhanced the turbulent exchange of both the momentum and sensible heat fluxes. The latter increased as much as three-fold. On the other hand, latent heat fluxes were predicted at or below bare soil values. If drier soils and lower resistance coefficients for the foliage are used, the latter result would probably be reversed.

The results of these experiments also present implications regarding the effect of overgrazing. In this model the loss of vegetation would dry the surface soil and increase the surface albedo. If the modelled sand is taken to be a representative dry soil, then the effect would be to raise the surface temperature, which would stimulate stronger turbulent fluxes. This opposes the observations of Otterman

(1974) and Otterman (1975), where the overgrazed Sinai desert was cooler than the nearby Negev. However, the Sinai albedo was estimated to average about 0.47 for all wave- lengths and it was greater than 0.50 in the infrared. The present model restricts the soil albedo to a maximum value of 0.31 (equation III.B.10). It is probable that overgrazing would cool the surface if the albedo were permitted to seek a value similar to that of the Sinai. Mahrer and Pielke (1978) showed, via a numerical simulation, that a change in the regional albedo of the magnitude observed by Otterman could have an important effect on local circulations (this supported Otterman's speculation).

VII. Three-Dimensional Sensitivity Experiments

The first attempts to model south Florida sea breezes in three dimensions (Pielke, 1974; Tapp and White, 1976) prescribed surface heating via a sinusoidal forcing function. Even though the heating was applied uniformly across the peninsula, reasonable sea breeze convergence was achieved. This demonstrated that the dominant mode of the forcing requisite for sea breeze development was a strong thermal contrast through a deep atmospheric layer between the cool ocean and the heated land.

Predicting the surface temperature using a surface energy budget (Hsu, 1978; Mahrer and Pielke, 1978; Carpenter, 1978; Carpenter, 1979; Gannon, 1978) improved the general applicability of numerical modelling. The heating was free to respond to atmospheric variability, which permitted spatially inhomogeneous forcing. Mahrer and Pielke concluded that although their simulation was intuitively more realistic by predicting thermal forcing, the gross features of the sea breeze circulation were largely unaltered when the ground surface was homogeneous.

Gannon (1978) demonstrated that surface heterogeneity significantly influenced the strength of sea breeze convergence in his two-dimensional simulation of a south Florida sea breeze. He observed that the surface sensible heat flux was the most important forcing parameter and that it was predominantly regulated by soil wetness. Carpenter (1978) reinforced this finding, noting that his simulated

sea breeze was more intense and advanced 20 kilometers further inland when the surface resistance to evaporation was increased. Gannon also examined the impact of non-precipitating clouds on the sea breeze. He found that thick cirrus clouds (i.e. geometric thickness greater than two kilometers) inhibited sea breeze development, whereas thinner clouds displaced the convergence and intensified it by as much as a factor of two.

Three-dimensional numerical simulations were used to evaluate the development of a sea breeze circulation for three increasingly complex surfaces. One simulation assumed that the surface was a uniform bare soil. Another included a parameterization of heterogeneous bare soils, while a third run added vegetation to the heterogeneous soils.

Precipitation was included in two additional experiments, which tested the importance of the release of latent energy on the development of mesoscale convergence. Mixed soils both with and without vegetation served as the surface condition.

A. Dry Experiments

The Miami 1200 Z (0700 LST) sounding for July 17, 1973, shown in Figure 6, was used to initialize the model atmosphere. All runs began with an atmosphere which was assumed barotropic. The initial boundary layer height was placed at 660 meters, below which the wind was in Ekman balance. At the top of the boundary layer, the geostrophic wind was from the East at 6 m/sec, backing to 4.71 m/sec

from the Northeast above four kilometers (Table II). The remaining initial conditions were specified in section V.

Maps of soil type, canopy type and vegetation shielding factors are needed to specify the heterogeneous surfaces. All other variables are determined from tables of values as a function of soil or canopy type so that they need not be mapped.

The mean soil distribution in Figure 34 was determined from the General Soil Map of Florida (Conservation Services of the U. S. Department of Agriculture, Gainesville, Florida). It represents the array which was used by the numerical model. Sand is the most abundant type of soil. It covers much of the west and northwest and a strip of sand also extends nearly the length of the peninsula along the east coast. A broad band of peat lies in the east ranging from Lake Okeechobee southward to an extensive marsh which occupies most of the southern extremity of Florida. Sandy clay covers the remainder of the southern third of the land area while sandy loam is generally situated in the proximity of the lake.

South Florida vegetation is very heterogeneous on a subgrid scale. In the interest of simplicity the description of vegetation was therefore confined to two broad categories-- trees and grasses. The General Map of Natural Vegetation of Florida (Davis, 1967) was used to estimate the vegetation mosaic. Only the dominant canopies are depicted in Figure 35 .

Forests prevail in much of the west and northwest and

144

Figure 34. Soil types used in the south Florida simulations.

LEGEND

1 MARSH

2 PEAT

3 SAND

4 SANDY CLAY

5 SANDY LOAM
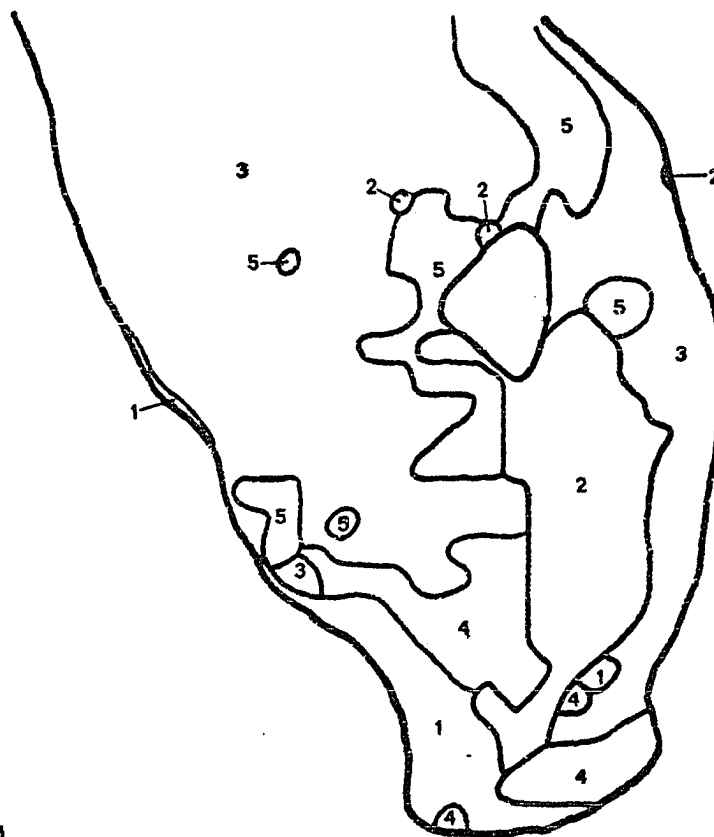
Figure 35. Distribution of the types of plant canopies used in the south Florida simulations.

LEGEND

1 TREES

2 GRASSES

in most coastal areas. Grasslands cover the interior of
Florida south of Lake Okeechobee including the Everglades.
Some grassland also extends north of the lake roughly
parallel to the Atlantic coast.

Vegetation shielding factors in Figure 36 further
subdivide the major canopy types. Odum (personal communica-
tion) kindly provided the estimates. These values are most
difficult to assign for two reasons. First, the natural
vegetation has been altered by cultivation and development
of the land. Second, and most important, a single vegetative
cover is required to represent a grid area which in reality
is quite heterogeneous.

Run A represented the common type of mesoscale simulation
which presumed that the ground surface was homogeneous. Bare
sand was applied to all land areas. A heterogeneous matrix
of bare soils characterized Run B. Although the types of
soils differed, the distinction was principally one of soil
wetness. The most complex surface was modelled in Run C.
The vegetation canopies described by Figure 35 were combined
with the mixed soils of Run B.

A complex surface affects the atmosphere in many ways.
For instance, changes in roughness affect the intensity of
turbulent mixing, while moistening the soil accentuates
latent heat fluxes at the expense of sensible heat fluxes.
However, the overriding consideration for the development of
a dry sea breeze circulation is the degree to which the
atmosphere is heated. The predicted soil temperatures for

Figure 36. Map of the foliage shielding factors used in the south Florida simulations.

LEGEND

A 0.50
B 0.75
C 0.85
D 0.90
E 0.98

1315 LST in Figure 37 show that the effect of changeable surface conditions can be substantial. Soil temperatures, and subsequently air temperatures, steadily increased toward the leeward coast (i.e. west coast) when the soil was uniform. Interspersing several different soils across Florida created a patchwork of hot and cool spots which generally damped sensible heat transfer. Horizontal gradients of surface temperature and sometimes the temperatures were reduced beneath vegetation, although this is somewhat misleading since the plant canopy was nearly always the primary source of sensible heat.

The relationship between surface conditions and the organization of mesoscale convergence is illustrated in Figures 38 and 39 . The data represents a cross- section taken over the peninsula south of Lake Okeechobee. Moist soil was cool since a large fraction of the net radiation was used to evaporate soil water. Correspondingly the sensible heat flux was quite weak. On the other hand, the sensible heat flux was much larger for sand. Its moisture supply was limited so that most of the energy was channelled into heating the soil.

The intensity of the west coast convergence, indicated by the strength of the ascending air (Figure 38), was directly linked to the magnitude of the sensible heat flux.

Convergence associated with the sea breeze was ill-defined and weak in Run B since cool surfaces diminished the supply of warm bouyant air. In Run C the canopies enhanced

Figure 37. Predicted soil surface temperatures at 1315 LST for south
Florida. The contour interval is 5.0 ^{O}C. a. Run A (all
sand) b. Run B (mixed dry and moist soils) c. Run C
(mixed soils of Run B overlain by vegetative canopies).
The coolest soils in b and c are located south of Lake
Okeechobee.

a.

b.

c.
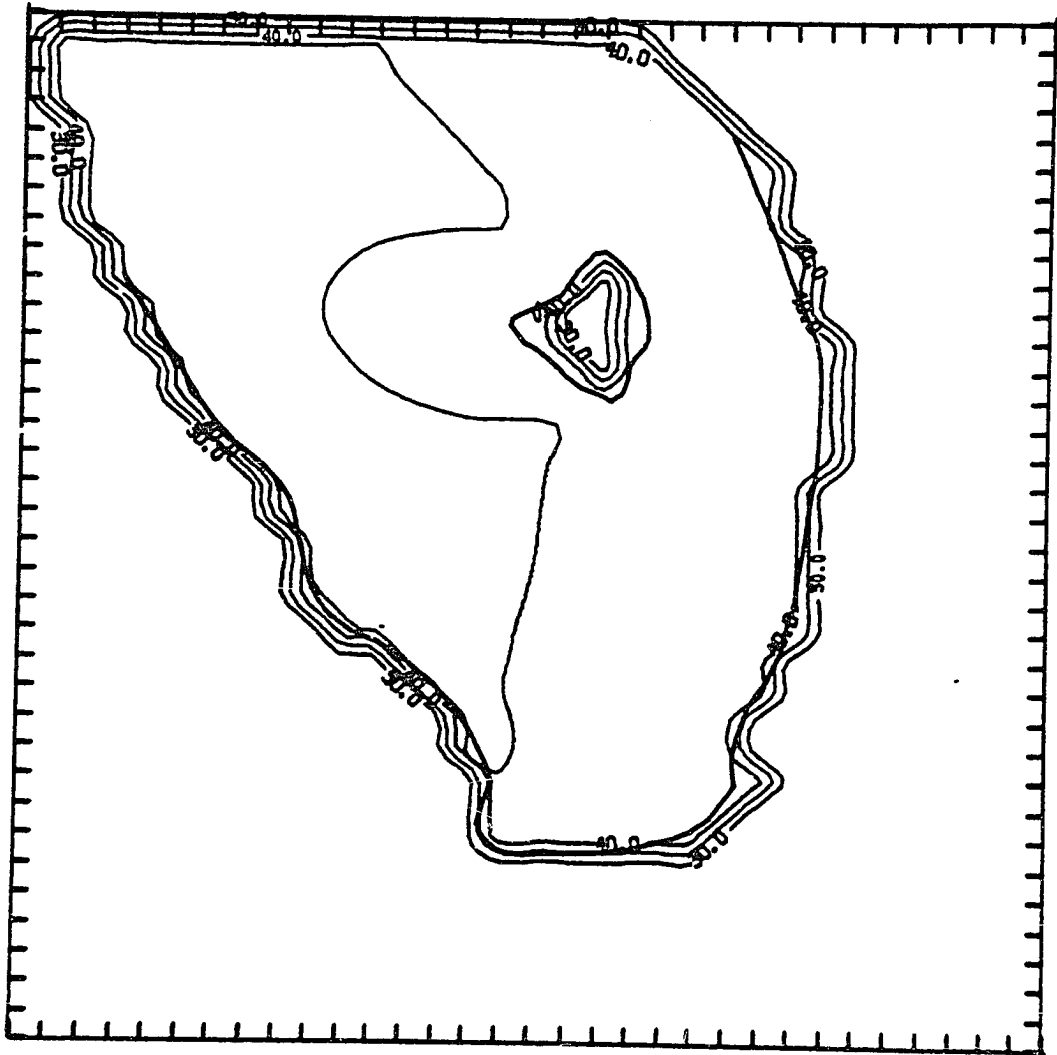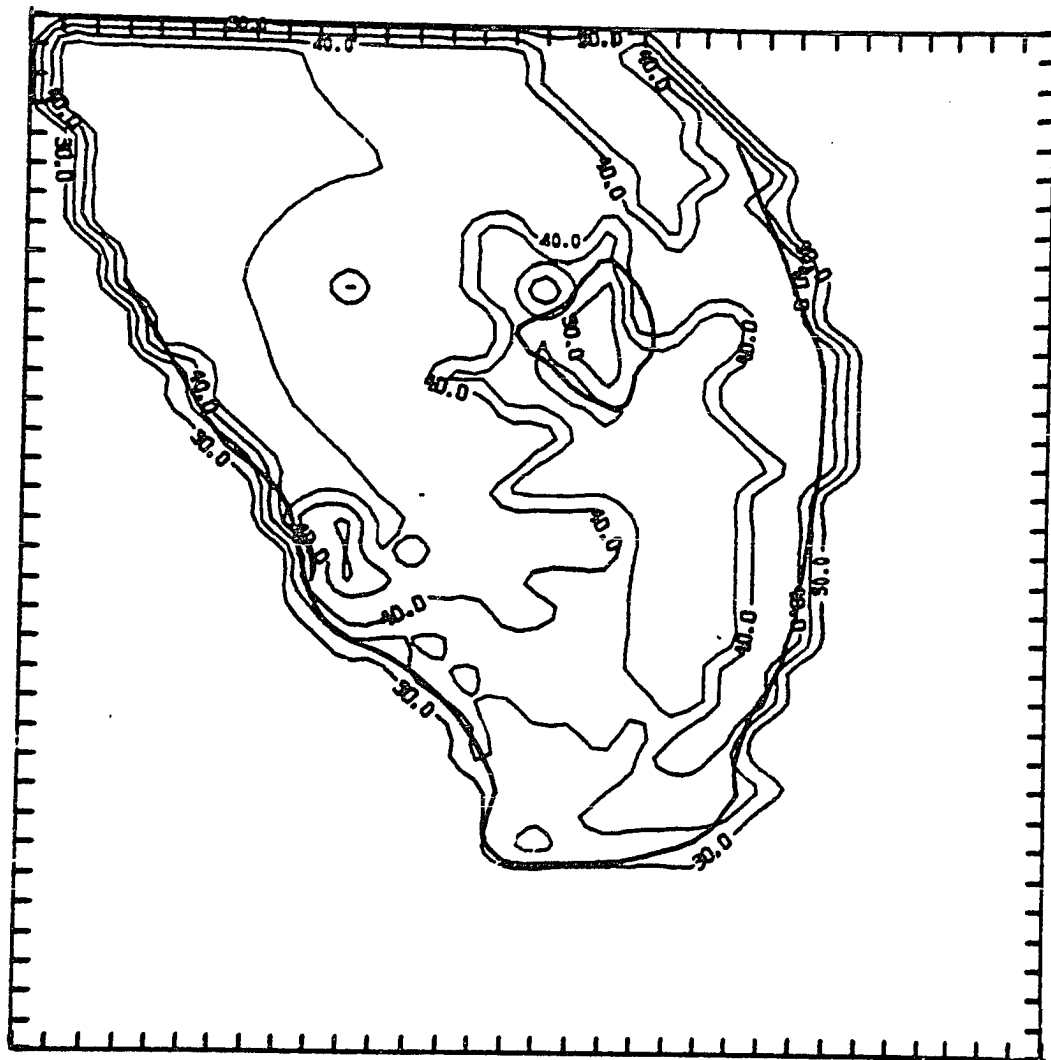
Figure 38. Comparison of ground surface temperature, vertical velocity

and sensible heat flux from the surface. The times chosen

roughly correspond to the time of peak value of each para-

meter. a. Predicted ground surface temperature (^{o}C) at

1215 LST b. Predicted vertical velocity at a height of

1200 meters at 1815 LST. Includes the legend for Runs A, B

and C. c. Predicted total sensible heat flux at the sur-

face at 1215 LST. Abscissa is labelled by gridpoint. This

is an East-West cross-section of south Florida corresponding

to row 17.
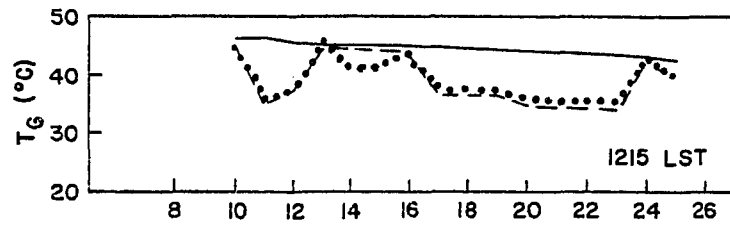
a.
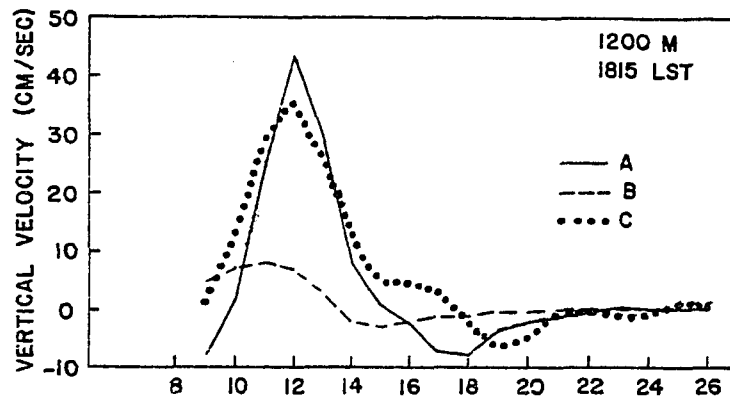
b.
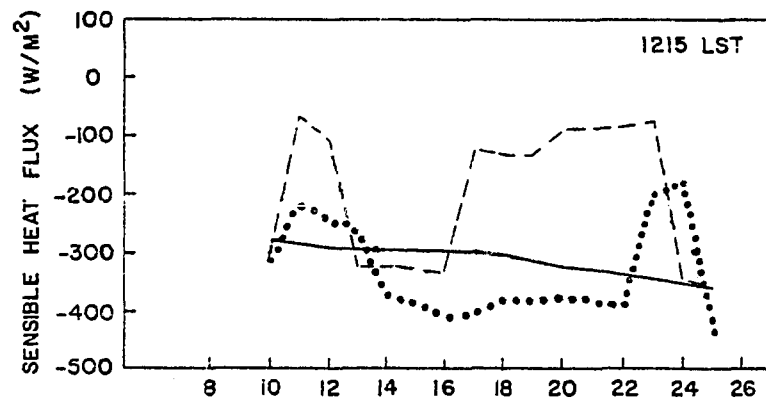
c.

Figure 39. Predicted total latent heat flux at the surface at 1215 LST

for the same cross-section as in Figure 38. Run A is all

sand, Run B is mixed soils and Run C is mixed soils with

vegetation. Soil types and vegetation canopy types assigned

to the gridpoints (abscissa) are given below the figure.

The coasts are located at approximately gridpoints 9 and

25.
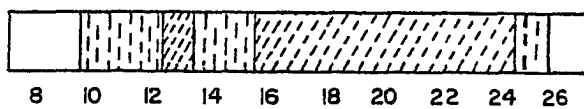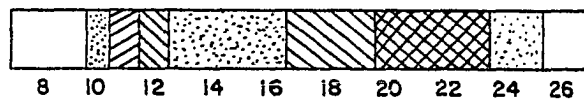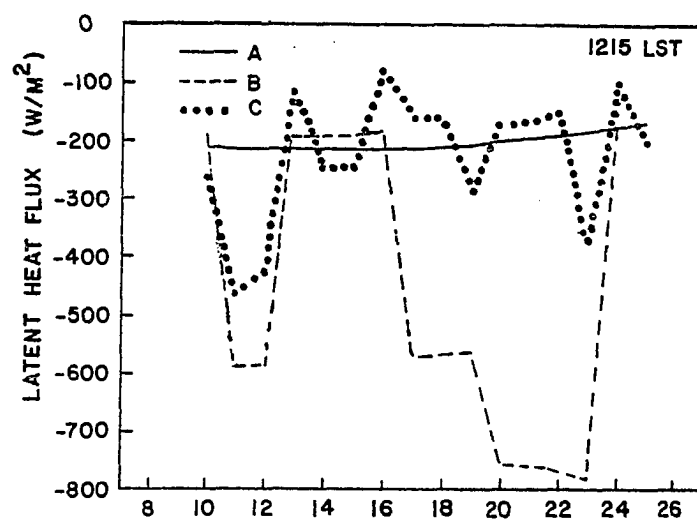
the sensible heat transfer over the moist soils in the east, while sharp decreases near each coast were still very much in evidence. On the west coast the relative minimum in the sensible heat flux reduced the temperature gradient in the atmosphere, resulting in weaker and broader convergence.

Latent heat fluxes varied inversely with respect to the sensible heat. Usually the moist ground evaporated moisture at the potential rate, which accounted for the large fluxes. The very large intensity of the latent fluxes over the peat are due to its low albedo.

A uniform surface is convenient because it is easy to apply. Also it avoids the relative uncertainty which occurs when attempting to specify a matrix of different surface conditions. The price paid is the loss of many small scale circulations which are generated by local and regional inhomogeneities.

This point is illustrated by first examining important surface properties. For example, the temporal variation of the predicted soil surface temperatures in Figure 40 is typical of a homogeneous soil. Predicted temperatures rose slowly, though steadily, toward the leeward coast (i.e. the west coast in this example) due to warming of the advected air. Only a 3°C temperature difference can be seen from coast to coast! At the west coast, the maximum temperature shifted inland at midday, positioned just ahead of the advancing sea breeze front.

The heterogeneous surfaces provided a marked contrast.

Figure 40. Predicted time history of soil surface temperature (^{O}C)

for an East-West cross-section of south Florida (row 17).

The abscissa extends from the west to east coastlines and

it is labelled by gridpoint. a. Run A (all sand) b. Run

B (mixed soils) c. Run C (mixed soils and vegetation)

The distribution of soil and canopy type by gridpoint is

given beneath the figures.

a.

b.

c.

SAND   SANDY CLAY   SANDY LOAM   PEAT   WATER   TREES   GRASS
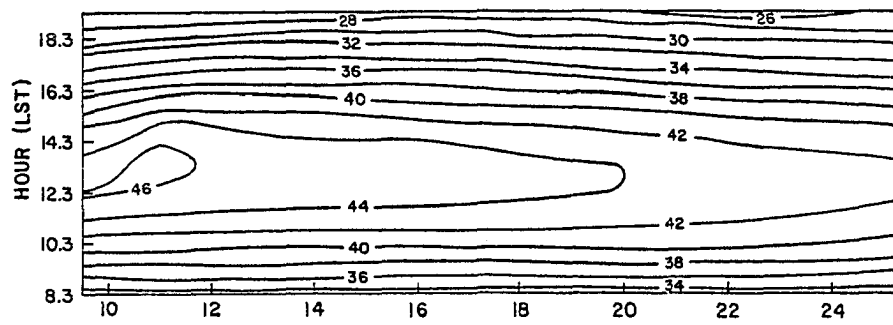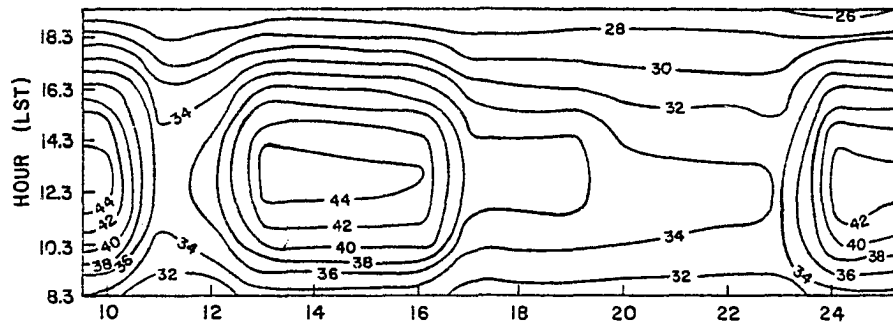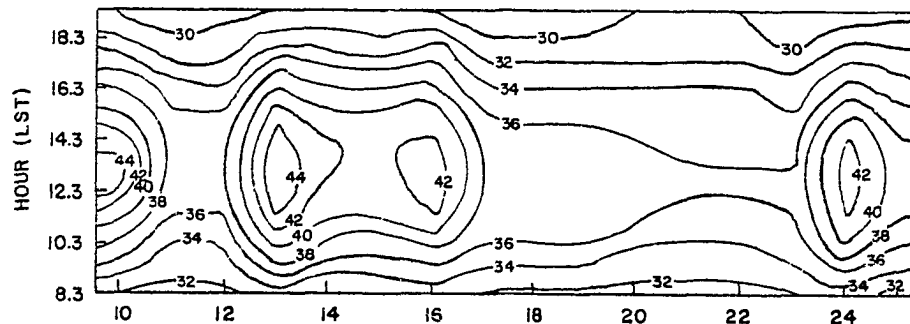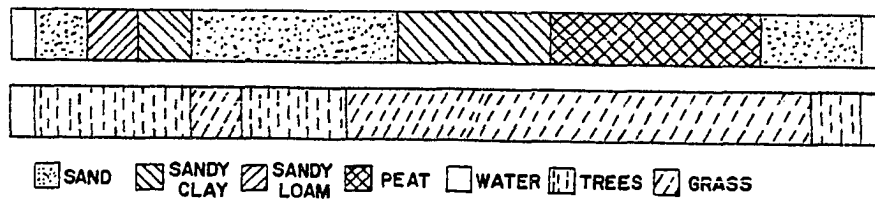
Three distinct hot cells appeared, each corresponding to sandy soil. Intervening areas were much moister and thereby cooler since much of their net radiation was consumed by evaporation and transpiration (Run C). In these experiments temperature differences of up to 10°C occurred at adjacent gridpoints.

An interesting analogy is noted in Figure 41 . Observed surface air temperatures are plotted as a function of local hour for several sites on an east-west line across the Florida peninsula. They correspond to the same cross-section as Figure 40 . The important feature to note here is the remarkable resemblance between the air temperatures and the predicted soil temperatures when the surfaces were inhomogeneous. Agreement is credible for the coastal maxima and for the minimum inland from the east coast. The latter location corresponds to the region where the South Florida Water and Flood Control District impounds water behind a series of canal locks.

Surface energy fluxes (Figures 42 and 43) behaved in much the same manner as surface temperatures. Slow, steady changes across the peninsula typified Run A, while dissimilar surfaces were bounded by sharp flux gradients in the other experiments.

Latent and sensible heat fluxes varied inversely with respect to one another from west to east for a sandy surface. A modest coast-to-coast difference occurred for each flux, peaking at about 30% during the afternoon.

Figure 41 . Time history of observed air temperatures (^{O}C) near
the ground. This East-West cross-section corres-
ponds with row 17 in the model predictions. Data
is missing at station AA1 due to equipment damage.

JULY 17, 1973

TIME E.S.T.

	NOG	NAP AA5	AA4	AA3	AA2	AA1	FXE	FLL	FTL
1900		22.2	22.2	26.1	28.7			27.8	31.7
1800	23.9	22.2	22.2	26.7	27.2		28.9	32.2
1700	24.4	22.2	22.2	27.2	28.3		29.4	35.0
1600	26.7	23.9	22.2	30.6	29.4		30.0	35.6
1500	28.3 27.8	28.3	26.7	28.4	27.8		30.6	35.6
1400	28.3 27.8	36.7	31.7	29.4	27.8		30.6	36.1
1300	32.2 32.2	36.1	30.0	32.8	26.7		30.8	36.1
1200	32.8 30.0	35.6	30.0	32.2	31.1		30.6	33.9
1100	31.1	36.1	26.1	31.7	29.4		29.4	32.8
1000	31.7 31.1	33.9	29.4	29.4	27.4		28.3	32.2
0900	30.0	31.1	27.2	28.3	25.6		26.7	30.0
0800	28.3 27.8	26.7	25.0	26.7	22.8		28.7	28.9 30
0700	25.0	21.1	21.1	22.2	21.7		25.6	27.8
0600	22.8 23.3	18.9	20.0	21.1	21.1		24.4	26.7
0500		18.0	20.0	21.1	21.1		25.0	26.1

Figure 42. Same as Figure 40, except for total sensible heat flux
(watts/m^2). Distribution of soil and canopy types is
given in Figure 40.
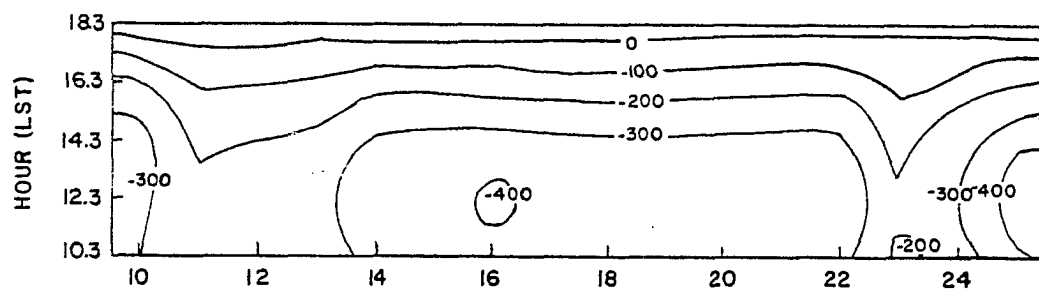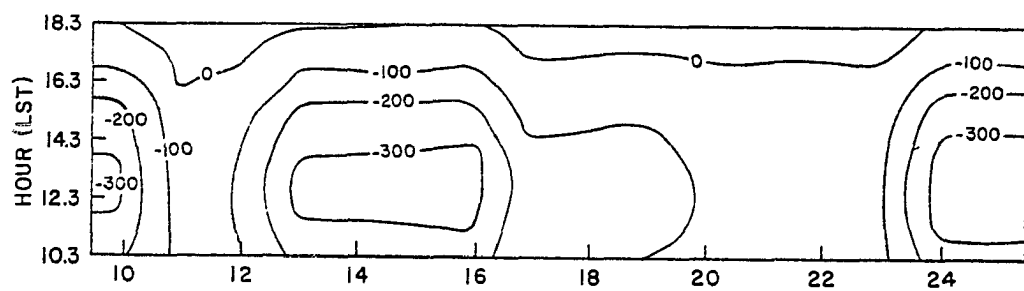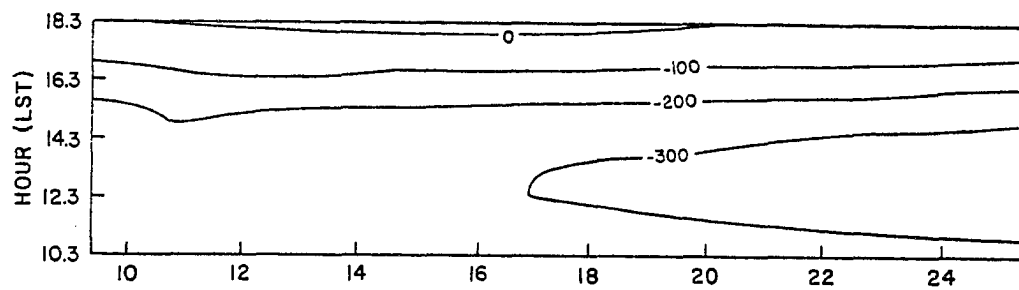
Figure 43. Same as Figure 40, except for total latent heat flux
(watts/m^2). Distribution of soil and canopy types is
given in Figure 40.
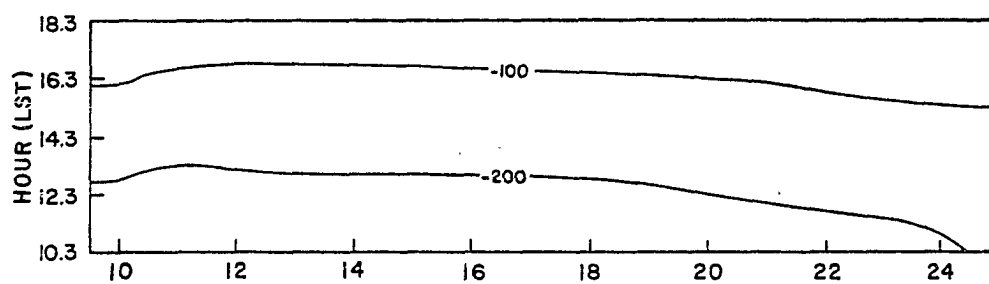
a.
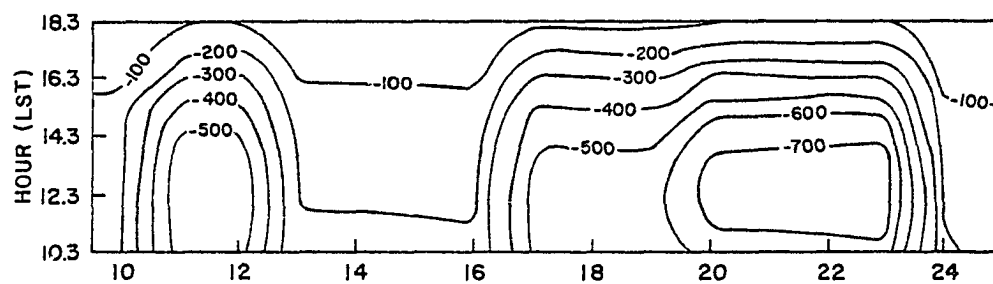
b.
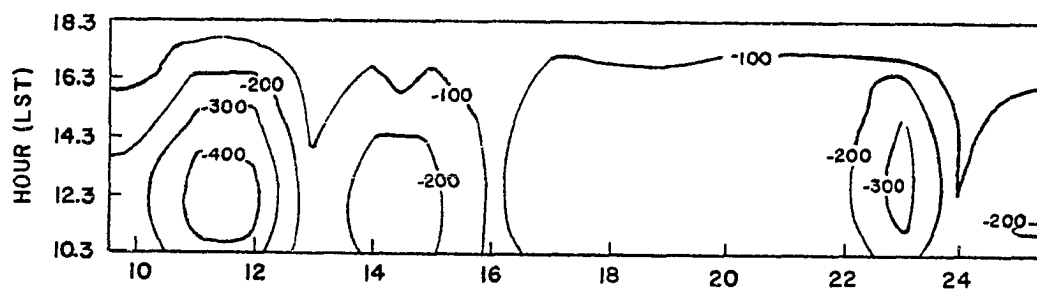
c.

Moist soils in Run B were weak sources of sensible heat, yet prolific sources of latent heat. They exported moisture into the atmosphere at rates which approached four times that of sand.

The primary source of sensible heat was elevated from the ground to canopy level when vegetation was dense. In Figure 42 sensible heat fluxes increased more than 100 watts/m^2 over much of the wettest ground, thereby smoothing horizontal gradients. However, the influence of moist soils is still recognizable near each coast!

Transpiration increased moisture fluxes over sand up to 15% (Figure 43). But the strong fluxes over peat and sandy clay decreased 70% or more at midday because the foliage shaded most of the surface. This cooled the ground and reduced the surface relative and specific humidities. Had the bare soil evaporated moisture below the potential rate, the relative contrast between experiments B and C would be accentuated.

Mixed soils always evaporated more moisture into the lower atmosphere than did bare sand. The upper set of curves in Figure 44b show that mixed soils overlain by vegetation added about one g/kg at a height of 200 meters in the interior of the land area, while bare moist soils supplied an additional three g/kg. But the boundary layer heights in Figure 44a indicate that thermal forcing was weak to the east in Run B. Judging from the lower curve for Run B in Figure 44b there was no effective mechanism to mix the large

Figure 44. a. Predicted boundary layer height (km) at 1815 LST for

an East-West cross-section of south Florida (row 17).

b. Predicted atmospheric specific humidity. Upper set

of curves applies to a height of 200 meters, while the

lower set of curves applies to a height of 2500 meters.

The abscissa is labelled by gridpoint.
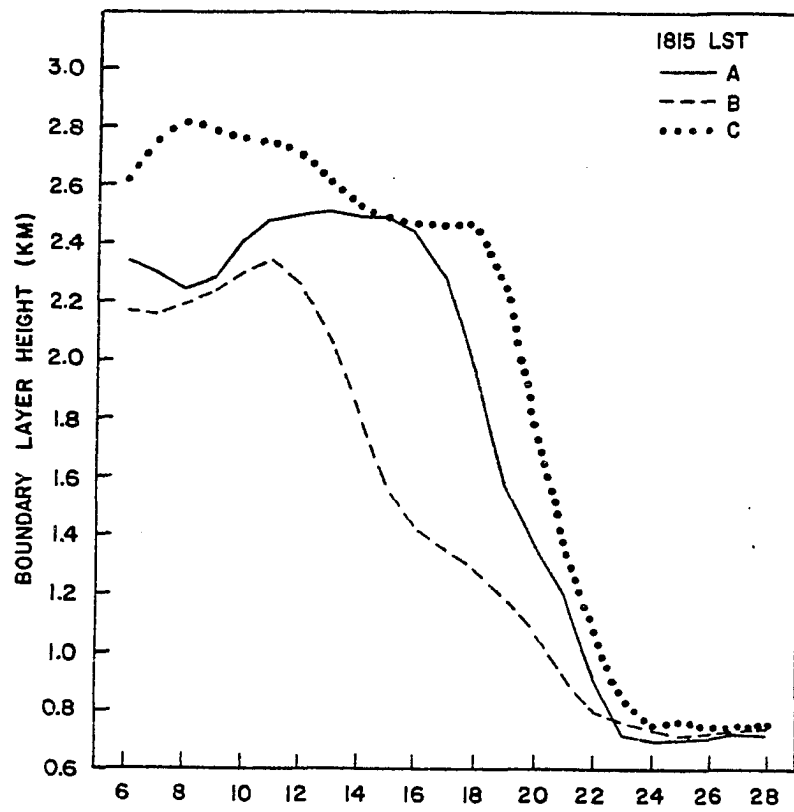
a.
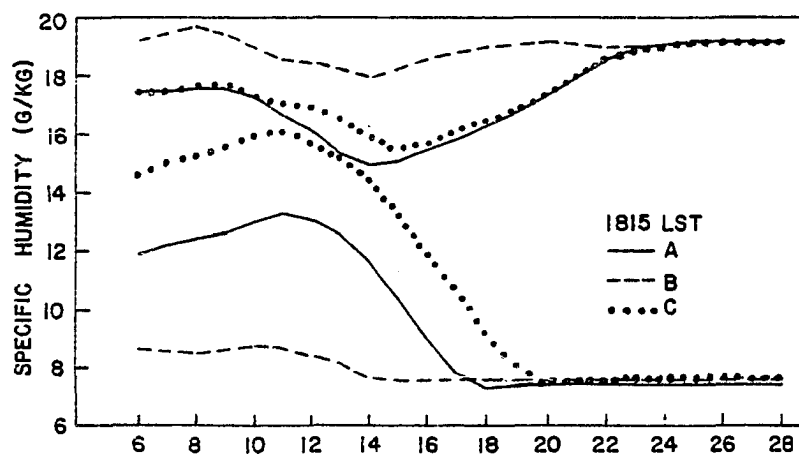
b.

pool of moisture to higher levels, forcing it to accumulate near the surface.

Deep turbulent mixing in the other two experiments raised specific humidities at 2500 meters by at least 5 g/kg above the background values which persisted at 1815 LST over eastern Florida. Near the ground each simulation was drier than Run B due to low level moisture divergence. The consequences of significant moisture transport to higher levels will be apparent when condensation is simulated.

In general mesoscale convergence was most intense when both the thermal contrast was greatest over a long fetch and where the curvature of the coastline was favorable. This meant that along the west coast strongest convergence was situated near sandy soil. For Run A, where sand was the only soil, the sea breeze was relatively strong along much of the west coast by early afternoon (Figure 45). A vertical velocity maximum developed along the concave coastline in the southwest due to marked curvature convergence.

Sea breeze strength was similar for the non-uniform surfaces in Runs B and C during the early afternoon, although the convergence zone was more extensive in Run C. Figures 46 and 47 indicate that to the north the region of greatest intensity (i.e. $w \geq 8$ cm/sec) appears to delineate the boundary of extensive sand. Within this region the vertical velocities were comparable in strength for each of the runs, suggesting that the sea breeze circulation of Run A will develop relatively unaltered, at least up to early afternoon,

Figure 45 . a. Predicted horizontal winds at 25 meters for Run A

(homogeneous sand). Wind speed is proportional to arrow

length with one grid interval equal to 8 m/sec. b.

Predicted vertical velocity at 1200 meters. Contour in-

terval is 4 cm/sec. Dashed lines indicate negative vel-

ocities. Time is 1315 LST.
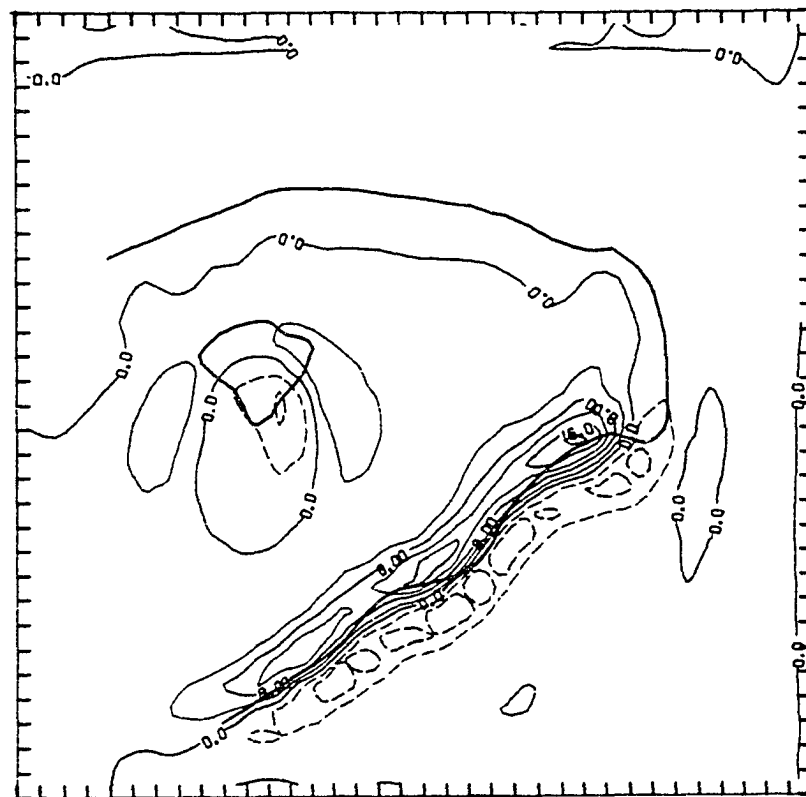
b.
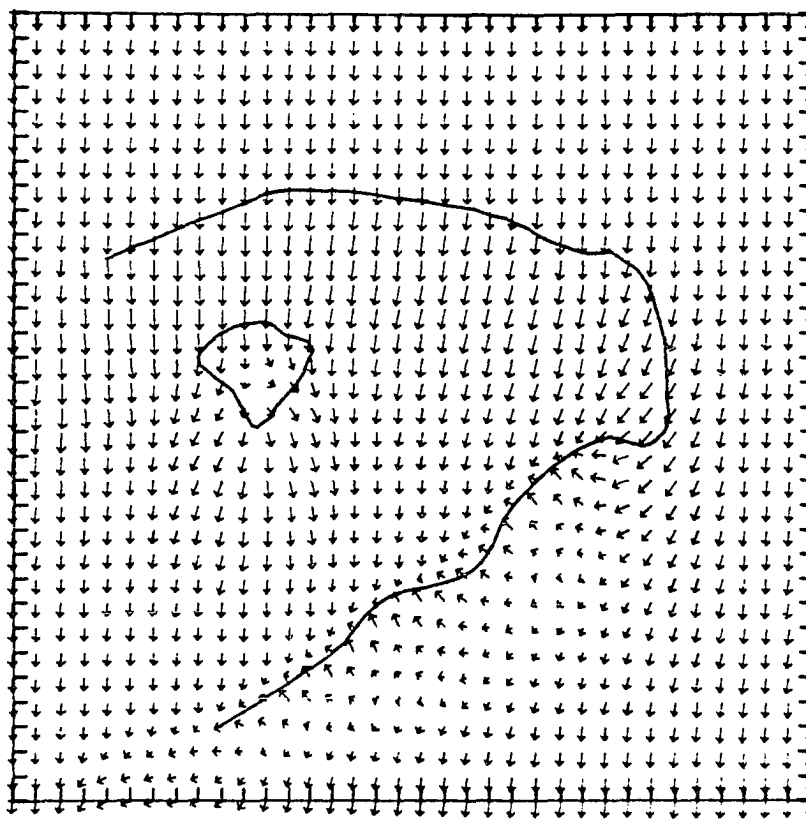
a.

Figure 46. Same as Figure 45, except for Run B (mixed bare soils).
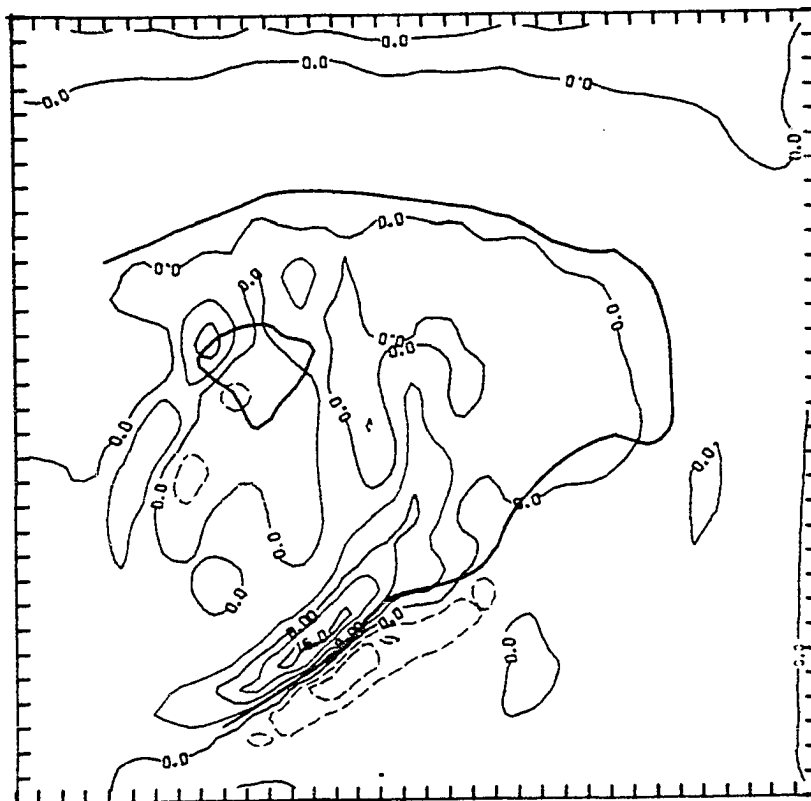
b.
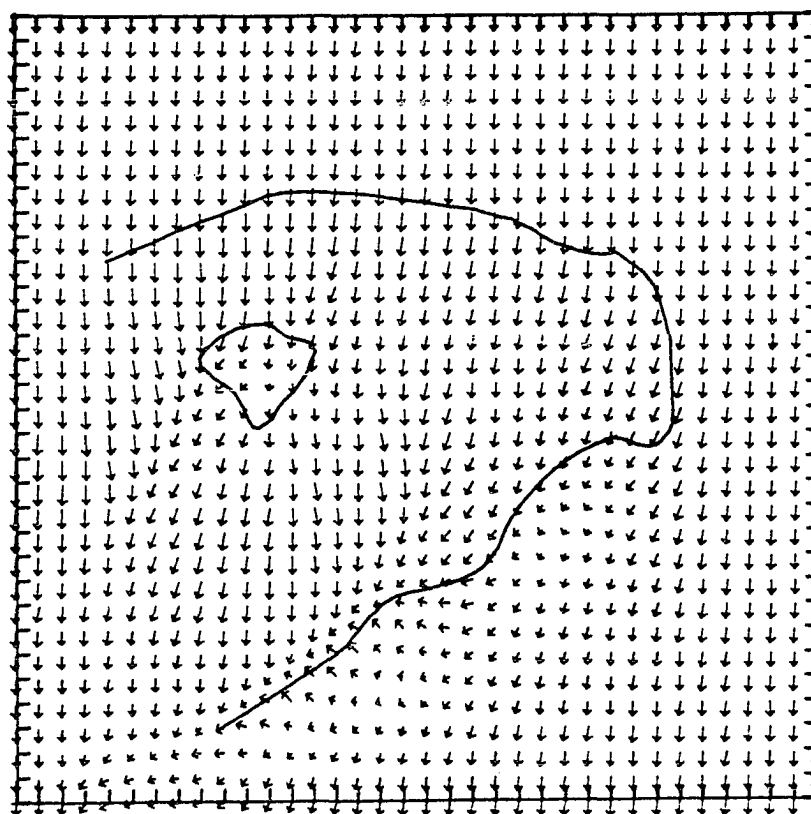
a.

Figure 47. Same as Figure 45 , except for Run C (mixed soils and vegetation).
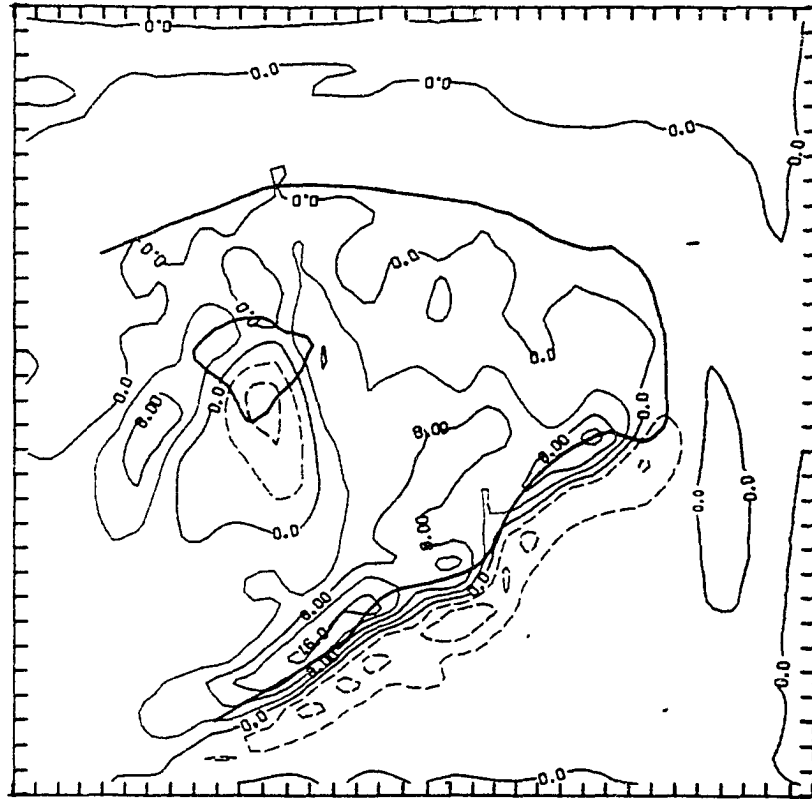
b.
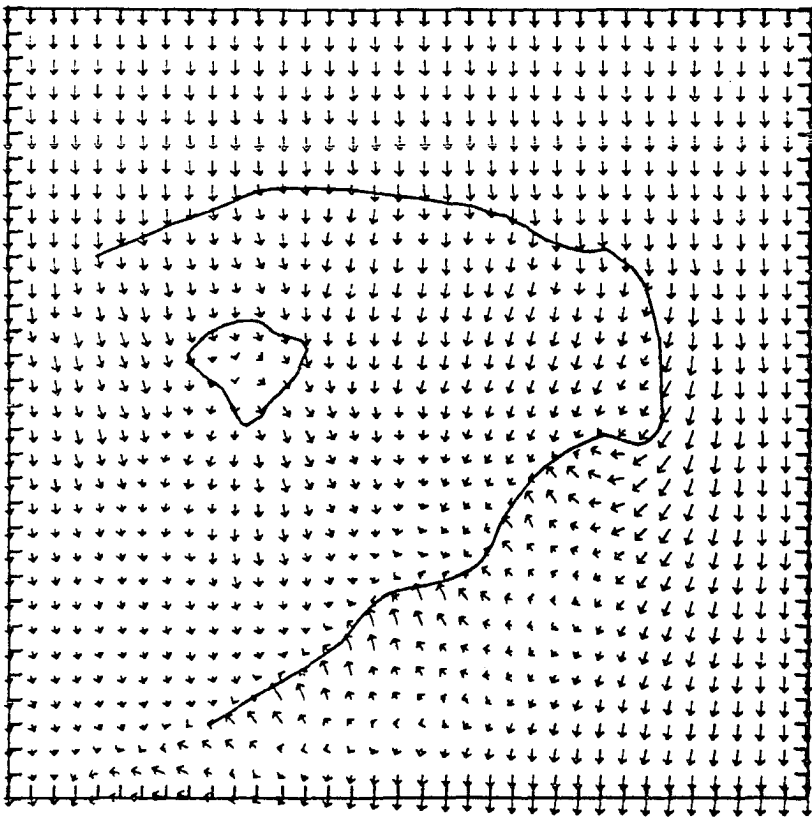
a.

wherever there is sufficient sand upwind.

The sea breeze had advanced only a small distance inland on the west coast by 1315 LST. Maximum penetration varied from 5 - 7 kilometers and it always occurred over sand. Very little penetration was evident over cool bare soil in Experiment B (Figure 46).

The contrast between the heated land and the cool water of Lake Okeechobee resulted in a lake breeze which produced divergence to the west of the lake. This occurred in every simulation. Subsidence formed over the lake and extended more than 60 kilometers downstream. Divergence to the southwest was negligible for the bare mixed soils since the cool soils to the south of the lake provided weak thermal contrast. However, to the north the cool soils contributed to the divergence. In Runs B and C the predicted divergence was slightly stronger than in Run A and it was displaced about 20 kilometers further to the north.

There was some qualitative agreement between predicted convergence and the location of radar echoes. Figure 48 shows the echoes observed by the Miami WSR-57 radar at 1300 LST. At this time precipitation echoes were scattered through a broad band which extended from northeast of the lake southwestward to the Gulf coast. Within the next hour (Figure 49) a line of echoes developed northeastward from the Gulf coast to the southwestern shore of the lake. This coincided with predicted convergence caused by the lake breeze circulation (Figures 45 and 47) in Runs A and C.

Figure 48 . Shower pattern observed at 1300 LST on July 17, 1973 by the Miami WSR-57 digitized radar. Contours for rainfall rates are drawn for 0.25, 2.29, 13.72, 30.23 and 66.55 mm/hr.
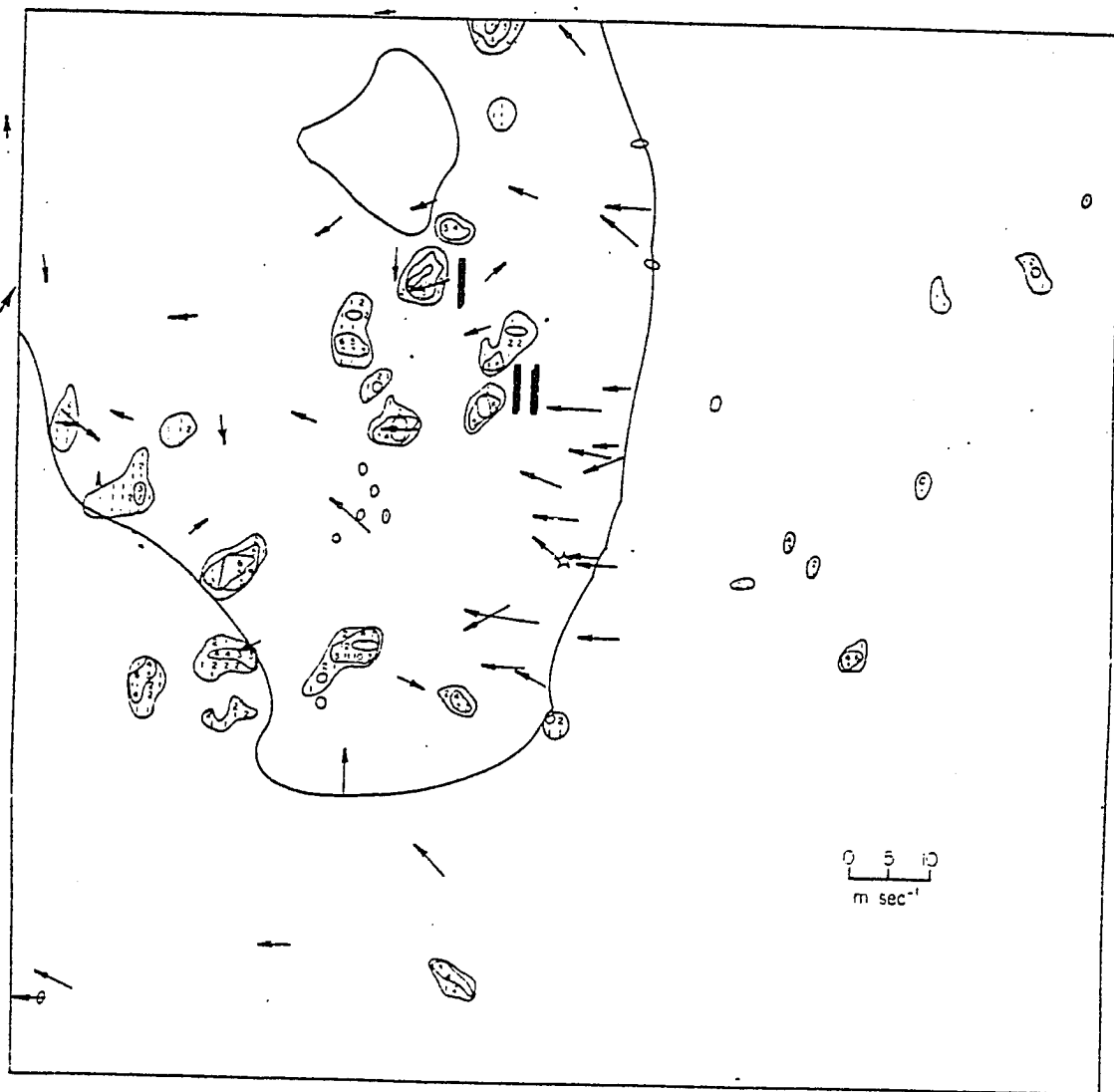
Figure 49. Radar echoes observed by the Miami radar at 1400 LST on July 17, 1973. Rainfall contour intervals are the same as in Figure 48.
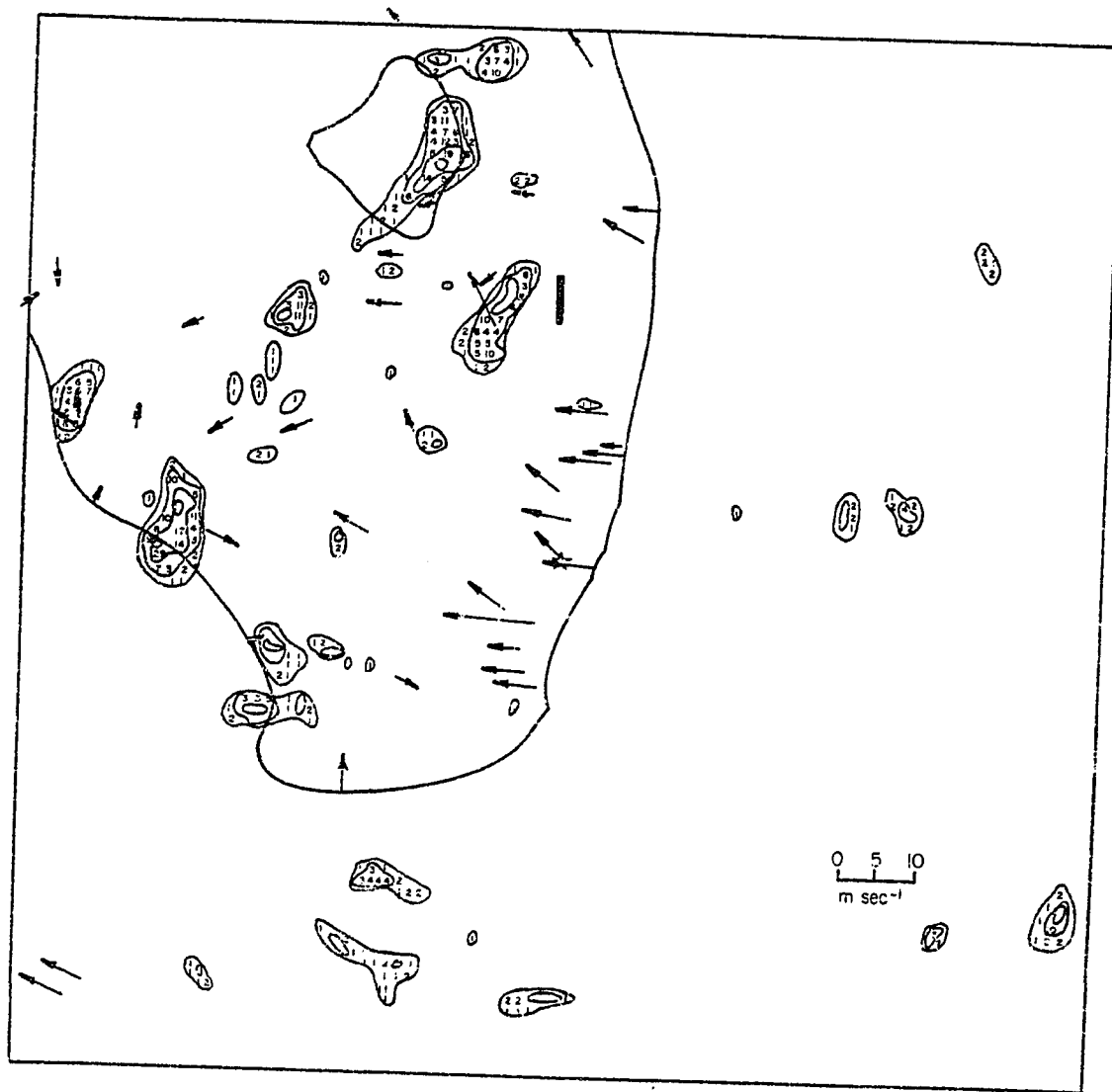
Simpson et al. (1979) observed that cirrus outflow from thunderstorms was extensive on July 17, covering much of the peninsula to the south of Lake Okeechobee. Convective activity in this region was apparently subdued by the presence of cirrus, in support of Gannon's findings, and by 1600 LST this activity had ceased. Pielke and Mahrer (1978) showed for a different summer day (July 1, 1973) that the model predicts sea breeze-generated moisture convergence to persist longer than the observed showers, a result which may be due to the omission of cirrus and the subsequent shading of the ground. This disparity between prediction and observation also occurs on this day along the southwest coast of the peninsula.

Nevertheless, Simpson et al. showed that the location of convergence zones (i.e. areas of mesoscale ascent), which were predicted using an earlier version of the University of Virginia Mesoscale Model (Mahrer and Pielke, 1977), were very well correlated with the locations of observed radar echo mergers, despite the neglect of cirrus shading in the model. The results of Runs A and C agree comparably well with those mergers, although Run B (moist, heterogeneous soils) does not.

In the simulation with the homogeneous surface, convergence wrapped around the eastern shore of the lake. A predicted peak vertical velocity of 4 cm/sec on the eastern shore weakened after local noon as the convergence split and moved around the lake.

In Runs B and C local convergence developed near cool sandy loam soil on the northern shore and to the southeast

of Lake Okeechobee. At a height of 1.2 kilometers the cell to the southeast indicated a peak upward velocity of about 6 cm/sec at 1215 LST for Run B and 4.7 cm/sec for Run C. Radar coverage in Figure 48 suggests a very general agreement of this cell with observed echoes I and II. The cell agrees a little better with echo I in Figure 49. It is important to note that the predicted cell developed solely because of a local change in surface description. Run A was featureless in the same vicinity, with vertical velocities approaching 1 cm/sec.

The convergence on the northern shore resulted from the combined influence of the lake and the moist soil. The predicted vertical velocity was greater than for the other cell, reaching 12 cm/sec for Run B and 7.2 cm/sec for Run C. These maxima occurred near 1300 LST. An echo was observed to form near the predicted convergence by 1400 LST.

A convective cell which developed by 1400 LST on the eastern shore of Lake Okeechobee was not handled well by any of these simulations.

It is probable that subgrid-scale inhomogeneities gave rise to the individual convective cells. However, areas of preferred local convergence did develop on the resolvable scales in these simulations. Cotton and Pielke (1977) computed grid-averaged vertical velocities from data sampled at 1.2 km for July 17. They noted a large variance and attributed it to cumulus effects. The results of Runs B and C give rise to the speculation that much of the variance may

be due to surface inhomogeneities. However, it is acknow-
ledged that the effects of cirrus may overwhelm surface
forcing.

Sea breeze development, judged by the intensity of the
convergence, was most intense by 1815 LST. Figures 50
through 52 indicate that sea breeze penetration was greatest
near the convex bulge in the west coast, reaching about
35 km inland for the homogeneous sand and 30 km for Run C.
Inland penetration of the sea breeze was much less over the
moist coastal soils in Run B. Maximum inflow of sea air
over sand to the north in that simulation reached about 13
km.

Intensification of the sea breeze trough along the west
coast accelerated the air at low levels over most of the
western peninsula. Windspeeds over the southern peninsula
in B were relatively unaffected, although the winds veered
toward the well-developed convergence to the northwest.

Onshore flow crossed the western coastline at a large
angle and it accelerated significantly in the vicinity of
the most intense convergence. Winds which earlier diverged
widely over Lake Okeechobee now blew straight across,
responding to the intensified downstream pressure gradient
and the reduced thermal contrast with respect to the land.

Airflow downwind of the lake was still divergent, much
as it was earlier in the afternoon. Notice that the cooler
soils in Run B still prevented a southwestward deflection of
winds off of the lake (Figure 51). This suggests that the

Figure 50 . Same as Figure 45 , except the time is 1815 LST. Contour interval for the vertical velocities is 5 cm/sec.
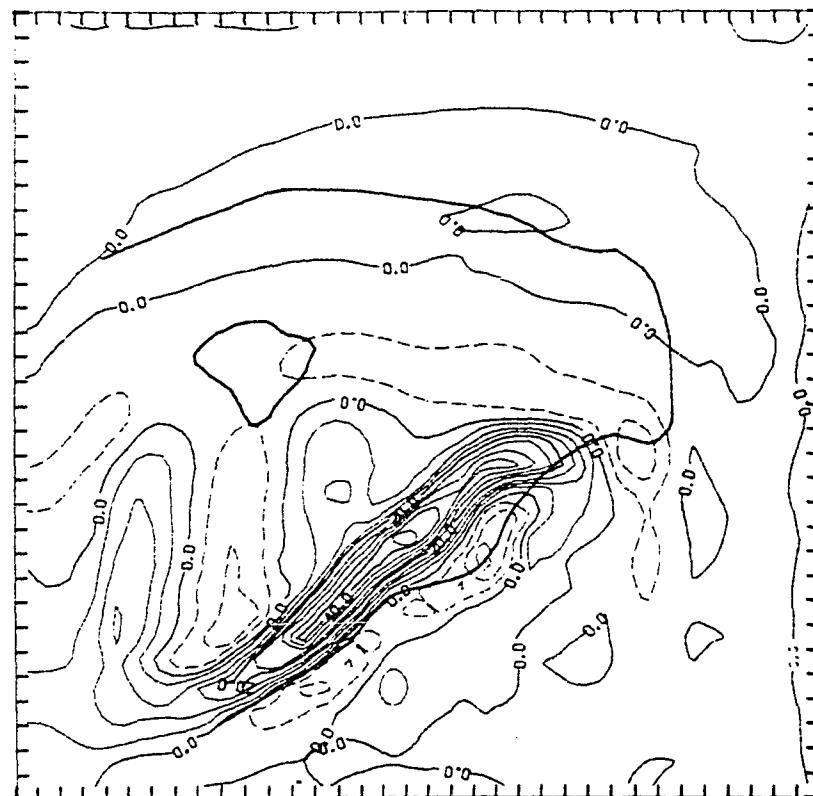
b.
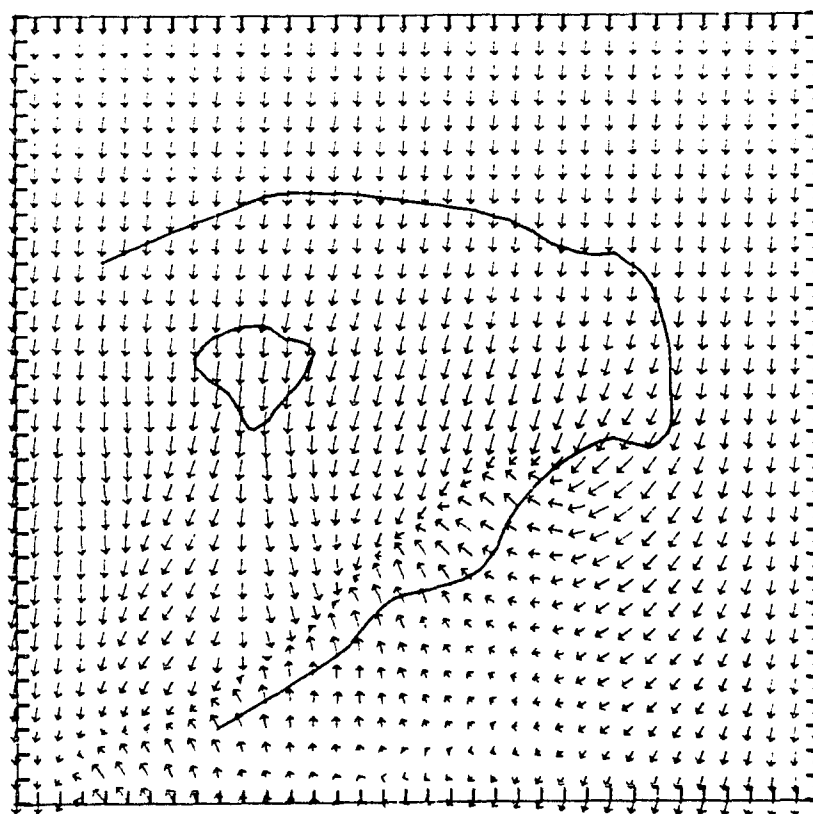
a.

Figure 51. Same as Figure 46 , except the time is 1815 LST. Contour interval for the vertical velocities is 5 cm/sec.
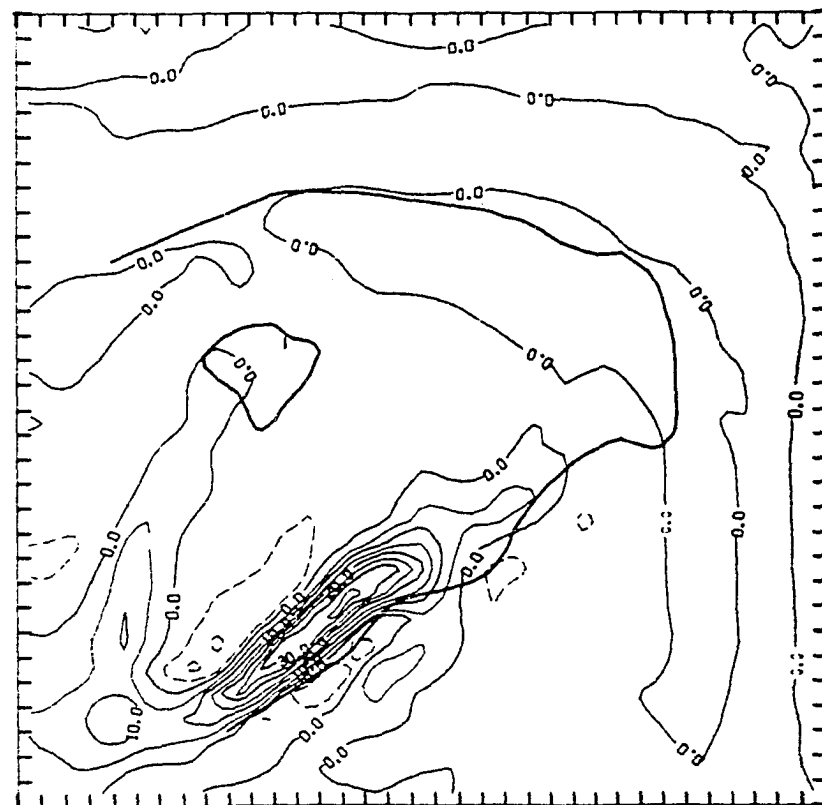
b.
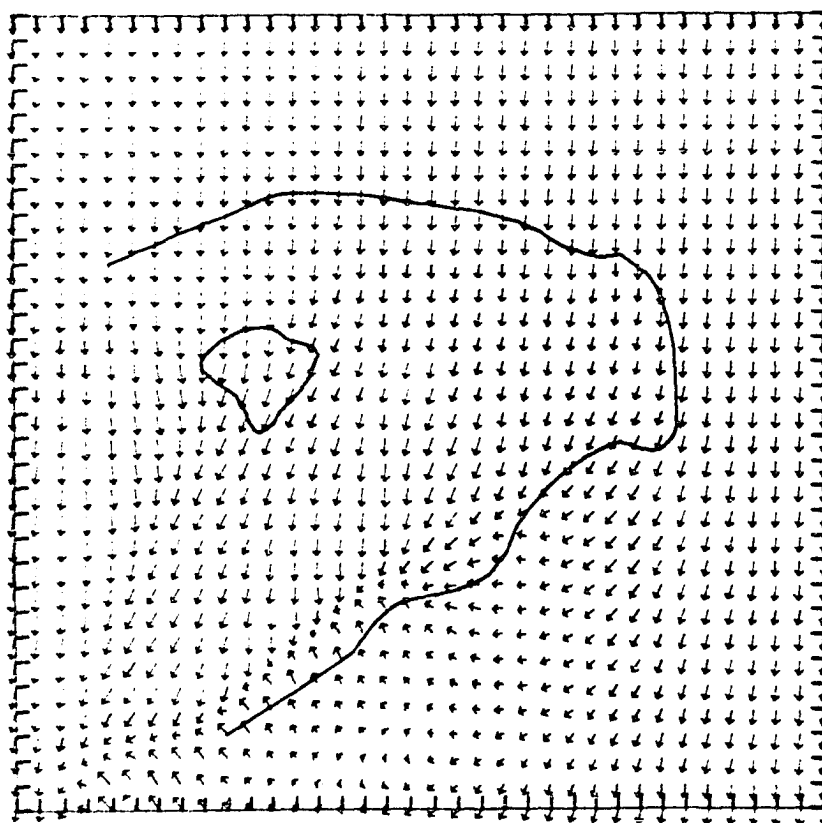
a.

Figure 52 . Same as Figure 47, except the time is 1815 LST.

Contour interval for the vertical velocities is

5 cm/sec.

b.

a.
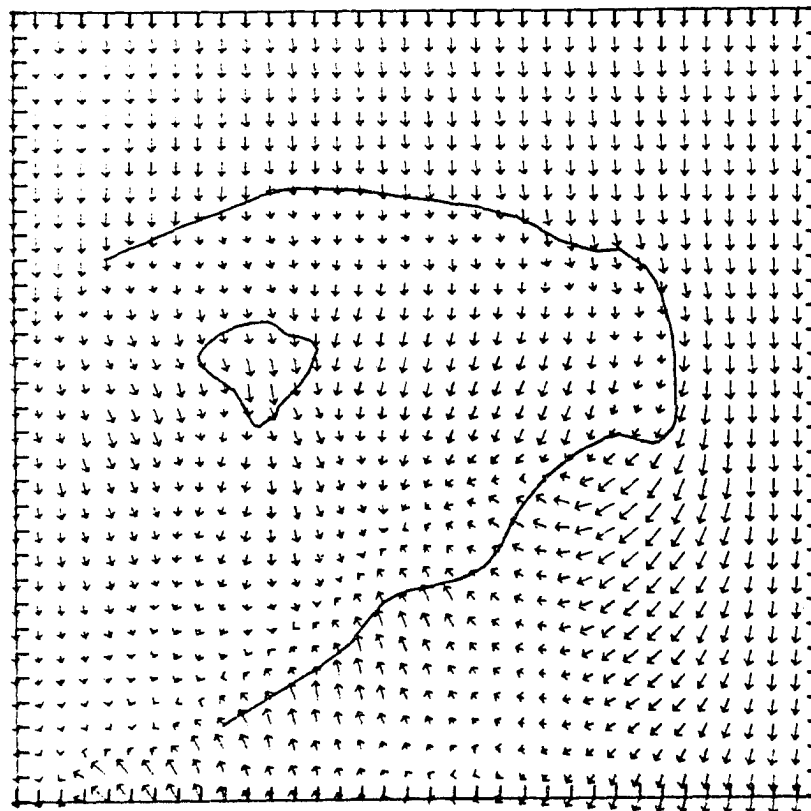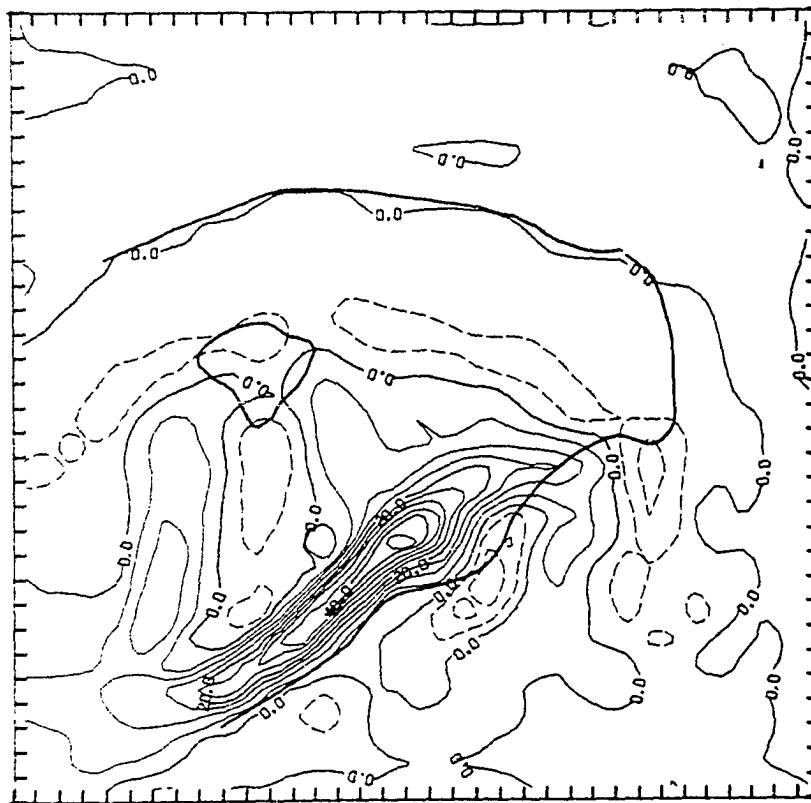
divergence is largely regulated by the lake breeze coupled with the diffluent curvature of the western lakeshore.

Convergence appeared in corridors where the deflected air intercepted the main airstream. Vertical velocities up to 16 cm/sec were predicted in the northern corridor, while they were about 40% less to the south. Ascent was greatest near the sea coast. The most intense development of the sea breeze was still limited to the north shore by the bare moist soils. However, the vegetation generated a sea breeze nearly as extensive as the bare sand of Run A. The peak upward velocity in the former was slightly higher (51 cm/sec vs. 47 cm/sec), but it occurred in about the same location. Generally the convergence in Run C was slightly weaker, indicative of less sensible heat availability in the lower half of south Florida.

The observed shower activity along the eastern shore of Lake Okeechobee was most intense between 1500 and 1600 LST. Then it rapidly decayed and regenerated by 1700 LST just to the south of the lake. Neither of the simulations which parameterized bare soil captured this activity. In Run C the cell located initially to the southeast moved westward along the southern shore, but the convergence was weak and quite diffuse. Thus it did not correlate well with observations. The stronger convergence around the lake was maintained along the northern or northwestern shore in Runs B and C. However, this area became echo-free by 1600 LST.

Shower activity was negligible in the southern peninsula

where cirrus overcast shaded the ground. It is perhaps worth mentioning that even though the effect of cirrus clouds was not incorporated in the model, convergence was not predicted over most of the southern peninsula late in the afternoon in any of the simulations.

B.   Experiments with Condensation

In numerical models, condensation is usually treated on two different scales: the resolvable scale (as defined by the grid points), and the subgrid scale, which incorporates the effects due to ensembles of individual cumuli. On the resolvable scale, latent heat is released explicitly by removing any supersaturation which occurs at each time step. The condensate which results is then eliminated either very simply (Hsu (1979); Shuman and Hovermale (1968)) or it is subjected to a bulk microphysical parameterization (Bhumralkar (1972); Rosenthal (1978)).

Cumulus parameterizations are treated less directly, relying upon statistical descriptions of the effects of cumulus populations on the larger scales. Recently, Rosenthal (1978) questioned the necessity for cumulus parameterizations, especially in models which simulate smaller scales, such as the mesoscale. He attributed early failures to simulate hurricanes (which led to the apparent necessity for cumulus parameterization) to the absence of a large scale circulation which could organize and control small scale instabilities. He also noted that those simulations were terminated prematurely before non-linear effects could act to balance convective growth. Furthermore, the environmental soundings used to initialize the models permitted a rapid amplification of small-scale instabilities.

Using a numerical model, Rosenthal demonstrated that explicit treatment of convective elements on the resolvable

scale led to a reasonable simulation of tropical storm evolution. His model was hydrostatic and axisymmetric and it employed a horizontal grid increment of 20 km. Notably, Rosenthal's simulation did not suffer from the numerical difficulties of the early hurricane models.

The condensation parameterization described in section III.C. was applied directly to the resolvable scale in the present model without resorting to subgrid scale parameterizations. Preliminary results in two and three dimensions revealed that rainfall did not reach the ground in the south Florida simulations. In fact, only one or two vertical levels were ever saturated. It was felt that the inability of the model to generate rain at the surface was attributable to two causes. First, the grid box area (121 km^2) is large relative to the average size of individual cumulonimbi (the primary precipitation mechanism). Secondly, and most importantly, cloud microphysics were not treated. This meant that the restraint imposed by the method of partitioning condensed water vapor below predicted cloud base was too severe, precluding rainfall.

It was desirable to keep the condensation parameterization simple. Therefore, in lieu of an explicit microphysical parameterization, the moisture excess was computed from III.C.4,

$$q' = q - \delta\, q_s\, (T) \; ,$$

where $\delta < 1.0$. In this way, convection was crudely parameterized by assuming that once the grid volume relative

humidity exceeded δ, someplace within the grid box was saturated. All other aspects of the condensation scheme remained unchanged.

Three values of δ were tested: 0.95, 0.90 and 0.85. In two dimensions little useful information was obtained since the coastal convergence was weak (cloudiness and its effects upon surface heating were permitted). Simulations in three dimensions indicated that rain still failed to reach the surface when δ = 0.95. But it did reach the ground when δ = 0.90 and δ = 0.85. Rain was heaviest and most wide-spread for the latter value, but convergence over most of south Florida appeared to be too weak during the afternoon. Therefore, δ was arbitrarily set equal to 0.90 in the moist experiments which follow.

Shuman and Hovermale (1968) introduced a similar tech-nique for an NMC operational primitive equation model which they applied to the synoptic scale. Their testing indicated that δ = 0.80 gave useful rainfall predictions. In their model, latent heating was distributed above the boundary layer in proportion to the vertical moisture distribution.

Experiments B and C were rerun permitting cloud cover and rain. They are referred to as Runs D and E, respectively.

Departures from Run B were first evident in Run D by 1115 LST with the onset of cloudiness. Low cloud formed at 950 meters in a large band which paralleled the east coast. Its predicted width was a few tens of kilometers to the north of Lake Okeechobee, but it expanded to about 120

kilometers south of the lake encompassing much of the lower peninsula. At this time predicted rainfall was very light, occurring only to the south of the lake. Figure 53 is a satellite photograph taken at 1237 LST. Notice that two convective cells are prominent just south and southeast of the lake. The model predicted rainfall of 0.9 mm near the southeast cell and 0.2 mm near the southern cell for the hour ending at 1215 LST.

Rain was also predicted just offshore and about a grid point north of the isolated cloud shown along the southwest coast. The most substantial precipitation fell in the vicinity of the large cloud mass situated near the southern tip of Florida. Predicted rain fell over an area of approximately 2400 km^2 with a maximum accumulation of 1.5 mm during the hour ending at 1215 LST.

East coast winds in Run D accelerated by late morning due to superimposition of the sea breeze inflow upon the synoptic current (Figure 54). Subsidence, which resulted over the coastline, was strongest at predicted cloud base height (950 meters). Air over the east coast dried about 0.5 g/kg below the maritime air and 3.5 g/kg below the air over the moist soil to the west. During the course of the afternoon dry air was advected westward causing the cloud deck to dissipate. By 1715 LST clouds were aligned with the mesoscale convergence along the western shoreline and to the northwest of Lake Okeechobee as seen in Figure 55 . Another large cloud deck lay to the west of the peat situated south

Figure 53. A DAPP (Data Acquisition and Processing Program) satellite photograph of south Florida taken at 1237 LST on July 17, 1973.

Figure 54. a. Predicted horizontal winds at 25 meters for Run D

(mixed soils). Wind speed is proportional to arrow

length with one grid interval equal to 8 m/sec. b.

Predicted vertical velocity at 1200 meters. Contour

interval is 4 cm/sec. Dashed lines indicate negative

velocities. Time is 1115 LST.

b.

a.

Figure 55. Predicted cloud cover at 1715 LST (composited from all levels) for Run D.

JULY 17, 1973
1715 LST
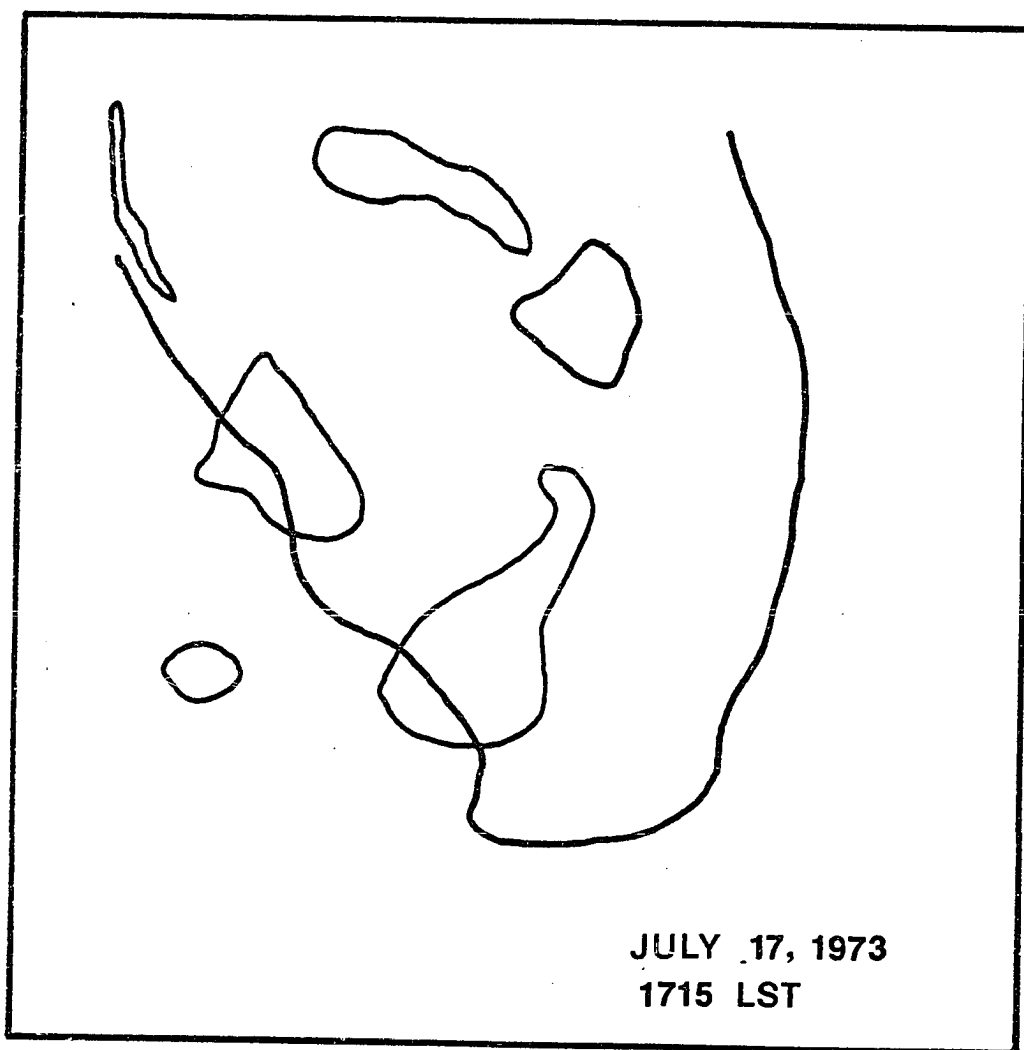
of the lake.

Tables VI and VII demonstrate the importance of both cloud and light rain on the model predictions. The onset of cloudy skies cooled ground surface temperatures quickly by several degrees. Air temperatures fell by less than one degree in the first hour and the relative humidity increased. When light rain reached the ground, the surface was cooled an additional 4.6°C. Evaporation of rainwater chilled the air another degree and saturated it.

Over sand, the clouds dissipated after two hours. The surface temperature recovered close to the clear sky value. On the other hand, the temperature of the sandy clay surface warmed by only 2°C after the shower had ceased. Overcast skies depressed the soil and air temperatures several degrees below the clear sky temperatures until late afternoon.

Between 1815 and 1915 LST the sky cleared over the clay. Surprisingly the surface temperature dropped 3.3°C, lower in Run D than in Run B, even though the air temperature and the specific humidity were about the same for each simulation. Apparently the discrepancy in behavior was a consequence of a weaker deep soil heat reservoir which was needed to sustain a higher surface temperature.

Afternoon cloudiness along the upper west coast of Florida reduced coastal soil temperatures by 3 - 6°C with respect to Run B. Since this reduced the sharpness of the temperature gradient, the maximum strength of the sea breeze convergence was diminished by 25% at 1815 LST (Figure 56).

Table VI . Effect of limited cloud cover on soil and atmospheric

parameters for a gridpoint with sandy soil (13,17).

Atmospheric variables are evaluated at a height of

37.5 meters.

RUN D   RUN B

Hour (LST)	$T_G(^\circ C)$	$T(^\circ C)$	$q(g/kg)$	$h(\%)$	Sky	$T_G(^\circ C)$	$T(^\circ C)$	$q(g/kg)$	$h(\%)$
1015	40.6	30.2	18.3	77	Clear	40.6	30.2	18.3	77
1115	36.9	29.8	18.6	80	Cloudy	43.2	30.9	18.3	66
1215	37.4	29.7	18.9	82	Cloudy	44.6	31.6	18.1	63
1315	43.5	31.2	18.3	73	Clear	44.7	32.3	17.6	59
1415	42.7	31.8	17.8	68	Clear	43.8	32.6	17.4	58
1515	40.6	31.9	17.5	67	Clear	41.7	32.7	17.4	57
1615	37.5	31.6	17.7	69	Clear	38.5	32.5	17.4	58
1715	33.5	31.0	18.0	72	Clear	34.5	32.1	17.7	60
1815	30.1	30.1	18.8	80	Clear	30.9	31.1	18.8	75
1915	26.2	28.4	19.4	91	Clear	27.0	29.4	19.3	86

Table VII. Effect of cloud cover and rain on soil and atmos-
pheric parameters for a gridpoint with sandy clay
soil (17,17). Atmospheric variables are evaluated
at a height of 37.5 meters. Hourly rainfall (mm)
is noted in parentheses under sky condition.

RUN B

Hour (LST)	T_G(°C)	T(°C)	q(g/kg)	h(%)	Sky	T_G(°C)	T(°C)	q(g/kg)	h(%)
1015	34.5	29.6	19.8	86	Clear	34.5	29.6	19.8	86
1115	32.3	29.8	19.5	84	Cloudy	35.7	30.3	19.5	74
1215	32.1	28.7	19.8	97	Cloudy	36.4	30.7	19.6	72
1315	27.5	27.6	20.2	100	Cloudy (.12)	36.6	31.1	19.8	71
1415	29.5	28.5	20.0	97	Cloudy (.22)	36.0	31.4	19.6	70
1515	29.6	28.7	20.0	93	Cloudy	34.7	31.3	19.3	68
1615	29.5	29.1	19.8	89	Cloudy	32.7	31.1	19.1	69
1715	29.8	29.8	19.7	85	Cloudy	30.4	30.7	19.4	72
1815	29.4	29.8	20.1	87	Cloudy	28.4	29.8	20.0	86
1915	26.1	28.7	20.2	93	Clear	26.3	28.7	20.3	93

RUN D

Figure 56. Same as Figure 54, except at 1815 LST. Contour interval in b. is 10 cm/sec.

b.
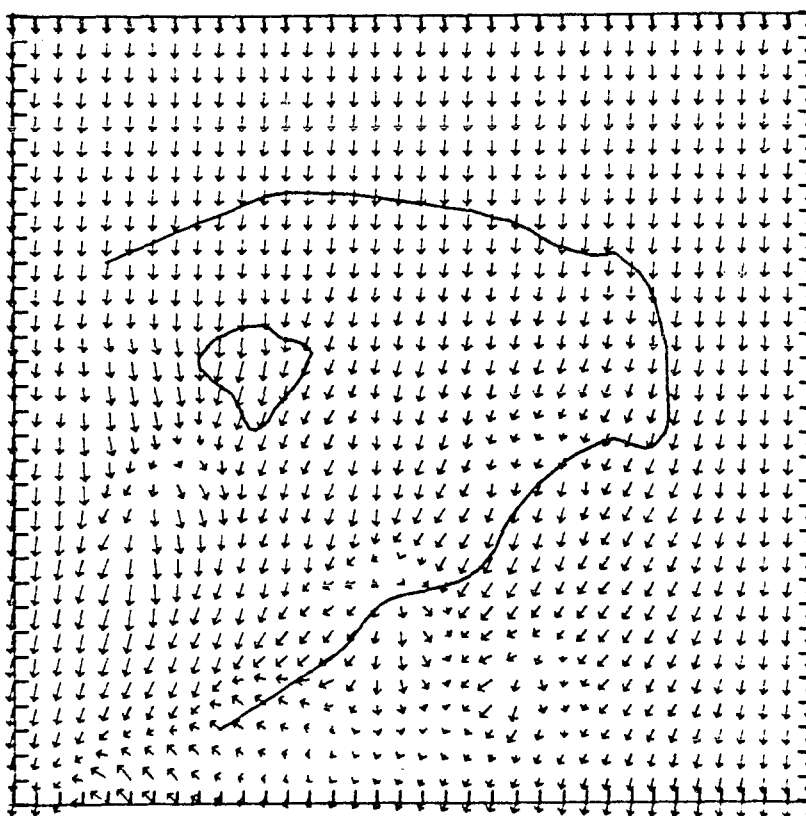
a.

Local cooling due to cloud cover abbreviated the region of strongest convergence at 1.2 km (w > 10 cm/sec), preserving only the northernmost ninety kilometer segment. Interestingly the strength of this convergence was comparable to Run B.

Just inland along the indentation in the lower west coast rain and cloud formed by 1115 LST. Weak sea breeze convergence, enhanced by the release of latent heat, created a precipitating disturbance which later proceeded westward across the Gulf of Mexico. This "storm" will be evaluated in future research.

Sea breeze convergence was stronger in Run E than in Run D since vegetation enhanced the sensible heat flux to the atmosphere. By 1515 LST (Figure 57) the primary convergence zone had advanced 40 - 60 kilometers inland from the west coast. Two hours later it was centered up to 90 kilometers inland. This was three times the penetration which occurred when clouds were absent (compare Figures 52 and 58).

Predicted cloud cover (which in this model is indistinguishable from rainfall aloft) at 1715 LST, depicted in Figure 59, indicates that the strongest sea breeze convergence was essentially contoured by the inland edge of the clouds. The radar map at 1700 LST in Figure 60 suggests that there may be some relationship between the predicted cloudiness and observed echoes along the coast. The echoes to the south of Lake Okeechobee may well be a response to the cirrus over the southern peninsula. Cirrus was not treated by the model.

Figure 57 . a. Predicted horizontal winds at 25 meters for Run E.
Wind speed is proportional to arrow length with one
grid interval equal to 8 m/sec. b. Predicted vertical
velocity at 1200 meters. Contour interval is 5 cm/sec.
Dashed lines indicate negative velocities. Time is
1515 LST.

b.

a.

216
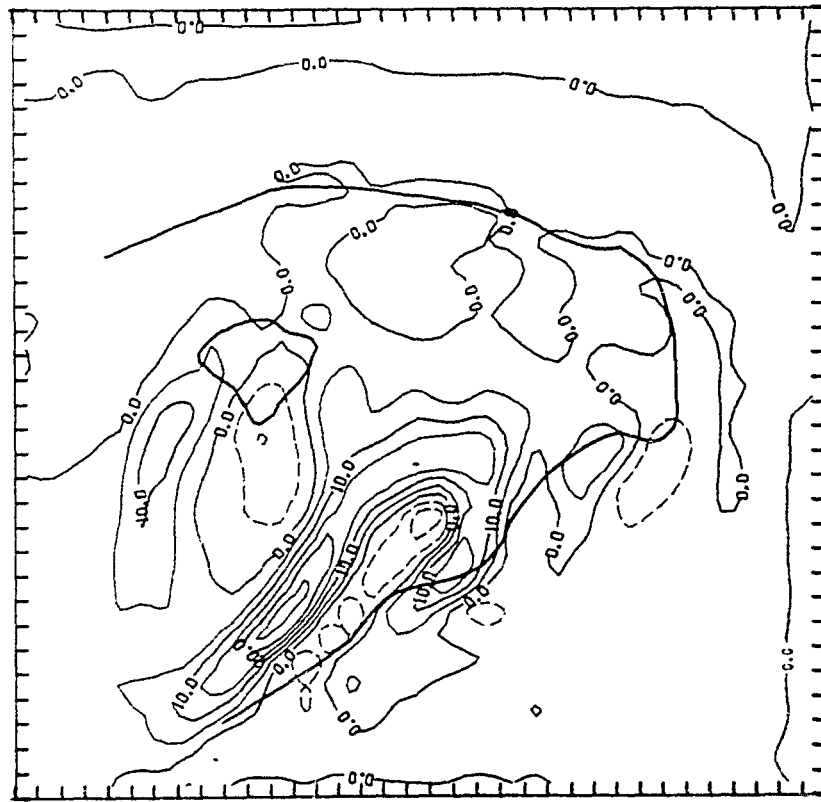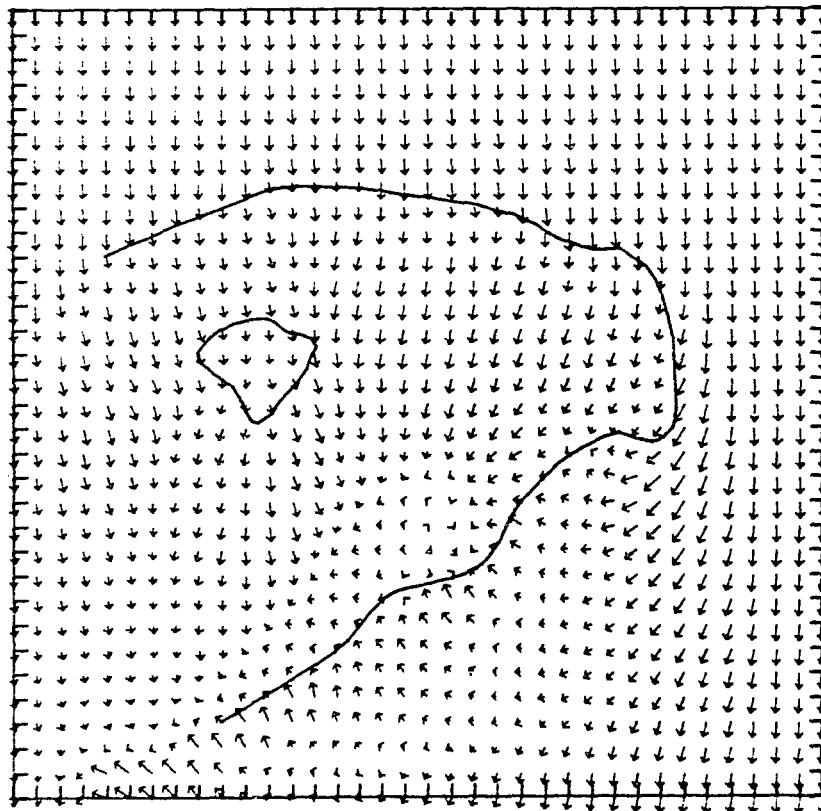
Figure 58. Same as Figure 57, except the time is 1715 LST.
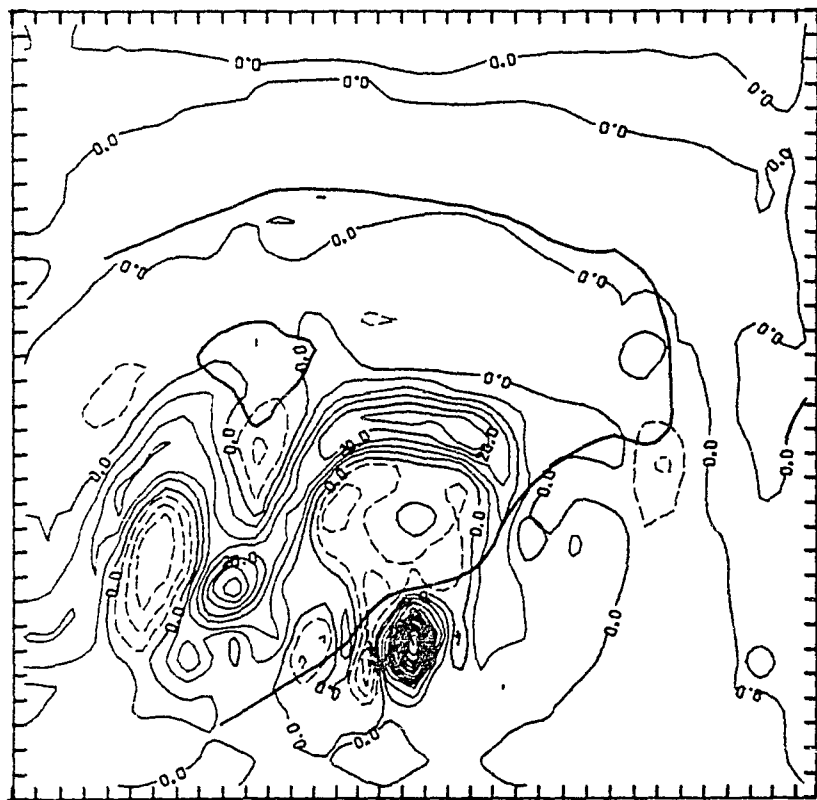
b.
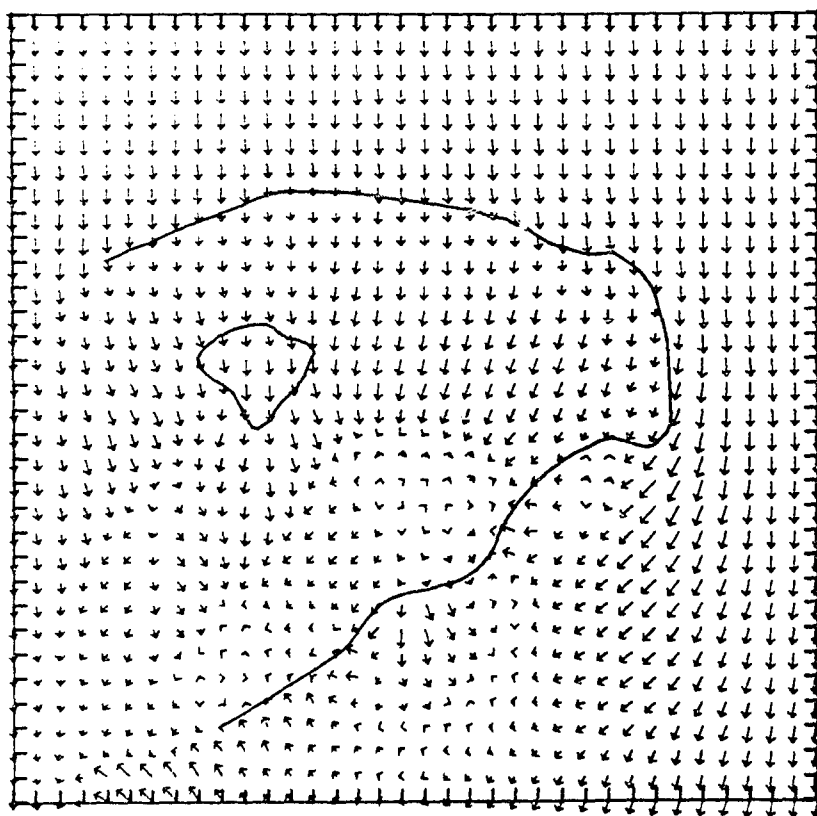
a.

Figure 59. Predicted cloud cover at 1715 LST (composited from all levels) for Run E.

JULY 17, 1973
1715 LST
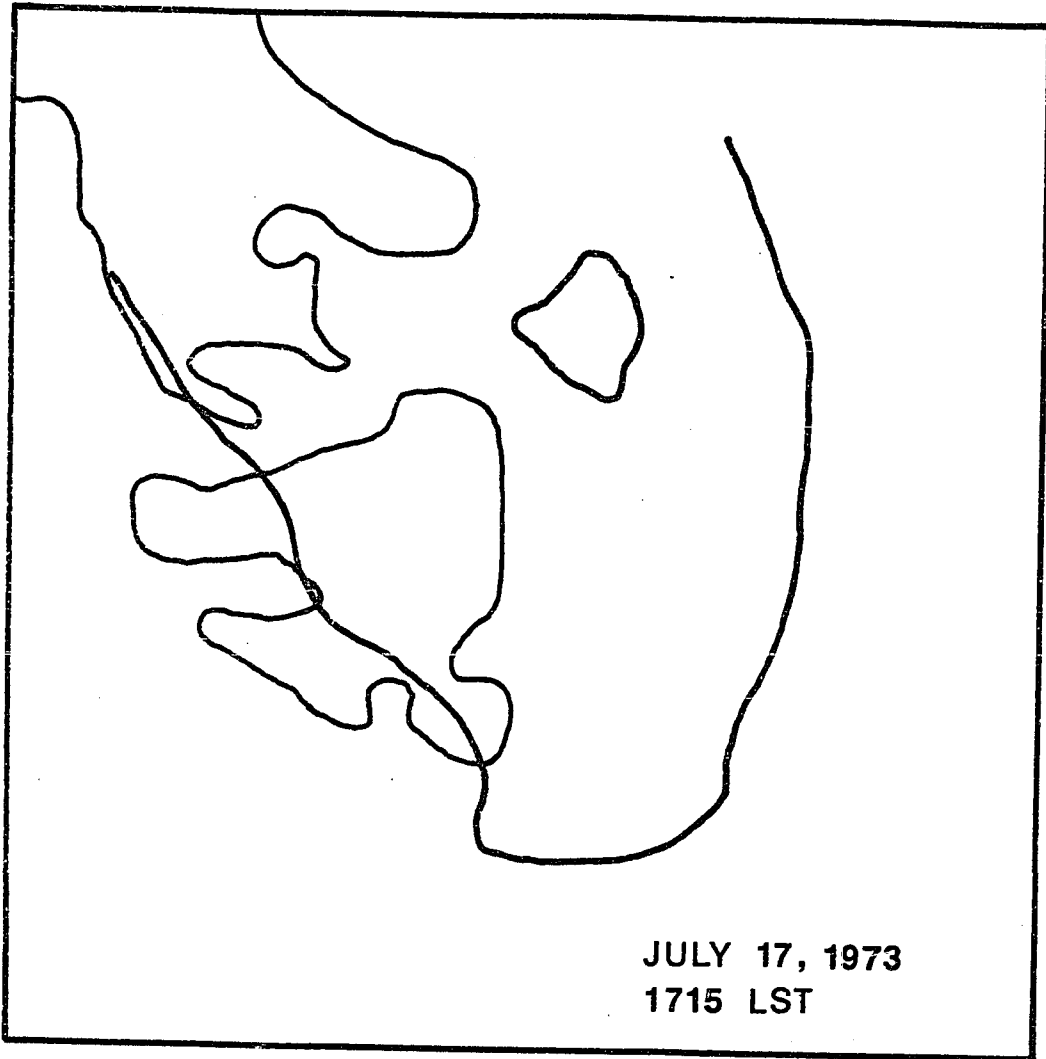
Figure 60 .   Shower pattern observed by the Miami radar at 1700

LST on July 17, 1973.   Rainfall rates are contoured

as noted in Figure 48 .

The predicted cloudiness over bare soils in Figure 55 agrees
even less with observed radar echoes.

A large precipitating cell developed along the middle
of the west coast, within the cloud deck. By 1815 LST the
circulation of the storm was questionable since the updraft
core intercepted the top of the model.

Convergent cells which developed on the north shore
and to the southeast of Lake Okeechobee in the early after-
noon in Runs B and C also appeared in both of the simulations
with clouds and rain. Neither the location nor the inten-
sity of these cells appeared significantly altered by the
presence of light rain or cloud.

C. Summary

Simulations in three dimensions showed that sea breeze organization was regulated by the transfer of sensible heat from the surface to the atmosphere. Gannon also determined that sensible heat flux was the most important forcing controlling sea breeze intensification in his two dimensional experiments. He noted that lower albedos and drier soil enhanced sensible fluxes, which is consistent with the results in section VI.

Uniform dry soil produced the most extensive and intense sea breeze since a large temperature contrast relative to the sea air had developed through a deep layer in the atmosphere near the coast. Moist soils which were up to 10°C cooler than dry sand inhibited strong sea breeze development. Similarly Carpenter (1978) showed, using a uniform surface, that a sea breeze under southeasterly geostrophic flow penetrated 20 km further inland when the resistance to evaporation was higher.

Vegetation decreased moisture fluxes over peat and marsh, from which soil water evaporated at the potential rate. At the same time the foliage increased the flux of sensible heat to the atmosphere. This helped to create a circulation which was intermediate in both intensity and extent between the uniform and variable bare soils. Where the coastal soils were wettest, the development of the circulation in Run C lagged the predicted circulation in Run A by one to two hours through late afternoon.

The simulation in which the soil surface was assumed homogeneous (Run A) predicted divergent airflow near Lake Okeechobee. Otherwise the inland airflow was featureless. For heterogeneous surfaces local convergence also developed to the north and the southeast of the lake, where the soil temperature contrast was large. Since strong temperature perturbations were confined to a shallow layer, the convergence was weak.

Cloudiness which formed along the west coast diminished sea breeze intensity by reducing the horizontal temperature gradient. The convergence moved inland and re-established itself just to the east of the clouds.

VIII. <u>Conclusions</u>

A. A Review

A numerical model was developed to examine the impact of surface sensible and latent heat fluxes upon the organization and the strength of a south Florida sea breeze. The basic model was that of Pielke (1974), with the revisions reported in Mahrer and Pielke (1977). Three principal modifications were performed in this research. They included a more complete and detailed description of the soil layer, a provision for bulk parameterization of the energetic and aerodynamic effects of vegetation and a simple, explicit treatment of condensation.

The soil layer was staggered over 14 levels to a depth of one meter. This offered high resolution near the surface, where heat and moisture gradients are most intense during the day, and low resolution below the depth of the diurnal temperature wave. Using data from Clapp and Hornberger (1978) and Rijtema (1970) a table of values for several variables was constructed for eleven different soil textures in addition to peat. The model was then constructed so that these soils could be arbitrarily intermixed, one to each grid box. This permitted studies of heterogeneous ground surfaces.

Deardorff's (1978) one-level vegetation parameterization was extended to three dimensions by mapping foliage as an array in a manner similar to the treatment of the soils. His equations were re-configured so that the vegetative fluxes

could be used with the more sophisticated treatment of bare
soil fluxes in the Pielke model. A provision was made for
two types of canopies for the south Florida simulations,
each being uniquely described by several generalized
variables (they were generalized because sampled data was
not available for vegetation).

Precipitation was predicted explicitly. Excess moisture
was removed and condensed using the procedure outlined by
Asai (1965). When an unsaturated layer was encountered
rainfall evaporated until the layer saturated. Saturation
was not imposed upon the air just above the surface.

Radiative transfer between the atmosphere and the
ground was modified to take account of predicted cloudiness.
It is important to note that this model makes no distinction
between cloud water and rain water. Upon the inception of
condensation, cloud and rain appeared simultaneously. Solar
insolation was diminished via a transmission function
(Atwater, 1973) which was applied layer by layer in a
multiplicative fashion. In the absence of cloud, no
reduction of the flux occurred in a layer.

Sasamori's (1972) simplification of long wave radiative
transfer was extended to account for a single cloud deck,
although the depth was variable. Both the upper and lower
surfaces of a cloud were assumed to radiate as black bodies.

One-dimensional sensitivity tests were conducted to
evaluate the parameterizations of the soil and the foliage
canopies. Three single-level slab schemes for predicting

soil moisture were compared against the layered soil of the
present model. With the layered soil taken as the control,
it was shown that none of the slab approximations correctly
predicted soil moisture. Discrepancies in predicted soil
moisture content resulted in deviations in the sensible
heat flux as large as 30%. Even larger departures occurred
for the magnitude of the latent heat flux and the shape of
its diurnal curve varied markedly. The type of slab
technique chosen strongly affected the outcome. Therefore,
if a slab parameterization is used, the results can be
considered firmly reliable only if they are checked against
sampled soil data. This especially applies to atmospheric
simulations which permit condensation, since they use the
latent energy released from the soil.

Testing also revealed that:

a. The initial profile of soil temperature is
   inconsequential when a simulation commences at
   sunrise, provided the sky is clear. This result
   may not apply should a run commence during the night.

b. Initial soil moisture conditions mandate the outcome
   of a simulation. This applies to both the initial
   surface moisture content and to the vertical
   moisture profile within the soil. The moisture
   conductivity, a function of soil moisture, regulates
   delivery of soil moisture from a deep supply to the
   surface. The relative humidity of the soil surface
   is strongly affected by the wetness (through the

moisture potential). This humidity is the important variable which determines how energy, which is available for export to the atmosphere, is partitioned as latent and sensible heat. The immense control exerted by the wetness of the soil, as demonstrated by the experiments presented in this research, make clear the necessity to acquire sampled soil data suitable for initializing a numerical model! The results of the three-dimensional simulations presented here are surely strongly dependent on the estimates for soil moisture which were used in lieu of non-existent observed data.

c. The surface albedo was secondary in importance to the soil moisture content, although its magnitude was dependent on the wetness of the surface. Soil type was apparently not a very significant factor.

d. Moist soil was characterized by a lower midday peak temperature and a smaller diurnal range than dry soil. When soils evaporated moisture very near the potential rate, latent heat fluxes tended to be very large. This is reasonable for a clear July day in south Florida. When the soil was sufficiently dry, the relative humidity dropped so low (< 30%) that it caused the latent heat flux to peak two hours ahead of the sensible heat flux.

e. Vegetation replaced the ground surface as the principal source of sensible heat. Over wet soils

this flux increased nearly 200%, while the latent

heat fluxes were reduced by up to a factor of two.

Some uncertainty in assigning weighting parameters

for q_{af} and T_{af} (canopy air specific humidity and

temperature, respectively) and in choosing a repre-

sentative resistance coefficient resulted in dis-

crepancies in heat fluxes on the order of 10% or less.

and f. Boundary layer growth over a forest was about 60%

greater than over bare soil in a one-dimensional

simulation (Figure 32). However, the relative dif-

ference was much less noticeable in a three-dimen-

sional simulation due to the dominance of mesoscale

circulations.

The three-dimensional simulations indicated an important

point--mesoscale circulations will develop where large

temperature contrasts occur, provided they do so over a

distance of at least a few grid points. Certainly this is

nothing new. Many other investigators (Pielke, 1974; Tapp

and White, 1976; Hsu, 1978; and others) showed that sea

and lake breeze circulations resulted when the thermal

contrast between land and water is large.

Conversely, in the present research sea breeze develop-

ment was curtailed by moist coastal soils, which offered

relatively weaker temperature gradients between land and sea.

But this work also indicated that the strength of the

mesoscale convergence was strongly linked to the depth of

the large thermal contrast. Along the west coast of Florida
the warm air amassed through a deep layer, culminating in
strong convergence. But local convergence to the north and
southeast of Lake Okeechobee, generated by local surface
inhomogeneities, was weak because the temperature perturba-
tion was shallow. Thus, advection enhanced the west coast
convergence, but it limited the intensity of local convergence
in the east. This is consistent with the findings of
Pearson (1973).

Sea breeze intensity was strongest where the upwind
heating was intense over a long fetch. Therefore, the
strongest circulation always occurred alongside regions of
extensive sand, since it was the driest soil modelled. In
Run B, which included moist bare soils, strong sea breeze
development was limited to the northern Gulf coast. But
when vegetation was added, much more sensible heat was made
available in the southern peninsula. In this case the
strongest circulation was nearly as extensive as Run A, in
which a homogeneous sand surface was assumed.

Simulated cloud cover cooled soil and air temperatures
during the day due to shading and raised them at night, as
it should. On the mesoscale, clouds reduced the temperature
contrast along the coast, thereby weakening sea breeze
convergence. Also, the convergence repositioned itself just
along the inland edge of the cloud deck. Rain, although
generally light, cooled air and soil temperatures even more
than did clouds. This agreed with Bhumralkar (1972), who

neglected cloud shading in his simulations because observations indicated that it was insignificant relative to evaporational cooling.

Cloud formation was more widespread and more persistent in Run B than in Run C due to the larger moisture fluxes to the atmosphere. In Run C clouds were mostly confined to the western half of the peninsula or the immediate vicinity of Lake Okeechobee. But in Run B, a predicted cloud coverage extended over much of the peninsula to the south of the lake. This coverage persisted until about mid-afternoon, when the surface heating coupled with advection of drier air from the east coast dissipated much of the deck. Test runs in two dimensions indicate that the greater cloudiness in Run B is due to a large increase in the surface moisture convergence. This results from a larger source of surface moisture and from less vertical turbulent mixing since the sensible heating is reduced. The test runs suggested that the moisture convergence could increase by more than 40% up to cloud base.

B.   Suggested Research

Some additional work is justified to better understand the surface parameterizations. For instance, the matrix of soils could be reduced to a single soil type, where the moisture content and surface albedo can be mapped as variable input. This should succeed since wetness and albedo account for nearly all of the variability between the soils which were tested. Such an approach would effect a savings in computer core storage!

Most modellers cannot or will not simulate layered soils because of the attendant computational cost. For their benefit, Deardorff's (1978) force-restore slab scheme for predicting soil moisture should be evaluated. Intuitively it appears to be the best slab approach available.

The best way to fine tune the vegetation parameterization is to attempt numerical replication of observed data. Deardorff (1978) adjusted his simulation using sampled data and he obtained a good correlation with his predictions. However, the results of this work suggest that some of Deardorff's coefficients may not be universally applicable. It is likely that the coefficients need to be re-evaluated on an ad hoc basis. Without sampled data, the parameterization is guided less by rigorous physics and more by instinct.

More work needs to be done to ascertain the role of local surface inhomogeneities in the generation of mesoscale circulations. A good example is the simulation of urban heat islands. In this case soil properties would be replaced with

those of the dominant urban substance (concrete, stone, etc.). Recent research strongly suggests that local rainfall is modified by urban influences (Huff and Vogel, 1978; Changnon et al., 1976). A numerical simulation could lend support to existing theories. This work could also be extended to study the effect of local circulations on the intensity and longevity of air pollution.

The present dependence of vegetative heat fluxes upon a constant transfer coefficient (C_G) is unsatisfactory. This formulation is only strictly valid for neutral stability. A more generally satisfying approach would be to define C_G as a function of the atmospheric stability, perhaps by using the Obukhov similarity functions which are applied to the bare soil. This would more formally generalize the parameterization.

An interesting experiment would be to simulate a locale as it exists today and compare that with either past or anticipated surface conditions. For example, some insight could be gained into the effect of cultivation and urbanization by the numerical restoration of native vegetation. Although detailed differences may not be reliably predicted owing to the complex interrelationship between soil and atmospheric variables, the gross trend may be shown.

Looking toward the future, a particular simulation for south Florida should prove interesting. A greater frequency of fires due to cultivation and its related flood control program in south Florida has caused a serious depletion of

rich peat soil. The impending total loss of the peat, with its low albedo and sometimes high water content, could have a large impact on the organization of the sea breeze and localized circulations. In addition, farmers have noticed that the frequency of frosts in orchards has risen dramatically from earlier in this century (Pielke, personal communication). Undoubtedly, this results from drier soil which occurs when water is impounded behind flood gates. Nixon and Hales (1975), using an airborne precision radiation thermometer (PRT) showed that wetter soils were warmer at night and the simulations reported here support their finding. It is possible that the results of a simulation without peat (exposing a limestone bedrock) could prove useful for the management of the Flood Control District of south Florida.

Experiments with moist processes should be explored further. In particular, the role of low level moisture convergence must be better understood in regard to the formation of clouds. Also the precipitation scheme must be improved. It is not economically feasible to use detailed sophisticated microphysics in this model, since the computer storage is already taxed heavily. However, a simple bulk approach such as that used by Rosenthal (1978) seems appropriate. The rain technique presently used is probably unnecessarily restrictive below cloud base for a mesoscale model, so that much surface rainfall is "lost". Cooling of the ground surface seems to be too little and it occurs later than it

should. On the other hand, the atmosphere below cloud base cools too much during the early hours of rainfall. Intuitively this must have a noticeable effect on mesoscale convergence.

It also seems appropriate that grid boxes should be permitted to contain fractional cloud cover, since the dominant cloud type (convective) has a typical area which is subgrid scale, at least prior to cloud maturity. In light of the anticipated vigor of precipitating systems in south Florida, the vertical dimension should be extended to at least 10 or 12 km.

The numerical model presented in this dissertation has been modified and extended to enhance its generality. A sound treatment of bare soils together with a reasonable parameterization of vegetation render this model ideally suited for a wide host of applications on the mesoscale.

APPENDIX A

List of Symbols

A (III.D)	root extraction term for soil moisture
A (IV.A)	generalized dependent variable in the Crank-Nicolson differencing scheme for diffusion
a	a constant (0.003286)
a_f	foliage albedo
a_G	total albedo of the ground surface
a_n	dependence of albedo on zenith angle
a_s	soil albedo (function of soil moisture)
a_w	empirical function for absorption of short wave radiation by water vapor
b	soil moisture exponent (function of USDA soil textural class)
c (III.B)	optical path length for carbon dioxide
c (III.D)	volumetric heat capacity of soil
c_f	non-dimensional transfer coefficient for foliage
c_G	non-dimensional transfer coefficient used to compute wind speed within a plant canopy and for energy fluxes computed beneath the canopy
c_i	dry soil volumetric heat capacity for soil type i
c_p	specific heat at constant pressure for dry air
c_s	soil specific heat
d	zero-plane displacement height for a plant canopy
D_η	diffusivity for soil moisture
D_{η_s}	saturation diffusivity for soil moisture

E_f	total moisture flux from foliage
e_s	saturation vapor pressure of air
E_{tr}	transpiration rate per unit area from foliage
E_0	moisture flux from the ground beneath a canopy
f	coriolis parameter
f'	fraction of potential evaporation from foliage
F_q	source/sink term for specific humidity
F_θ	source/sink term for potential temperature
F'_q	source term for specific humidity due to evaporation of rainwater
F'_θ	source term for potential temperature due to evaporation of rainwater
g	gravitational constant
G	soil heat flux
h (III.A)	depth of atmospheric surface layer
h (IV.B)	relative humidity of the soil surface
H	heat flux by conduction through the laminar boundary layer of a leaf
H_f	sensible heat flux from a canopy
H_s	vertical sensible heat flux within soil
H_0	sensible heat flux from the ground beneath a plant canopy
i	angle of incidence
I	thermal inertia
I_1	stability function used to compute friction velocity
I_2	stability function used to compute friction temperature and friction specific humidity
k	thermal conductivity of air

K	generalized exchange coefficient for Crank-Nicolson scheme
K_z^m	exchange coefficient for mass used for computing vertical diffusion
K_z^θ	exchange coefficient for potential temperature and specific humidity used to compute vertical diffusion
K_η	hydraulic conductivity
K_{η_s}	saturation hydraulic conductivity
k_o	von Karman's constant (0.35)
L	latent heat of vaporization
L_I	leaf area index
L_*	Monin-Obukhov mixing length
$L_*^\dagger$	mixing length weighted between bare soil and soil overlain by a plant canopy
M	solar optical path length used to compute transmissivity due to clouds
n	slope azimuth
P	atmospheric pressure (unscaled)
P_f	base ten logarithm of the magnitude of the soil moisture potential
P_G	precipitation rate at the ground surface
P_r	precipitation rate at the first atmospheric level
P_{TOP}	atmospheric pressure at the top of the model atmosphere
P_o	surface atmospheric pressure
q	atmospheric specific humidity
q_{af}	specific humidity of the air within a canopy
q_f	foliage specific humidity

q_G	soil surface specific humidity
q_s	saturation specific humidity
$q\vert_s$	specific humidity on the material surface
q_*	friction specific humidity
q'	moisture excess
$q_*^{\dagger}$	friction specific humidity weighted between bare soil and soil overlain by a plant canopy
$\tilde{q}$	partially updated specific humidity
r (III.B)	optical path length for solar radiation
r (III.D)	depth of the root zone
r_a	resistance of the air
r_s	stomatal resistance
R (II)	gas constant for dry air
R (III.D)	root distribution function for vertical profile
RAY	empirical function for forward Rayleigh scattering of solar radiation
R_L	longwave radiation
R_n	net radiation flux
R_{sw}	shortwave radiation
$(R_{sw})_0$	solar constant
$(R_{sw})_{MAX}$	maximum solar radiation for a clear sky
$(R_{sw})_{sl}$	shortwave radiation flux on a slant surface
S	material surface height
R_v	gas constant for water vapor
$\tilde{S}$	initial height of the material surface
S'	fraction of supersaturation which is condensate
t	time

T	free air temperature
T_{af}	air temperature within a plant canopy
T_f	foliage temperature
T_G	temperature of the ground surface
T_s	soil temperature
u	East – West component of velocity
u_{af}	windspeed within a plant canopy
U_g	East – West geostrophic wind component
u_*	friction velocity
$u_*^{\dagger}$	friction velocity weighted between bare soil and soil overlain by a plant canopy
v (II)	North – South component of velocity
v (VI.E)	free air speed just above the canopy
V_g	North – South geostrophic wind component
W_a	turbulent atmospheric moisture flux
W_I	maximum interception storage as a depth per unit leaf area
W_L	actual liquid water depth per unit leaf area
W_s	soil moisture flux
w^*	vertical velocity in the transformed coordinate system
w_*	convective velocity scale
x	East – West horizontal coordinate
y	North – South horizontal coordinate
z (II)	cartesian vertical coordinate
z (III.D)	vertical coordinate within the soil
Z (III.B)	zenith angle
z^*	transformed vertical coordinate in the atmosphere

z_G	height of topography
z_i	depth of the planetary boundary layer
z_0^*	turbulent roughness height in the transformed coordinate system
α	slope angle
β	solar azimuth
γ	solar hour angle
Γ_{TOP}	initial vertical gradient of potential temperature at the top of the model atmosphere
δ (I)	weighting function
δ (III.B)	solar declination
δ (VI.E)	laminar boundary layer thickness
Δ (III.B)	ratio of soil moisture to soil porosity
Δ (III.E)	equals zero if condensation occurs onto leaf surfaces. Otherwise it equals one
ε	total atmospheric emissivity
ε_c	emissivity for carbon dioxide
ε_G	ground surface emissivity
ε_f	foliage emissivity
ε_r	emissivity for water vapor
η	soil volumetric moisture
η_{ROOT}	minimum soil moisture in the root zone
η_s	soil porosity
η_{WILT}	permanent wilting soil moisture (15 bar)
θ	atmospheric potential temperature
$\tilde{\theta}$	partially updated potential temperature
θ^+	potential temperature at top of the planetary boundary layer

$\theta\big|_s$	potential temperature on the material surface
θ_*	friction potential temperature
$\theta_*^{\dagger}$	friction potential temperature weighted between bare soil and soil overlain by a canopy
κ	a constant (0.286)
λ	soil thermal conductivity
ν	kinematic viscosity for air
ξ (III.A)	non-dimensional stability height
ξ (III.B)	reference height for computing longwave atmospheric fluxes
π	scaled pressure (Exner function)
ρ	air density
ρ_s	soil density
ρ_w	water density
σ	Stefan-Boltzman constant (1.38×10^{-12} cal/cm^2/sec/°C)
σ_f	foliage shielding factor
τ_m	transmission function for clouds
ϕ	latitude
ϕ_h	non-dimensional similarity function for heat
ϕ_m	non-dimensional similarity function for momentum
ψ	soil moisture potential (suction)
ψ_G	surface moisture potential
ψ_s	saturated moisture potential

SUBSCRIPTS

BARE	bare soil
BASE	cloud base

CTOP	cloud top
G	ground surface
h	canopy height
MAX	maximum
TOP	top of model atmosphere
η	function of soil moisture

Appendix B. Derivation of the Soil Moisture Flux Equation

Horizontal flow within the soil is negligible, especially on the time scale of a typical mesoscale integration. Therefore, only vertical motion, acting under the influence of gravity, will be considered. The Navier-Stokes equation becomes

(1) $\frac{\partial w}{\partial t} + w\frac{\partial w}{\partial z} = - \frac{1}{\rho_w} \frac{\partial p}{\partial z} - g + \frac{\mu}{\rho_w} \nabla^2 w$.

Here w is the vertical velocity of groundwater, P is pressure, μ is the dynamic viscosity, ρ_w is the density of water and z is a vertical coordinate within the soil.

If we further require the flow to be steady, then the left hand side of (1) equals zero. Now we have

(2) $0 = - \frac{1}{\rho_w} \frac{\partial p}{\partial z} - g + \frac{\mu}{\rho_w} \nabla^2 w$.

In any arbitrary unit volume of soil, some of the volume is occupied by void space, which consists of a matrix of interconnected pores. To make (2) meaningful, each component term must be averaged over a unit volume. The second term is straightforward:

$$\int_{\eta_s \Delta v} g \, dv = g \int_{\eta_s \Delta v} dv = g \, \eta_s \Delta v \quad ,$$

where η_s is the porosity, Δv is a unit volume and the product $\eta_s \Delta v$ is the unit void space.

If the motion is assumed to be slow (i.e. no dynamic pressure), then

$$\int_{\eta_s \Delta v} \frac{1}{\rho_w} \frac{\partial p}{\partial z} \, dv = \frac{1}{\rho_w} \overline{\frac{\partial p}{\partial z}} \eta_s \Delta v \quad .$$

And since the averaging volume is not a function of depth, it follows that

$$\overline{\frac{\partial p}{\partial z}} = \frac{\partial \overline{p}}{\partial z}$$

is a reasonable approximation.

The third term on the right hand side of (2) is treated by applying dynamic similarity. Following Hubbert (1956),

$$\int_{\eta_s \Delta v} \nabla^2 w \, dv = \int_{\eta_s \Delta v} \alpha \, \frac{u_d}{d^2} \, dv = \overline{\alpha} \, \frac{u_d}{d^2} \, \eta_s \Delta v \quad ,$$

where α is a proportionality factor, $\overline{\alpha}$ is an average value of α over the unit volume, u_d is the Darcian Velocity and d is a length scale.

Equation (2) is now approximated by

$$0 = -g \, \eta_s \Delta v - \frac{1}{\rho_w} \frac{\partial \overline{p}}{\partial z} \, \eta_s \Delta v + \frac{\mu}{\rho_w} \, \overline{\alpha} \, \frac{u_d}{d^2} \, \eta_s \Delta v \quad ,$$

(3)

or

$$g + \frac{1}{\rho_w} \frac{\partial \overline{p}}{\partial z} = \frac{\mu}{\rho_w} \, \overline{\alpha} \, \frac{u_d}{d^2} \quad .$$

Solving for u_d yields

$$u_d = \left[g \, \frac{\rho_w d^2}{\mu \overline{\alpha}} \right] \frac{\partial}{\partial z} \left(z + \frac{\overline{p}}{g \rho_w} \right)$$

(4)

or

$$u_d = K_\eta \frac{\partial \psi}{\partial z} \quad .$$

The hydraulic conductivity is $K_\eta = \frac{g d^2}{\mu \overline{\alpha}} \rho_w$ and the moisture potential is $\psi = \frac{\overline{p}}{g \rho_w}$. Note that this equation only holds true for small Reynolds numbers. Otherwise the inertial terms are important and dynamic similarity is not realized.

The soil moisture flux of III.D.5 is related to u_d by

$$w_s = \rho_\omega \, u_d \quad .$$

References

Al Nakshabandi, G. and H. Kohnke, 1965: Thermal conductivity and diffusivity of soils as related to moisture tension and other physical properties. Agric. Meteor., 2, 271-279.

American Meteorological Society, 1976: Policy statement of the American Meteorological Society on weather forecasting. Bull. Amer. Meteor. Soc., 57, 1460-1461

Anthes, R. and T. Warner, 1978: Development of hydrodynamic models suitable for air pollution and other meso-meteorological studies. Mon. Wea. Rev., 106, 1045-1078.

Asai, T., 1965: A numerical study of the air-mass transformation over the Japan Sea in winter. J. Meteor. Soc. Japan, 43, 1-15.

Atwater, M., 1973: Atmospheric radiation computations for an urban meteorological pollutant model. Appendix C, 139-158 in Pandolfo and Jacobs (1973).

Atwater, M. and P. Brown, Jr., 1974: Numerical calculation of the latitudinal variation of solar radiation for an atmosphere of varying opacity. J. Appl. Meteor., 13, 289-297.

Black, T. and K. McNaughton, 1971: Psychrometric apparatus for Bowen-ratio determination over forests. Bound. Layer Meteor., 2, 246-254.

Blackadar, A., 1957: Boundary layer wind maxima and their significance for the growth of nocturnal inversions. BAMS, 38:5, 283-290.

Blackadar, A., 1976: Modelling the nocturnal boundary layer. Proceedings of the third symposium on Atmospheric Turbulence, Diffusion and Air Quality. American Meteorological Society, Boston, Mass., 46-49.

Burgy, R. and C. Pomeroy, 1958: Interception losses in grassy vegetation. Trans. Amer. Geophys. Union, 39, 1095-1100.

Burk, S., 1977: The moist boundary layer with a higher order turbulence closure model. J. Atmos. Sci., 34, 629-638.

Businger, J., 1973: Turbulent transfer in the atmospheric surface layer. Workshop in Micrometeorology, Amer. Meteor. Soc., Boston, Mass. Section II, 1-69.

Carpenter, K., 1978: Surface exchanges in a meso-scale model of the atmosphere. Meteo. Off. 11, TN No. 96, 23 pp.

Carpenter, K., 1979: An experimental forecast using a non-hydrostatic mesoscale model. Quart. J. Roy. Meteor. Soc., 105, 629-655.

Changnon, S., Jr., R. G. Semonin and F. A. Huff, 1976: A hypothesis for urban rainfall anomalies. JAM, 15, 544-560.

Clapp, R. and G. Hornberger, 1978: Empirical equations for some soil hydraulic properties. Wat. Resour. Res., 14, 601-604.

Clark, O., 1940: Interception of rainfall by prairie grasses, weeds, and certain crop plants. Ecol. Monogr., 10, 244-277.

Clarke, R., 1970: Recommended methods for the treatment of the boundary layer in numerical models. Austral. Meteor.

Mag., 18, 51-73.

Cotton, W. and R. Pielke, 1980: One day in the life of a Florida seabreeze. In preparation.

Davis, J., 1967: General map of natural vegetation of Florida. Agric. Exper. Stations, Instit. of Food and Agric. Sci., Univ. of Florida, Gainesville.

Deardorff, J., 1974: Three-dimensional numerical study of the height and mean structure of a heated planetary boundary layer. Bound. Layer Meteor., 7, 81-106.

--------------, 1978: Efficient prediction of ground surface temperature and moisture, with inclusion of a layer of vegetation. J. Geophys. Res., 83:C4, 1889-1903.

DeVries, D., 1975: Heat transfer in soils, 5-28 in DeVries, D. and N. Afgan: Heat and Mass Transfer in the Biosphere. Part I. Transfer Processes in the Plant Environment. Scripta Book Co., Wash., D.C. Halstead Press.

Dieterle, D., 1976: Simulation of the urban surface energy balance including the effects of anthropogenic heat production. Rep. No. G320-3344, IBM Palo Alto Scientific Center, Palo Alto, Cal., 61 pp.

Fetcher, N., 1976: Patterns of leaf resistance to lodgepole pine transpiration in Wyoming. Ecology, 57, 339-345.

Fritsch, J. and C. Kreitzberg, 1978: Workshop on local weather forecast techniques--1980 and beyond. Bull. Amer. Meteor. Soc., 59, 293-296.

Gannon, P., Sr., 1978: Influence of earth surface and cloud

properties on the south Florida sea breeze. NOAA Tech. Rep. ERL 402-NHEML2, U.S. Dept. of Commerce, 91 pp.

Gannon, P., Sr., 1979: personal communication.

Garrett, A., 1978: Numerical simulations of atmospheric convection over the southeastern U.S. in undisturbed conditions. Rep. No. 47, Atmos. Sci. Group, Coll. of Engin., Univ. of Texas (Austin), 356 pp.

Gates, D., 1962: Energy Exchange in the Biosphere. Harper and Row, New York and John Weatherhill, Inc., Tokyo, 151 pp.

Geiger, R., 1965: The Climate Near the Ground. Harvard Univ. Press, Cambridge, Mass., 611 pp.

Golden, J., C. Chappell, C. G. Little, A. Murphy, E. Burton and E. Pearl, 1978: What should the NWS be doing to improve short-range weather forecasting? -- A panel discussion with audience participation. Bull. Amer. Meteor. Soc., 59, 1334-1342.

Halstead, M., R. Richman, W. Covey and J. Merryman, 1957: A preliminary report on the design of a computer for micrometeorology. J. Meteor., 14, 308-325.

Helvey, J. and J. Patric, 1965: Canopy and litter interception of rainfall by hardwoods of eastern United States. Wat. Resour. Res., 1, 193-206.

Hicks, B., P. Hyson and C. Moore, 1975: A study of eddy fluxes over a forest. J. Appl. Meteor., 14, 58-66.

Hsu, Hsiao-Ming, 1979: Numerical simulations of mesoscale precipitation systems. Dept. of Atmos. and Oceanic Sci.,

Coll. of Engin., Univ. of Michigan, 342 pp.

Hubbert, M., 1956: Darcy's law and the field equations and
the flow of the underground fluids. Trans. Amer.
Instit. Min. and Metal Engrs., 20, 222-239.

Huff, F. and J. Vogel, 1978: Urban, topographic and diurnal
effects on rainfall in the St. Louis Region. JAM, 17,
565-577.

Idso, S., R. Jackson, B. Kimball and F. Nakayama, 1975a:
The dependence of bare soil albedo on soil water
content. J. Appl. Meteor., 14, 109-113.

--------, T. Schmugge, R. Jackson and R. Reginato, 1975b:
The utility of surface temperature measurements for the
remote sensing of surface soil water status. J. Geophys.
Res., 80:21, 3044-3049.

Jacobs, C., J. Pandolfo and M. Atwater, 1974: A description
of a general three dimensional numerical simulation
model of a coupled air-water and/or air-land boundary
layer. IFYGL Final Rep., CEM Rep. No. 5131-509a.

Jadhav, G., V. Ingle, S. Varade and K. Pawar, 1977: Moisture
retention and available water capacity of Marathwada
soils. J. Indian Soc. Soil Sci., 25, 436-438.

Klemp, J. and D. Lilly, 1978: Numerical simulation of
hydrostatic mountain waves. J. Atmos. Sci., 35, 78-107.

Kondrat'yev, J., 1969: Radiation in the Atmosphere.
Academic Press, New York, 912 pp.

Kuhn, P., 1963: Radiometeorsonde observations of infrared
flux emissivity of water vapor. J. Appl. Meteor., 2,

368-378.

Lavoie,R., W. Cotton and J.B. Hovermale, 1970: Investiga-
tions of lake effect storms. Final Report, Contract
No. E22-103-68(N), Dept. of Meteor., The Penn. State
Univ., 127 pp.

Lettau, H. and B. Davidson, 1957: Exploring the Atmosphere's
First Mile, Vols. I and II, New York, Pergamon Press,
577 pp.

Leuning, R. and P. Attiwill, 1978: Mass, heat and momentum
exchange between a mature Eucalyptus forest and the
atmosphere. Agric. Meteor., 19, 215-241.

Long, P., 1975: Dissipation, dispersion and difference
schemes. NOAA Tech. Mem., NWS TDL, No. 56, 33 pp.

Long, P. and D. Pepper, 1976: A comparison of six numerical
schemes for calculating the advection of atmospheric
pollution. Proc. Third Symposium on Atmospheric Tur-
bulence, Diffusion and Air Quality, Amer. Meteor. Soc.,
Raleigh, N.C.

Mahrer, Y. and R. Pielke, 1977: A numerical study of the
airflow over irregular terrain. Beitrage zur Physik
der Atmosphare, 50, 98-113.

------------------------, 1978a: A test of an upstream spline
interpolation technique for the advective terms in a
numerical mesoscale model. Mon. Wea. Rev., 106, 818-
830.

------------------------, 1978b: The meteorological effect
of the changes in surface albedo and moisture. Israel
Meteor. Research Papers, 2, 55-70.

McNider, R., 1980: personal communication.

McDonald, J., 1960: Direct absorption of solar radiation by atmospheric water vapor. J. Meteor., 17, 319-328.

Molz, F. and I. Remson, 1970: Extraction term models of soil moisture use by transpiring plants. Wat. Resour. Res., 6, 1346-1356.

Monteith, J., (ed.) 1975: Vegetation and the Atmosphere. Volume I Principles. Academic Press, London, 278 pp.

Monteith, J. and G. Szeicz, 1962: Radiative temperature in the heat balance of natural surfaces. Quart. J. Roy. Meteor. Soc., 88, 496-507.

Neumann, J. and Y. Mahrer, 1975: A theoretical study of the lake and land breezes of circular lakes. Mon. Wea. Rev., 103:6, 474-485.

Nimah, M. and R. Hanks, 1973: Model for estimating soil water, plant and atmospheric interrelations: I. Description and Sensitivity. Soil Sci. Soc. Amer. Proc., 37, 522-527.

Nixon, P. and T. Hales, 1975: Observing cold-night temperatures of agricultural landscapes with an airplane-mounted radiation thermometer. J. Appl. Meteor., 14, 498-505.

O'Brien, J., 1970: A note on the vertical structure of the eddy exchange coefficient in the planetary boundary layer. J. Atmos. Sci., 27, 1213-1215.

Odum, W., 1979: personal communication.

Oke, T., 1978: Boundary Layer Climates, Metheun and Co.,

Ltd., Halstead Press, John Wiley and Sons, New York, 327 pp.

Otterman, J., 1974: Baring high-albedo soils by overgrazing: A hypothesized desertification mechanism. Science, 86, 531-533.

Otterman, J., 1975: Possible rainfall reduction through reduced surface temperatures due to overgrazing. Rep. X-910-75-93 (Preprint), NASA, Goddard Space Flight Center, Greenbelt, Md.

Ovington, J., 1954: A comparison of rainfall in different woodlands. Forestry, 41-53.

Paegle, J., W. Zdunkowski and R. Welsh, 1976: Implicit differencing of predictive equations of the boundary layer. Mon. Wea. Rev., 104, 1321-1324.

Pandolfo, J. and C. Jacobs, 1973: Tests of an urban meteorological pollutant model using CO validation data in the Los Angeles metropolitan area, Volume I. The Center for the Environment and Man, Hartford, Conn., 176 pp.

Perkey, D., 1976: A description and preliminary results from a fine-mesh model for forecasting quantitative precip- itation. Mon. Wea. Rev., 104, 1513-1526.

Petersen, G., R. Cunningham and R. Matelski, 1968: Moisture characteristics of Pennsylvania soils: I. Moisture retention as related to texture. Soil Sci. Soc. Amer. Proc., 32, 271-275.

Philip, J., 1957: Evaporation, and moisture and heat fields

in the soil. J. Meteor., 14, 354-366.

Pielke, R., 1974: A three-dimensional model of the sea
breezes over south Florida. Mon. Wea. Rev., 102, 115-
139.

----------, 1979: personal communication.

---------- and Y. Mahrer, 1978: Verification analysis of
the University of Virginia three-dimensional mesoscale
model prediction over south Florida for 1 July 1973.
Mon. Wea. Rev., 106, 1568-1589.

Rijtema, P., 1970: Soil moisture forecasting. Instit. for
Land and Water Management Res., Note 513, Wageningen,
The Netherlands, 28 pp.

Rosenthal, S., 1978: Numerical simulation of tropical cyclone
development with latent heat release by the resolvable
scales. I: Model description and preliminary results.
J. Atmos. Sci., 35, 258-271.

Salter, P. and J. Williams, 1965: The influence of texture
on the moisture characteristics of soils. II. Avail-
able-water capacity and moisture release characteristics.
J. Soil Sci., 16, 310-317.

Sasamori, T., 1970: A numerical study of atmospheric and
soil boundary layers. J. Atmos. Sci., 27, 1122-1137.

-----------, 1972: A linear harmonic analysis of atmos-
pheric motion with radiative dissipation. J. Meteor.
Soc. Japan, 50, 505-517.

Sellers, W., 1965: Physical Climatology. Univ. of Chicago
Press, 272 pp.

Sim, L., 1972: Interception loss in the humid forested
    areas (with special reference to Sungai Lui Catchment,
    West Malaysia). Malay. Nat. J., 25, 104-111.

Simpson, J., N. Westcott, R. Clerman and R. Pielke, 1979:
    On cumulus mergers. Arch. Met. Geoph. Biokl. Ser. A.,
    1-29.

Tapp, M. and P. White, 1976: A non-hydrostatic mesoscale
    model. Quart. J. Roy. Meteor. Soc., 102, 277-296.

Thom, A., 1971: Momentum absorption by vegetation. Quart.
    J. Roy. Meteor. Soc., 97, 414-428.

--------, J. Stewart, H. Oliver and J. Gash, 1975: Compar-
    ison of aerodynamic and energy budget estimates of
    fluxes over a pine forest. Quart. J. Roy. Meteor. Soc.,
    101, 93-105.

van Bavel, C. and D. Hillel, 1976: Calculating potential
    and actual evaporation from a bare soil surface by
    simulation of concurrent flow of water and heat. Agric.
    Meteor., 17, 453-476.

Whisler, F., A. Klute and R. Millington, 1968: Analysis of
    steady-state evapotranspiration from a soil column.
    Soil Sci. Soc. Amer. Proc., 32, 167-174.